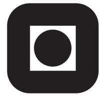

NTNU – Trondheim
Norwegian University of
Science and Technology

A first-principles Study of epitaxial Interfaces between Graphene and GaAs

Astrid Marthinsen

Nanotechnology
Submission date: June 2014
Supervisor: Sverre Magnus Selbach, IMTE
Co-supervisor: Zhaohui Wang, IMT
Gerhard Olsen, IMT

Norwegian University of Science and Technology
Department of Materials Science and Engineering

Abstract

Epitaxial interfaces between graphene and GaAs(111) have been investigated through a first-principles study using density functional theory (DFT). The GaAs(111) surface at the interface is assumed to be 2×2 reconstructed with Ga vacancies. Three different relative phase orientations between the GaAs(111) surface and graphene have been studied; 0°, 16.1° and 30°, respectively, where three translations of the 0° configuration have been considered. Within the three considered epitaxial phase orientations, the GaAs phase is strained in the (111) plane to accommodate a lattice mismatch of 6.3%, 10% and -8.2% in the 0°, 16.1° and 30° orientations, respectively. Biaxial straining of bulk GaAs has been studied, both in the zincblende (ZB) phase ((111) plane) and in the meta-stable wurtzite (WZ) phase ((0001) plane). The relative stabilities of the two phases are found to depend on the degree of strain. Biaxial straining of GaAs(111) surfaces have also been investigated. The surface reconstruction energy is highly dependent on the degree of strain for GaAs(111)-2×2 reconstructed surfaces.

The interactions between GaAs and graphene at the interface have been studied by two different exchange-correlation functionals: The semi-local GGA functional PBEsol, and the van der Waals (vdW) functional optPBE. The latter is found to yield a significantly stronger interaction energy, which signifies a substantial vdW contribution to the interactions at the GaAs/graphene interface. The interaction energy between GaAs and graphene is estimated for the five configurations considered. The estimates vary in the range 0.24-0.31 J/m^2. The strongest interaction energy is found for the 30° configuration.

Sammendrag

Epitaksielle grenseflater mellom grafen og GaAs(111) er undersøkt gjennom en *ab initio* studie ved bruk av tetthetsfunksjonalteori. En 2×2 overflatereonstruksjon med Ga-vakanser er antatt å finne sted på grenseflata. Tre ulike relative faseorienteringer mellom GaAs(111)-overflata og grafen er studert, henholdsvis 0°, 16.1° og 30°, hvor tre translasjoner av 0°-konfigurasjonen har blitt betraktet. I de tre betraktede epitaksielle orienteringene er GaAs-fasen tøyd for å etterkomme en gittermistilpasning på 6.3%, 10% og -8.2% i henholdsvis 0°, 16.1° og 30°-orienteringen. Biaksiell tøyning av bulk GaAs er studert, både i sinkblende-fasen (i (111) planet) og i den metastabile wurtzitt-fasen (i (0001) planet). De relative stabilitetene til de to fasene er avhengig av graden av tøyning. Biaksiell tøyning av GaAs(111)-terminert overflate har også blitt undersøkt. Overflaterekonstruksjonsenergien er høyst avhengig av graden av tøyning i GaAs(111)-2 × 2 rekonstruerte overflater.

Interaksjonene mellom GaAs og grafen i grenseflata har blitt studert med to ulike exchange-korrelasjonsfunksjonaler: Det semi-lokale GGA funksjonalet PBEsol og van der Waals funksjonalet optPBE. Sistnevnte viser en signifikant mye sterkere interaksjonsenergi, som indikerer et betydelig vdW bidrag til interaksjonene ved grenseflata mellom GaAs/-grafen. Interaksjonsenergien mellom GaAs og grafen er estimert for de fem ulike konfigurasjonene. Estimatene spenner energiintervallet 0.24-0.31 J/m^2. Den sterkeste interaksjonsenergien er funnet for 30° konfigurasjonen.

Contents

Preface ix

1 Introduction 1
1.1 The present work . . . 3

2 Density functional theory 5
2.1 The Schrödinger equation . . . 5
2.2 The basis of DFT . . . 6
2.3 The Kohn-Sham equations . . . 7
2.4 The exchange-correlation functional . . . 8
2.5 Calculation scheme . . . 8
2.6 Hellmann-Feynman forces . . . 9
2.7 Computational approaches to DFT . . . 9
2.8 Non-Localized Exchange Correlation Functionals . . . 12
2.9 VASP . . . 12

3 Materials and Background 15
3.1 Graphene . . . 15
3.2 GaAs . . . 17
3.3 van der Waals interactions . . . 20
3.4 Previous DFT studies . . . 21

4 Computational details 23
4.1 Bulk GaAs and graphite . . . 23
4.2 GaAs surface reconstruction . . . 26
4.3 Heterostructure calculations . . . 32

5 Results 37
5.1 Bulk GaAs and graphite . . . 37
5.2 GaAs surface reconstruction . . . 43
5.3 GaAs graphene heterostructures . . . 53

6 Discussion 63
6.1 Epitaxial configurations . . . 63
6.2 Energy landscape at the interface . . . 65
6.3 Structural and electronic considerations . . . 71

6.4 The Computational Model 75
6.5 Further work 76

7 Conclusion 77

Bibliography 79

A VASP 85
A.1 The Four Main Input Files 85
A.2 Accurate DOS calculations 89

B VASP files 91
B.1 Bulk GaAs 91
B.2 Graphite $P6_3mc$ 92
B.3 GaAs surface reconstruction 94
B.4 Heterostructure calculations 95

List of Figures

1.1 Ref. [1]. Schematics of GaAs nanowire growth on graphene and epitaxial growth model. 2

3.1 Honeycomb structure of graphene. Ref. [2] Bandstructure of graphene. 15
3.2 Ref. [3] Different graphitic materials. 16
3.3 Zincblende crystal structure 17
3.4 Schematics illustrating a direct and an indirect bandgap . . . 18
3.5 Ref. [4] Top schematic view of the 2×2 vacancy buckling model. 20
3.6 Ref. [1] Epitaxial model presented by Munshi et al. 21

4.1 Total energy per atom as function of cutoff energy. 24
4.2 Visualization of the WZ structure and the ZB structure. . . . 24
4.3 Total energy of GaAs per atom as function of k-point density. 25
4.4 Total energy per atom for graphite $P6_3mc$ as function of cutoff energy. 26
4.5 Visualization of the constructed supercell with a GaAs symmetric double-slab. 27
4.6 Total energy per atom for different restrictions of the atomic convergence criterion for GaAs double-slab supercells. 29
4.7 Total energy per unit supercell (u.sc.) as function of distance between the periodically repeated GaAs slabs. 29
4.8 Crystallographic structure of orthorombic Ga metal. 30
4.9 Chemical potential for Ga(s) 31
4.10 Visualization of heterostructure slab and five epitaxial configurations. 33
4.11 Different sites on graphene, top, hollow and bridge sites respectively. 34

5.1 Elastic modulus and bulk modulus for graphene and GaAs. . 38
5.2 Straining in *ab*-plane of GaAs ZB(111) and GaAs WZ(0001) . 39
5.3 Relaxed *c* parameter as function of *ab*-plane strain for bulk GaAs, ZB and WZ. 40
5.4 Supercell structures for bulk WZ GaAs and ZB GaAs(111). . 40
5.5 Density of states for bulk GaAs, wurtzite and zincblende structure 41

5.6 Orbital resolved density of states for grapite P6_3mc. 42
5.7 Bandgap as function of percentage strain of GaAs zincblende structure in the (111) plane. 42
5.8 Visualization of relaxed GaAs reconstructed slab. 44
5.9 LDOS regions for GaAs slab supercell. 45
5.10 LDOS for GaAs slab supercell 46
5.11 Orbital resolved LDOS for GaAs slab supercell 47
5.12 Total energy as function of ab-straining for reconstructed and bulk-terminated supercells. 50
5.13 Visualization of strained bulk-terminated structures. 51
5.14 LDOS for three different strain values of the reconstructed GaAs slab. 52
5.15 Comparison of energy as function of distance between graphene and GaAs for calculations performed with PBEsol and optPBE, with different carbon potentials. 55
5.16 Total energy as function of distance between GaAs and graphene. 56
5.17 Ionic relaxation at the interface of 30° Bridge and 0° Top configuration. 57
5.18 LDOS regions for heterostructure slab. 59
5.19 LDOS for the dynamically relaxed heterostructure for the 30° orientation. 60
5.20 Orbital resolved LDOS for GaAs regions of dynamically relaxed heterostructure for the 30° orientation. 61
5.21 Orbital resolved LDOS for graphene regions of dynamically relaxed heterostructure for the 30° orientation. 62

6.1 Energy penalty of ab-plane straining per 2×2 reconstructed surface. 65
6.2 The reconstruction energy per 2×2 surface unit cell as function of strain in the ab-plane. 66
6.3 Estimation of interaction energy between GaAs and graphene for five different configurations. 69
6.4 Interlayer binding energy for graphite $P6_3mc$. 70
6.5 Electron localization function for three different graphene sheets in the 30 ° heterostructrue supercell. 72
6.6 Electron localization function at the interface between graphene and GaAs in the dynamically relaxed 30° supercell. 73
6.7 Electron localization function visualized for different regions of the dynamically relaxed 30° Bridge cell for different isosurface levels. 74

List of Tables

5.1 Calculated bandgaps for bulk GaAs zincblende (ZB) and wurtzite (WZ) at zero strain. 42
5.2 Relative GaAs/graphene phase orientations and their associated strain level. 49

6.1 Estimated interaction energies for different epitaxial configurations 67

Preface

This Master thesis is carried out at the Norwegian University of Science and Technology, at Department of Materals Science and Engineering, as a part of my master degree in Nanotechnology. The present project is a continuation of my project work, *DFT calculation of semiconductor/graphene interfaces* [5], that was carried out during the fall 2013. The idea behind the project is attributed my supervisor, Assoc. professor Sverre M. Selbach. Because this is a continued project, parts of the theory from the project report [5] have been reused in the current theory chapters.

Acknowledgements

I would like to give a special, warm thanks to my supervisor Assoc. professor Sverre M. Selbach for giving me invaluable guidance throughout this present work. This has been a challenging project, without always knowing what the next logical step in the research would be. Sverre's dedication, and the many hours he has devoted to the project has been of great importance for my motivation and what I have been able to achieve throughout this work.

I would also give a thanks my two co-supervisors MSC Gerhard Olsen and PhD Zhaohui Wang for all the help and support throughout the project work. VASP and Unix would be far less comprehensible without their help and good advices.

Astrid Marthinsen
Trondheim, June, 2014

Chapter 1

Introduction

Semiconductor devises have in our modern society penetrated into a large part of our lives as they are essential components in all modern elecronics. Ever since the transistor was first developed by Bardeen, Brattain and Shockley in 1947 [6], the semiconductor manufacturing industry has been continuously developing. The desire to constantly improve performance and create smaller, cheaper and faster electronics is a strong driving force for the field of semiconductor research, which thus today is a reseach field which has attained massive interest.

Semiconductor devices are traditionally silicon based. However, as silicon seem to be reaching its limits of downscaling and improved performance [7], other materials are being investigated for their potential in semiconductor manufacturing. Much attention has been given to the III-V semiconductor compounds for their potential in development of nano-scale electronics, such as nanometer-scaled transistors [7, 8]. III-V semiconductors are materials that combine elements from group III and V in the periodic table, such as GaAs, AlAs, InAs and InP. Some of the III-V semiconductors also have unique optical and optoelectronic properties, making them desirable materials in optoelectronic devices such as lasers and light emitting diodes (LEDs) [9]. Also, many of these material, exhibit extremely good electron transport properties and frequency response [7].

Semiconductor nanowires have attained much interest with respect to the development of future nanoscale electronics as they are highly versatile building blocks. Parameters such as dimension, composition, architecture and doping can be controlled, which implies enabling tailoring of their properties [10]. During the past decade semiconductor nanowires have been explored for the potential to develop a new generation solar cells [11]. This research is fueled by the ever desire to obtain solar cells with higher efficiency to a lower production cost. The advantages of nanowires are firstly that during heteroepitaxal growth, the nanowires are able to accommodate a larger lattice mismatch with respect to the substrate compared to growth of thin films, opening for a vast number of material possibilities for semiconductor heterostructure manufacturing [12]. This also renders a flexibility in substrate choice, which

could reduce cost. Choosing a substrate material being e.g. transparent and/or flexible could expand the integrating possibilities of solar cells in buildings, and also implement solar cells into fabrics [11]. III-V nanowires are attractive materials in optoelectronics, due to their unique absorption and emission abilities [13]. This is due to the combined fact that nanowires exhibit highly anisotropic properties because of their large aspect ratio and the specific crystallographic structure that the III-V semiconductors may exhibit at nanoscale, which can be very different from the bulk [13].

Graphene has in the recent few years been investigated for its potential as a substrate for growth of nanowires, owing to the many extraordinary properties of this unique material [1]. Having both superb mechanical properties, being transparent, conductive and flexible [3], graphene is commonly referred to as a "super material" in material science. Although graphene has been known to be the basic building block for graphite for several decades, it was believed until only ten years ago that graphene could not exist on its own as solely a 2D material. However, in 2004 Novoselov and Geim were able to isolate a single sheet of graphene, by the simple means of tearing the graphene layers in graphite apart with Scotch tape [14]. This fairly primitive means of isolating one atomic thick graphene, is due to the weak van der Waals forces that act between the graphene layers in graphite, which makes it easy to tear them apart.

The excellent properties of graphene, and the fact that it is a 2D material, renders it a highly attractive substrate material for nanowire growth, opening the possibility of e.g. designing highly flexible electronic components.

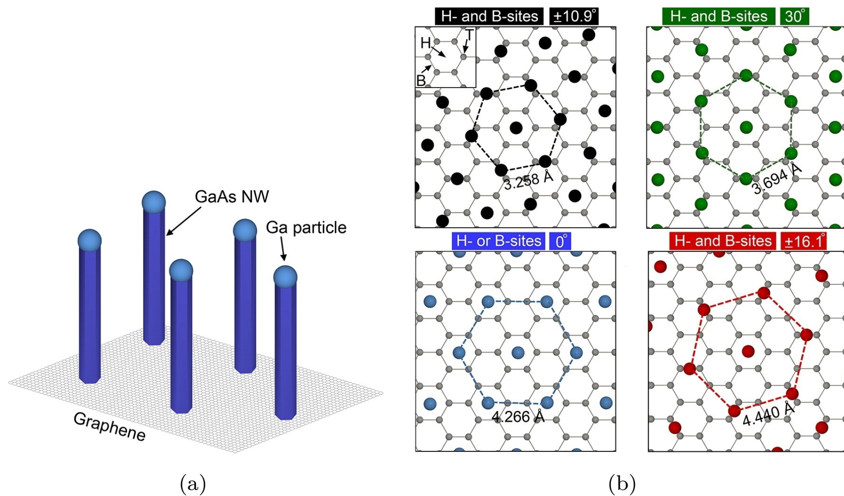

Figure 1.1: *Ref. [1] Munshi et al. have reported growth of GaAs nanowires on graphene using Molecular Beam Epitaxy (MBE). (**a**) Shematics of the growth of GaAs nanowires on graphene. (**b**) Model of potential epitaxial growth configurations between GaAs and graphene.*

A research group at Department of Electronics and Telecommunications

at Norwegian University of Science and Technology (NTNU) published in 2012 an article reporting growth of GaAs nanowires on graphene by molecular beam epitaxy (MBE) (Figure 1.1(a)) [1]. In the same paper, a model for epitaxial growth of GaAs on graphene is suggested. Graphene exhibits in-plane hexagonal symmetry. As GaAs in the zinkblende crystallographic structure also exhibits in-plane hexagonal symmetry in the [111] growth direction, this is indeed the preferred growth direction of GaAs on graphene [1]. The presented model of the different epitaxial growth configurations is however solely a geometric consideration of different possibilities (Figure 1.1(b)). The epitaxial structure at the interface between the GaAs nanowires and graphene is thus not yet fully explored and understood. As the properties at the interface of the heterostructure may differ from those of the individual phases, the presence of the interface may alter the properties of the overall structure. This will again affect the performance of the heterostructure component as a whole. Therefore, it is important to investigate and understand the properties at, and the impact of the present interface in the heterostructure.

1.1 The present work

In this Master Thesis the atomic and electronic structure at the interface between GaAs and graphene is studied with a first principles approach, using density functional theory (DFT). As of today, reported DFT studies performed on such heterostructure interfaces are limited. Only a few other research groups have conducted first principles studies on semiconductor/graphene interfaces [15, 16]. The epitaxial structure and the strength and nature of the interactions at such interfaces are still far from fully understood. The present work is thus partly an effort to develop methodology for how to construct a computational model that can provide physical information about the structure and electronic properties at the interface. The present work is also a contribution to gaining a better understanding of the nature of the epitaxy and the energetic landscape at the interface. GaAs is chosen as a model material as it is a promising material in future nanoscale electronics. However, the findings in the present work can also apply to similar heterostructure systems.

At the interface, weak van der Waals (vdW) forces act between the present phases. These are non-localized dispersion forces that are not captured by conventional local and semi-local exchange-correlation functionals used in DFT. To capture these weak dispersion forces, specially developed vdW functionals need to be used. However, the disadvantage with vdW functionals is that they make calculations much more computationally demanding. Therefore, both conventional functionals as well as vdW functionals have been tested to gain knowledge about what the different functionals are able to capture, and what the local and semi-local functionals fail to describe as compared to vdW functionals.

To be able to understand the materials under discussion and their properties at the interface, it is important also to understand their bulk properties

and bulk behaviour. Therefore, the respective bulk materials have been investigated computationally.

Because of the strong energetic driving force associated with reconstruction of the GaAs (111) free surface, it is reasonable to assume that a reconstruction of GaAs at the interface between graphene and GaAs also could take place. Yelgel et al. [15] and Hong et al. [16] have conducted first-principles studies on the InAs/graphene interface, both finding that a surface reconstruction of InAs at the interface is more energetically favourable than having a non-reconstructed InAs surface. Different reconstructions of the GaAs (111) surface have been reported in literature. Both a 2×2 reconstruction and a $\sqrt{19} \times \sqrt{19}$ reconstruction have been observed with scanning tunneling microscopy (STM) [17]. In the present work, a 2×2 reconstruction of GaAs at the interface has been assumed. A 2×2 reconstruction is the most simple assumption, and a natural starting point. Further, different epitaxial configurations between graphene and GaAs have been considered, based on the epitaxial configurations within the model presented by Munshi et al. [1].

Chapter 2

Density functional theory

The scope of this chapter is to give a brief introduction to the fundamentals of density functional theory (DFT). It is not intended to give a complete quantum mechanical explanation of the theory, but merely give a comprehensive overview for the reader with no previous knowledge of DFT. For further literature about DFT, it is referred to the references [18] and [19], which are the two main references of this introduction to DFT. At the end of this chapter, a brief introduction to the simulation package, *Vienna Ab initio Simulation Package* (VASP) [20–23] is included, used to perform the calculations in this present work.

2.1 The Schrödinger equation

The distribution of electron states in a material is predicted by the solution of the Schrödinger equation. Consider a crystal in which the atoms are arranged in a periodic manner. In the most general terms a system of interacting nuclei and electrons can be described by the time-dependent Schrödinger equation [19]:

$$i\hbar\frac{\partial}{\partial t}\psi(\{\mathbf{r}_j\},\{\mathbf{R}_J\},t) = H\psi(\{\mathbf{r}_j\},\{\mathbf{R}_J\},t) \tag{2.1}$$

where ψ is the system wave function, $\{\mathbf{r}_j\}$ the electron positions, $\{\mathbf{R}_J\}$ the nuclei positions, t is time and H the Hamiltonian of the system. Because of the considerably larger mass of the positive nuclei compared to the electrons, they have a much larger inertia, thus respond much more slowly to Coloumb interactions. Therefore, the nuclei are considered to be fixed, and their Coloumb potential is considered an external electrostatic field in which the electrons are free to move around. This assumption is called the Born-Oppenheimer approximation [24]. This reduces the problem to solving the time-independent Schrödinger equation:

$$\left[\frac{\hbar}{2m} \sum_{i=1}^{N} \nabla_i^2 + \sum_{i=1}^{N} V(\mathbf{r}_i) + \sum_{i=1}^{N} \sum_{i<j} U(\mathbf{r}_i, \mathbf{r}_j) \right] \psi = E\psi \tag{2.2}$$

In equation 2.2 three terms are included in the Hamiltonian; from left these are the electron kinetic energy operator, the potential energy operator considering the electrostatic potential from the nuclei, and the potential energy operator in which repulsive electron-electron forces are considered. The sums run over all N electrons in the system. A bulk material consists of an excessive number of electrons, thus the number N soon becomes very large and solving the Schrödinger equation becomes a many body problem. Computationally, this is an exhausting matter; but here is where density functional theory comes into play.

2.2 The basis of DFT

Density functional theory solves the many-body problem by reformulating the system wave function, which is a function of N variables, in terms of the electron density $n(\mathbf{r})$, a function of three spatial coordinates:

$$n(\mathbf{r}) = 2 \sum_{i=1} \psi_i^*(\mathbf{r}) \psi_i(\mathbf{r}) \tag{2.3}$$

where the electron density is the sum over all the individual electron wave functions i and the factor 2 accounts for the two possible electron spin states. The basis for density functional theory is derived from a fundamental theorem stated by P. Hohenberg and W. Kohn. The theorem states [25]:

Theorem 1. *For a system of interacting electrons in an external potential, the ground state energy is a unique functional*[1] *of the electron density:*

$$E[n(\boldsymbol{r})] = \int V(\boldsymbol{r}) n(\boldsymbol{r}) d^3 r + F[n(\boldsymbol{r})] \tag{2.4}$$

Further, the ground state energy E_0 can be found by minimizing the energy functional with respect to the electron density, n_0 being the ground state density:

$$E_0 = E[n_0(\boldsymbol{r})] \tag{2.5}$$

E[n($\mathbf{r}$)] is the energy functional, n($\mathbf{r}$) is the electron density, V($\mathbf{r}$) is the external potential, and F[n($\mathbf{r}$)] is called the exchange functional. The exact formulation of this functional is however not known. The exchange functional will be addressed in more detail later in this chapter.

The second part of the Hohenberg Kohn theorem provides a method to determine the ground state energy functional and finding the relevant electron density by simply varying the electron density until the minimum of the energy functional is reached. This is the *variational principle*.

[1] A functional is a function of a function

2.3 The Kohn-Sham equations

The problem of handling an unknown functional, the exchange functional, was resolved by Kohn and Sham [26]. They separated the exchange functional into three parts,

$$F[n(\mathbf{r})] = T[n(\mathbf{r})] + E_H[n(\mathbf{r})] + E_{xc}[n(\mathbf{r})] \tag{2.6}$$

where $T[n(\mathbf{r})]$ is the kinetic energy of a *non-interacting* electron gas, $E_H[n(\mathbf{r})]$ is the Hartree energy and $E_{xc}[n(\mathbf{r})]$ the exchange-correlation energy. The Hartree energy is the total Coloumb interaction of the electrons with all the other electrons in the system, and can be expressed by the electron density by the following equation:

$$E_H[n(\mathbf{r})] = \frac{e^2}{2} \int \int \frac{n(\mathbf{r})n(\mathbf{r}')}{|\mathbf{r} - \mathbf{r}'|} d^3r d^3r' \tag{2.7}$$

The last term, the exchange-correlation energy, includes all the quantum-mechanical effects that are not taken into account in the two former terms. An example of this is the non-physical aspect of the Hartree energy, in which the interaction of an electron with the electron density also includes a non-physical self-interaction, as this electron is also included in the electron density. This term needs to be approximated, and there are several approaches to resolving this difficulty, which will be elaborated later in this chapter.

In the Kohn-Sham approach, the electron wavefunctions are treated as being non-interacting, which simplifies the problem of finding the system wavefunction extensively. Thus, the system wavefunction can be found by solving a system of single-electron equations given by:

$$\left[-\frac{\hbar^2}{2m}\nabla^2 + V(\mathbf{r}) + V_H(\mathbf{r}) + V_{xc}(\mathbf{r}) \right] = \epsilon_i \psi_i(\mathbf{r}) \tag{2.8}$$

where the single electron Hamiltonian includes from the left, the kinetic energy operator, the external potential from the positive nuclei, followed by two potentials stemming from the two last terms in the separated exchange functional $F[n(\mathbf{r})]$, given by equation 2.6, the Hartree potential,

$$V_H = e^2 \int \frac{n(\mathbf{r}')}{|\mathbf{r} - \mathbf{r}'|} d^3r' \tag{2.9}$$

and the exchange-correlation potential,

$$V_{xc}(\mathbf{r}) = \frac{\delta E_{xc}(\mathbf{r})}{\delta n(\mathbf{r})} \tag{2.10}$$

.
The set of equations on the same form as equation 2.8 constitute the Kohn-Sham equations [26].

2.4 The exchange-correlation functional

It is previously mentioned that the exchange-correlation functional is not precisely known and therefore needs to be approximated. The most simple approach is the Local Density Approximation (LDA) [27]. The basis of this approximation is that the exchange-correlation functional indeed is precisely known for one specific case, where the electron density is independent of position $\mathbf{r}$, namely the uniform electron gas. Thus, in the local density approximation it is assumed that for every position $\mathbf{r}$ the exchange-correlation functional is equal to the known functional of constant electron density, given that this density equals $n(\mathbf{r})$,

$$V_{xc} = V_{xc}^{electron\ gas}[n(\mathbf{r})]. \tag{2.11}$$

Although this may appear to be a very rough approximation, LDA has shown to give very good results in predicting physical properties for a range of systems.

From this starting point, there exists many approximations that seek to increase the accuracy compared to the LDA. The best known scheme for approximating the exchange functional apart from LDA is the Generalized Gradient Approximation (GGA). As the name suggests, also the gradient of the density is taken into consideration in this approximation, as well as the density itself:

$$E_{xc}^{GGA}[n(\mathbf{r})] = \int f((n(\mathbf{r})), \nabla n(\mathbf{r}))d^3r \tag{2.12}$$

However, as opposed to LDA, the GGA scheme is not unique. Thus, there is a vast number of possibilities as to which form of the function $f((n(\mathbf{r})), \nabla n(\mathbf{r}))$ could take. Two schemes that have shown to be very successful are the PW91 scheme by Perdew and Wang [28, 29] and the PBE scheme by Perdew, Burke and Ernzerhof [30, 31], and named thereafter.

2.5 Calculation scheme

The Hohenberg-Kohn theorem gives rise to a method of finding the ground state electron density, by varying the energy functional until the minimum of the functional is reached. Further, the Kohn-Sham equations provide the necessary mapping of the correlated electron-wavefunctions into a set of handleable non-interacting wavefunctions. This provides a strategy for solving the initial problem of achieving the system wavefunction from the many-body Schrödinger equation, eq. 2.1. The procedure is given in the following scheme.

1. An initial trial density is suggested.
2. From this trial density the Hartree potential can be calculated.
3. Based on the Hartree potential the single-electron wavefunctions can be found from the Kohn Sham equations.

4. The new electron density from equation 2.3 based on the wavefunctions found from the Kohn-Sham equations is calculated.

5. The found electron density is used as a new trial density. The procedure is then repeated from step 1 and run iteratively until the density that minimizes the energy functional is found.

2.6 Hellmann-Feynman forces

When the electronic convergence loop given by the calculation scheme in section 2.5 has reached a minimum energy level for a given ionic configuration, forces exerted on the ions can be calculated. The calculated forces can then be used to move the ions, achieving a new ionic configuration, for which a new electronic loop can be run.

These analytic forces can be obtained from the Hellmann-Feynman theorem [32, 33]. This theorem states that if the electron wavefunctions have reached the Kohn-Sham eigenstates, the force contribution from the electrons exerted on an ion J is the partial derivative of the Kohn Sham energy with respect to its position $\mathbf{R}_J$, thus

$$\mathbf{F}_J^{elec} = -\frac{\partial E}{\partial \mathbf{R}_J} \tag{2.13}$$

We refer to the forces acting on the ions as Hellmann-Feynman forces, which are to be calculated for each ionic position update.

2.7 Computational approaches to DFT

Solving eq. 2.2, even with the tool of DFT, is computationally exhausting. Therefore, there are several approaches to reduce the computational load.

2.7.1 Energy cutoff

In a periodic potential, as in a crystalline material, the eigenfunctions of the wave equation may be expressed as a product of a plane wave and a periodic function $u_k(\mathbf{r})$, with periodicity equal to the potential. This is the Bloch theorem, and such functions are called Bloch functions [34]:

$$\psi_k(\mathbf{r}) = e^{i\mathbf{k}\cdot\mathbf{r}} u_k(\mathbf{r}) \tag{2.14}$$

Because $u_k(\mathbf{r})$ has the crystal periodicity, it can be expressed in terms of a Taylor series,

$$u_{\mathbf{k}}(\mathbf{r}) = \sum_{\mathbf{G}} c_{\mathbf{G}} e^{i\mathbf{G}\cdot\mathbf{r}} \tag{2.15}$$

which is a sum of plane waves with wavevector $\mathbf{G}$, where $\mathbf{G}$ is a reciprocal lattice vector, thus $G = m_1\mathbf{b}_1 + m_2\mathbf{b}_2 + m_3\mathbf{b}_3$. Recall that the reciprocal lattice vectors are defined in a way such that $\mathbf{b}_1 \cdot \mathbf{a}_j = 2\pi\delta_{ij}$, δ_{ij} being the

Kronecker delta, such that $\mathbf{G} \cdot \mathbf{a}_i = 2\pi m_i$. Combining equations 2.14 and 2.15 gives

$$\psi_{\mathbf{k}}(\mathbf{r}) = \sum_{\mathbf{G}} c_{\mathbf{k}+\mathbf{G}} e^{i(\mathbf{k}+\mathbf{G})\mathbf{r}} \tag{2.16}$$

i.e a sum of plane waves, with a modified wavevector including **k**. The consequence of equation 2.16 is that determining the wavefunction for each **k** vector involves a summation over infinitely many **G** vectors, which in a numerical perspective is not feasible. Consider the energy of a plane wave with wavevector **k**'=**G**+**k**:

$$E = \frac{\hbar^2}{2m}|\mathbf{k}+\mathbf{G}|^2 \tag{2.17}$$

Because systems tend to seek towards an energy minimum, the higher energy levels are considered less significant than the lower ones, and with respect to calculating the plane wave for a given **k** vector, only the **G** vectors up to a certain $\mathbf{G}_{max}$ are considered, such that

$$\psi_{\mathbf{k}}(\mathbf{r}) = \sum_{|\mathbf{G}+\mathbf{k}|<G_{cut}} c_{\mathbf{k}+\mathbf{G}} e^{i(\mathbf{k}+\mathbf{G})\mathbf{r}} \tag{2.18}$$

where we have defined an energy cutoff

$$E_{cut} = \frac{\hbar}{2m} G_{cut}^2 \tag{2.19}$$

2.7.2 k-space

A neat consequence of the Bloch theorem is that all unique **k** vectors are found within the first Brillouin zone (BZ). This comes from the fact that every chosen **k** vector outside of the first BZ can be translated back into this zone by an appropriate choice of reciprocal vector **G**. Thus, any **k** vector exceeding the first BZ does not provide any more physical information, and therefore, solving the wave equation reduces to solving for wavevectors confined within the first BZ. However, numerically, one cannot do a continous integration over all possible wavevectors, and thus k-space has to be discretized. This is done by projecting a mesh onto the first BZ and find the solutions for the wavefunctions at the mesh points.

2.7.3 Pseudopotentials

The number of electrons in a crystal quickly reach very large values as the size of the crystal grows. Take silicon with atomic number 14 in the periodic table as an example. There will be 14 electrons associated with each atom. For a single unit cell consisting of 8 atoms, the number of electrons is 112. Mininizing the energy functional with all electrons being free to move around clearly becomes a computationally costly process. Therefore, pseudopotentials are introduced, in which electrons in the inner shells are frozen and thus considered a part of an effective external potential, constituted of the nucleus and the

frozen electrons. One can argue that this is a reasonable approximation as the inner electrons are more bound than the outer ones. Pseudopotentals are commonly referred to as soft or hard, and this reflects upon the cutoff-energy for the plane wave basis. The softer the potential, the lower cutoff energy is needed.

2.7.4 Convergence

Convergence is an essential aspect of DFT calculations. Because these are numerical calculations there will be round-off errors along the calculation pathway. The level of accuracy of the calculations will depend on how well the calculations are converged. In order to have a well converged system, a sufficiently fine k-mesh needs to be projected onto the BZ. Thus, before performing calculations on a system, convergence tests should be performed, to assure that a sufficient number of k-points are used. k-point density convergence tests are performed by calculating the system energy as a function of number of k-points. The higher the k-point density, the more accurate the results. However, along with higher accuracy comes a higher computational work load. There will always be a trade-off between the the computational work and the accuracy of the calculations. The level of convergence of a system can thus be indicated by the size of the energy fluctuations for the chosen k-point density. Moreover, one needs to assure that the plane-wave basis set is large enough, by setting a sufficiently high cutoff-energy. Cutoff-energy convergence tests are performed analogously to k-point tests by calculating the system energy as a function of cutoff-energy.

2.7.5 Limitations of DFT

When performing calculations within DFT, it is important to understand the limitations of the theory. Firstly, we need to understand the concept of convergence. DFT calculations do not provide us with the exact solution of the Schrödinger equation because the exact energy functional described in the Kohn-Hohenberg theorems is simply not known. Thus, convergence in relation to DFT does not mean convergence towards the true solution. Therefore, when performing DFT calculations, this will always be an intrinsic uncertainty, and magnitude of this uncertainty between the calculated solution and the real solution is not completely known. Except from this there are some well known examples in which DFT clearly show its limitations. The most important ones are briefly elaborated below.

Underestimating Band-gaps DFT calculations generally underestimates band gaps. This has to do with the fact that DFT does not deal well with exited electronic states, because the Hohenberg-Kohn theorem which is the fundament of DFT in principle only applies to ground-state energies.

Overbinding A limitation that in particular is related to the LDA functional is the tendency of overbinding. This is reflected in an underestimation

of lattice parameters while cohesive energies and elastic moduli are typically overestimated.

Neglecting van der Waals interactions An important limitation to DFT, using the standard functionals LDA and GGA, is that long range non-covalent interactions cannot be treated. The binding energy curves decay exponentially with density overlap, thus, does not capture the vdW interactions that decays as $-\frac{A}{R^6}$. (see Section 3.3).

2.8 Non-Localized Exchange Correlation Functionals

In Section 2.4 the simplest and most conventional exchange functionals are presented. However, these functionals are localized (LDA) or semi-localized (GGA), that therefore make them unable to predict properly certain physical properties. The most important properties that DFT with the traditional functionals fail to predict are described in Section 2.7.5. There is however a constant effort to develop functionals that are able to overcome these well-known limitations. In fact, developing methods that include dispersion has been a very important field within DFT the last decade [35].

2.8.1 van der Waals functionals

van der Waals (vdW) functionals are non-localized exhange functionals that are developed to take van der Waals interactions into account. There exist several different schemes for how to add dispersion into the current DFT approximations. The vdW-DF method proposed by Dion et al. [36] is the original functional accounting for dispersion interactions that is based directly on the electron density. This functional takes the form:

$$E_{xc} = E_x^{GGA} + E_c^{LDA} + E_{nl} \tag{2.20}$$

Here, E_x^{GGA} is the exchange energy, which uses the revPBE GGA functional [37], and the E_c^{LDA} is the correlation term, using the LDA approximation. The last term, E_{nl}, approximately accounts for the non-local correlations. Several functionals aiming at improving the original vdW-DF scheme, have further been proposed. Promising improved functionals are the 'opt' functionals, optPBE-vdW, optB88-vdW and optB86-vdW, for which the exchange functionals are optimized for the correlation term [38].

2.9 VASP

The Vienna *Ab initio* Simulation Package (VASP) [20–23] is used to perform the calculations in the present work. Hereunder is given a brief insight into how calculations are performed with VASP. More technical details about

the actual input parameters and example files can be found in Appendix A. Running a simulation in VASP requires four main input files.

- INCAR
- POSCAR
- KPOINTS
- POTCAR

The INCAR file is the file that contains most of the calculation spesifications. This file may contain a set of different tags determining how to initialize and run calculations, convergence criteria etc.

The POSCAR file contains the size and geometry of the supercell. The supercell is described by the vectors spanning the cell volume, and the fractional coordinates within this cell volume.

The KPOINTS file contains specifications for the k-point mesh projected onto the Brillouin zone. In this file one also specifies where the mesh should be centered within the BZ.

The POTCAR file contains information about the pseudopotential used. VASP provides a catalogue containing already calculated pseudopotentials for a large list of elements in the periodic table. Different pseudopotentials can also be chosen for each element.

Chapter 3

Materials and Background

In the present chapter important properties of graphene and GaAs are described. Special attention is given to the electronic properties of the respective materials and their implications with respect to atomic structure and functional properties.

3.1 Graphene

Graphene is a two dimensional material consisting of carbon atoms arranged in a honeycomb structure, where each atom is bound to three other atoms. Graphene is the basic unit for a vast number of different graphitic materials of different dimensionality: rolling up graphene sheets creates one dimensional nanowires, fullerenes are molecules that are simply wrapped up graphene sheets and stacking graphene layers on top of each other gives the 3D material graphite (Figure 3.2) [2]. Graphite exists in three different polymorphs, having the space groups $P6_3mc$, $P6_3/mmc$ and $R\bar{3}d$, respectively. These three polymorphs are very close in energy as they only differ in the stacking of the

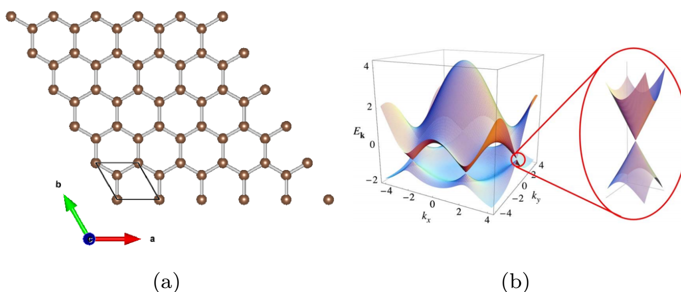

(a) (b)

Figure 3.1: ***(a)*** *Honeycomb structure of graphene.* ***(b) Ref.*** *[2] Bandstructure of graphene. The Dirac point, where the conduction band and valence band meet is shown in the circular frame to the right.*

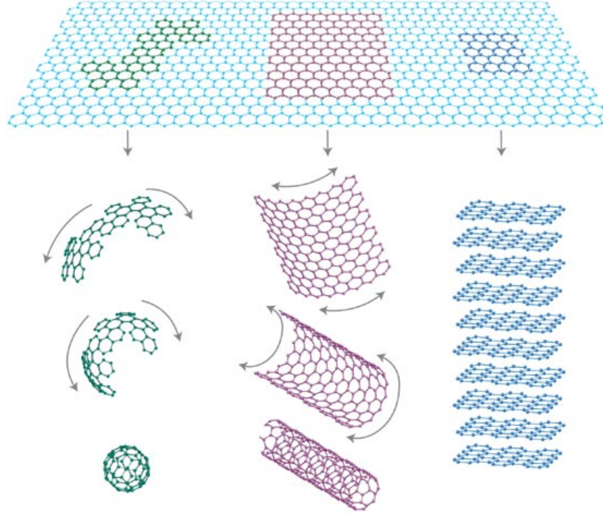

Figure 3.2: *Ref. [3]. Graphene is the basic unit for many different graphitic materials. A graphene sheet can be wrapped up to a fullerene, rolled up into a nanowire or stacked to form graphite.*

graphene sheets which are interacting only through weak van der Waals forces. Graphene, although known for several decades was not isolated until 2004, when Novoselov et al. [14] demonstrated preparation of thin graphitic sheets down to single layer graphene with of mechanical exfoliation, by the simple means of Scotch tape used to peel the graphene layers in graphite from each other.

Carbon is element No. 6 in the periodic table, thus containing 6 electrons, which in the atomic ground state is in the configuration $1s^2 2s^2 2p^2$. Each carbon atom in graphene is sp^2 hybridized, implying a mixing of the 2s and two 2p orbitals in carbon. The sp^2 hybridization gives rise to the trigonal, planar structure in graphene, where overlapping sp^2 orbitals create strong interplanar σ-bonds. The C-C bond length is 1.42 Å [2]. Each bond is separated by an angle of 120°. The remaining p orbital, the p_z orbital, points orthogonal to the plane. Overlap of neighbouring p_z-orbitals gives rise to the formation of π-bands. Each p_z-orbital contains a single electron, thus the created π-bands are half-filled [2]. The dispersion of the p_z-orbitals gives rise to formation of a bonding π-band (the valence band) and a higher energy anti-bonding π^*-band (the conduction band) [39]. The valence band and the conduction band touch at exactly six points, called the Dirac points or **K** points. These points are at the corners of the Brillouin zone. Thus, graphene is often in literature referred to as a zero-gap semiconductor. In the low energy regime, for low energy electron excitations, the bands have linear dispersion:

$$E = v_F \hbar |\mathbf{k}| \tag{3.1}$$

In equation 3.1 v_F is the Fermi velocity, $\hbar$ is the Planck constant scaled with

the $\frac{1}{2\pi}$ and $|\mathbf{k}|$ is the absolute value of the wave vector, near the **K** point. It turns out that the electrons in graphene behave like relativistic particles. The energy of a relativistic particle is given by:

$$E = \sqrt{(mc^2)^2 + (pc)^2} \tag{3.2}$$

where m is the particle restmass, c is the particle velocity and p its momentum ($p = \hbar|\mathbf{k}|$). Comparing this with equation 3.1, it is found that the electrons in graphene in the low energy limit (where the dispersion is linear) behave like massless particles, or Dirac Fermions [40]. This gives rise to many of the unusual properties of graphene. One interesting property of Dirac fermions is that they can escape the presence of localized potentials caused by e.g. impurities in the material, where ordinary electrons would be trapped. This enables such electrons in graphene to travel large distances, in the order of micrometers, without scattering [2].

Graphene is a highly flexible material. This is due to the out-of-plane phonon modes present, which one does not find in 3D materials [2]. The softness that graphene exhibits, has led to the investigation of graphene as an electronic membrane [41]. Due to its flexibility, rippling of the graphene sheet may occur, which again can alter the electronic structure of flat 2D sheets. One mechanism for altering electronic properties is rehybridization as a result of rippling [41].

3.2 GaAs

For this section the primary reference is Ref. [42].

Gallium Arsenide is a III-V binary semiconductor compound consisting of the group III element Gallium (Ga) and the group V element Arsenic (As). In bulk, GaAs attains the zincblende (ZB) crystal structure as seen in Figure 3.3. The ZB structure is a face centered cubic (FCC) lattice with a basis given by :

$$\vec{r_1} = [000], \quad \vec{r_2} = [\frac{1}{4}\frac{1}{4}\frac{1}{4}] \tag{3.3}$$

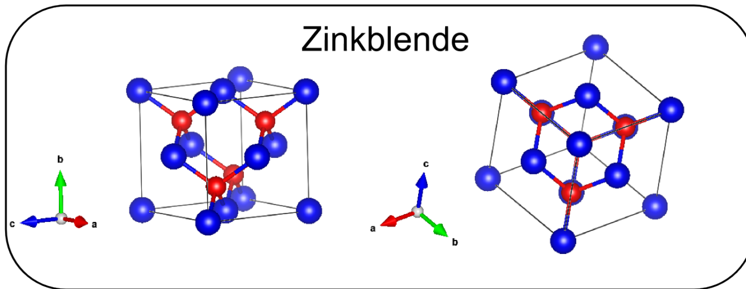

Figure 3.3: *Zincblende crystal structure. To the right the zincblende structure along its [111] direction is visualized. The in-plane hexagonal structure is apparent.*

The crystal binding in a material is highly dependent on the electronic structure of the specific material. Gallium has the electronic configuration [Ar]$3d^{10}4s^{2}4p^{1}$, whereas Arsenic has the configuration [Ar]$3d^{10}4s^{2}4p^{3}$. In the zincblende structure the atoms are tetrahedrally coordinated, in which each atom is bonded to four other atoms of the opposite element. This tetrahedral coordination is obtained through an sp^3 hybridization of the 4s and the three 4p orbitals of Ga and As. Overlap of these hybridized orbitals creates highly directional, covalent sp^3-bonds between the atoms in the crystal. Because Ga is a less electronegative element than As, As atoms pull more on the electrons in the sp^3-bonds. The covalent bonds thus have heteropolar character.

GaAs is a direct bandgap semiconductor. In general, semiconductors exhibit either a direct or an indirect bandgap. This is a feature related to the bandstructure of the material, which again is a characteristic depending on the energy dispersion in the material. The energy dispersion describes how the available energy states depend on the crystal momentum (the **k** vector). If the highest available energy in the valence band and the lowest energy in the conduction band is given for the the same crystal momentum, the semiconductor has a direct bandgap. If however these energies correspond to different wavevectors, the semiconductor has an indirect bandgap (Figure 3.4). This has implications for the light emitting and absorbing ability of the material. Materials that exhibit a direct bandgap, such as GaAs, have the ability to directly absorb and emit photons because electrons can be directly excited to the conduction band and recombine without any change in momentum. This is why GaAs in a promising material for applications within optoelectronics. However, for materials with an indirect bandgap, this is not directly possible; for excited electrons to re-enter the valence band, additional momentum needs to be transferred to the crystal lattice.

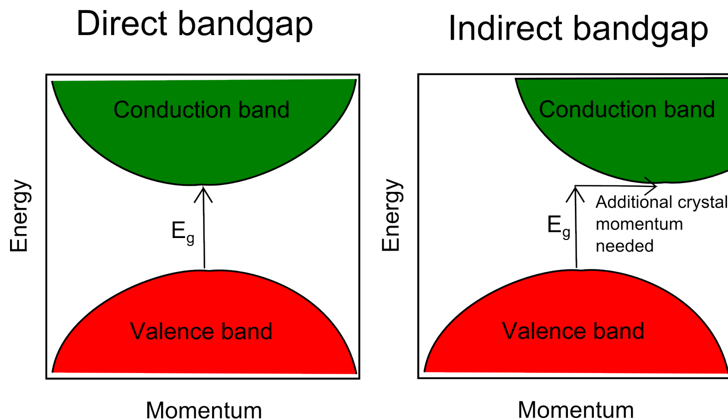

Figure 3.4: *Schematics illustrating a direct bandgap (left frame) and an indirect bandgap (right frame).*

Semiconductor nanowires

Semiconductor nanowires have caught attention because of unique electronic properties related to the structure of these quasi-one dimensional materials. The large aspect ratio of semiconductor nanowires induces very anisotropic properties [13, 43]. At the nanometer scale, electronic and optical properties may differ from the bulk material. Also the crystal structure may be affected by the reduced dimensionality. III-V nanowires show a ZB and WZ polymorphism [1, 16, 44]. Nanowires have a preferential growth along the [111]([0001]) crystallographic direction for cubic (hexagonal) crystals [45]. Because the ZB structure and the WZ structure are very similar along these directions, both exhibiting in-plane hexagonal symmetry, the polyomorphism is manifested in stacking faults and twin defects [13]. The crystallographic structure has impact on the electronic structure of the nanowires, and is thus very important to control for reproducibility of the electronic and optoelectronic performance [46].

3.2.1 Surface reconstruction

At the surface of a material, atoms may shift their position to minimize the surface energy. Whereas metals tend to simply relax the atomic positions at the surface, without any prominent structural changes, semiconductor materials tend to undergo surface reconstruction. This is because of the different nature of the bonds in metals and semiconductors, respectively. In metals, electrons are free to move around, whereas in semiconductors, the strong directionality of the covalent bonds limit the flexibility of the electrons to move. Surface reconstruction may involve large displacements of the atoms in the atomic layers closest to the surface, which involves a change in the periodicity at the surface compared to the bulk. The surface then normally exhibits a larger periodicity than its bulk. [47]

It is well established that GaAs(111) will reconstruct at the surface due to the high energy cost of having partially filled surface bonds [48]. There have been reported several different possible surface reconstructions that GaAs(111) surfaces can adopt, e.g. both 2×2 and $\sqrt{19} \times \sqrt{19}$ [17].

The GaAs(111) 2×2 Ga vacancy model

A vacancy buckling model presented by Tong et al [4] describes a 2×2 reconstruction on (111) surfaces on III-V semiconductor compounds.

In this model, a group III vacancy is present at the surface for every third group III element, giving rise to the 2×2 periodicity. Since the group III atoms present at the surface are bound to three other group V atoms, each vacancy present creates three group V dangling bonds, with which a charge of $\frac{5}{4}e^-$ is associated. Because of the vacancies present at the surface, there is an equal number of group III and group V dangling bonds. The highly unstable surface dangling sp^3-bonds associated with the group III elements, each having a charge of $\frac{3}{4}e^-$ associated with them, rehybridizes into sp^2 type orbitals in order to lower the surface potential energy. The sp^2 orbitals

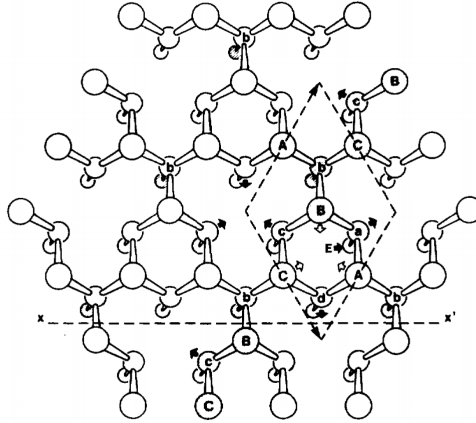

Figure 3.5: *Ref. [4] Top schematic view of the* 2×2 *vacancy buckling model. A, B and C denote surface Ga atoms, a,b,c and d are As atoms in the layer below. Atom E is a third layer Ga atom.*

are planar and form an orbital configuration where the angle between each orbital is approximately 120°. Thus the surface bilayer becomes flattened, because the surface group III elements move inward to form sp^2-orbitals. The group V elements on the other hand rehybridize to form three p-type orbitals, leading the surface bonds on the reconstructed surface to be a mix between sp^2-character and p-character. The model is experimentally supported by Tong et al. [4] by Low Energy Electron Diffraction (LEED) analysis of the GaAs (111) surface.

It is this 2×2 reconstruction that is assumed at the GaAs(111) surface in this work.

3.3 van der Waals interactions

van der Waals forces are expected to play an important role in studying the nature of interactions between GaAs and graphene at the interface. A short elaboration of the physical understanding of such forces is therefore included. The references used for the following section on van der Waals interactions are ref. [34] and ref. [42].

Van der Waals interactions occur as a consequence of the fact that the charge distribution around an atom is not fixed. In fact if the charge distribution around a neutral atom was homogeneously and spherically distributed around the atom, the potential around the atom would be zero, and an inert atom would not show any cohesion. However, the electronic charges in an atom moves around, and spontaneously induces dipole moments in the atom. This can further induce dipole moments in other atoms, thus causing an attractive force between the atoms. Modelling two atoms as harmonic oscillators, one can deduce that the attractive energy scales with the inverse of the atomic distance to the power of six:

$$\delta U = -\frac{A}{R^6} \tag{3.4}$$

where δU is the interaction energy, A is a constant factor and R is distance between the atoms. The vdW interactions are not dependent on any charge density overlap.

3.4 Previous DFT studies

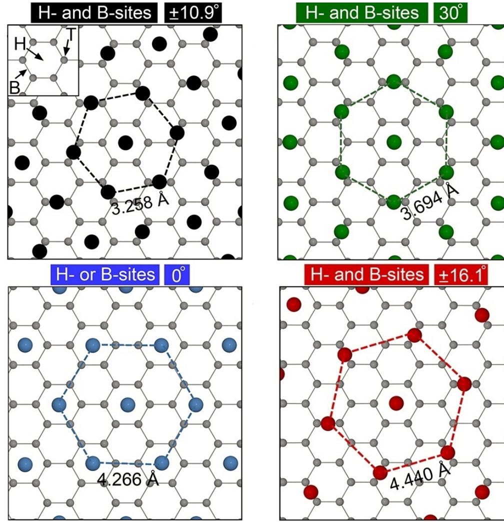

Figure 3.6: *Ref. [1] Epitaxial configurations of GaAs on graphene, proposed by Munshi et. al. A perfect epitaxial interface between GaAs and graphene is assumed. The interface Ga atoms on top of graphene are visualized. The dotted lines are guidance to the eye to help visualize the different relative phase orientations.*

There are limited DFT studies performed on semiconductor/graphene interfaces. Hong at al [16], who have also demonstrated growth of double heterostructure InAs/graphene/InAs have performed first principle calculations studying the InAs/graphene interface. They found that an InAs reconstructed interface with In vacancies is energetically more stable than the non-reconstructed interface in the In-terminated surface layer. Also, the equilibrium vdW heterointerface gap between the graphene layer and the InAs layer was found to be 3.1 Å. Yelgel et al. [15] have conducted a first principle investigation in the electronic properties and equilibrium geometry of graphene on InAs(111). From this study it was found that the equilibrium distance between the graphene and InAs(111) is 3.054 Å, thus in accordance with the findings of Hong et al. It is also found that the graphene layer buckles by 0.053 Å. Through band structure calculations it was shown that the system has metallic character. Adsorption of both In- and As-terminated InAs(111) was calculated, in which deposition of In terminated surfaces on

graphene was shown to be exothermic, whereas deposition of As-terminated surfaces was endothermic. This indicates that by growth of InAs on graphene, one would expect In-termination at the interface.

Munshi et al. [1] have presented a model for epitaxial growth positions of GaAs on graphene. Figure 3.6 shows the suggested atomic arrangements for GaAs(111) growth on graphene. This model assumes perfect epitaxy, and does only consider atomic positions of the interface semiconductor layer above a bridge between two carbon atoms and above the center of a hexagon in the graphene. The site right above a carbon atom is neglected in the model. This is based on previous DFT calculations by Nakada et al. [49] on adatom adsorption, finding that the top position is unfavourable for semiconductor atoms.

Chapter **4**

Computational details

In the present chapter computational details for the calculations performed during the present project are described. All calculations were performed with VASP[20–23], and the Projector Augmented Wave (PAW) method [50] was used throughout all calculations.

This chapter contains three main sections. First, details on calculations performed on bulk GaAs and graphite are described, second, the construction of GaAs slab supercells and all related calculation details are described, and third, details related to heterostructure calculations are elaborated.

4.1 Bulk GaAs and graphite

In order to understand the interface between GaAs and graphene, it is necessary to fully understand the properties of the individual materials. Therefore calculations on both bulk GaAs and graphite were performed.

For all bulk GaAs calculations the VASP 5.3.3 version was used, and calculations were performed with the PBEsol functional [51]. The potentials Ga_d(s^2p^1) and As(s^2p^3) were used, supplied with VASP. The Ga_d potential includes the Ga d electrons, and this potential is chosen for a slight improvement in the accuracy of the calculations. Electron wave functions were expanded in plane waves up to a kinetic energy cutoff of 400 eV. For this choice of cutoff energy, an energy convergence within 1 meV was achieved, as seen from cutoff-convergence testing (Figure 4.1).

4.1.1 Straining of bulk GaAs

The effect of biaxial straining of bulk GaAs zinkblende (ZB) within the (111) crystallographic plane and bulk GaAs wurtzite (WZ) within the (0001) plane was studied. These specific planes were studied because they are the planes perpendicular to the preferred growth directions of GaAs nanowires grown on graphene, in the ZB and WZ structure, respectively. This is due to the fact that graphene exhibits an in-plane hexagonal symmetry, as does the

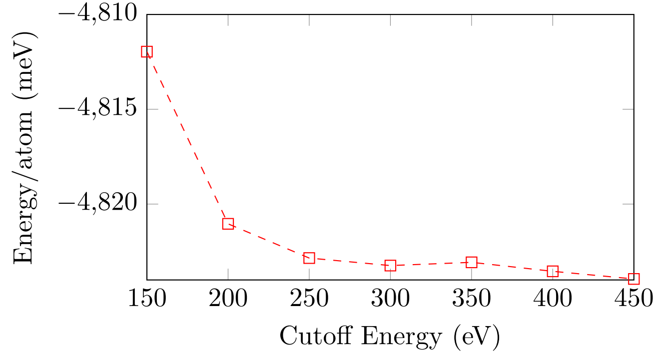

Figure 4.1: *Total energy per atom as function of cutoff energy for GaAs. Calculations are performed with PBEsol. The PAW potentials Ga_d(s^2p^1) and As(s^2p^3) are used.*

(111) plane in the ZB structure and the (0001) plane in the WZ structure. The unit cell for the WZ structure is seen in the frame to the left in Figure 4.2. For the ZB structure, a supercell was constructed for which the (111) plane corresponds to the supercell *ab*-plane and the *c* parameter accordingly corresponds to the [111] direction, as illustrated in the frame to the right in Figure 4.2.

Initial fully relaxed supercells of WZ and (111) oriented ZB were calculated, with a self-consistent field (SCF) convergence energy of 1.0×10^{-9} eV. k-point convergence testing was done, seen in Figure 4.3. The Brillouin zone was sampled for both WZ and ZB supercells with a $12 \times 12 \times 8$ Γ-centered k-point mesh, which gave total energies per atoms converged well within 1 meV. Structural relaxations of unit cell volumes and atomic coordinates were performed until all Hellmann-Feynman forces on the ions converged to a level below 0.001 eV/Å.

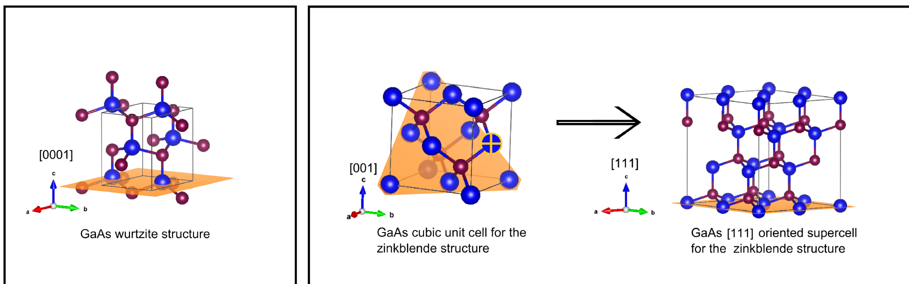

Figure 4.2: *Visualization of the WZ structure and the ZB structure. In the left panel, the unit cell for WZ is shown, for which the (0001) plane is highlighted in orange. In the right panel, the cubic unit cell for the ZB structure is shown, for which coordinates have been transformed to obtain a [111] oriented cell. The (111) plane is highlighted in orange in both the cubic cell and the rotated supercell.*

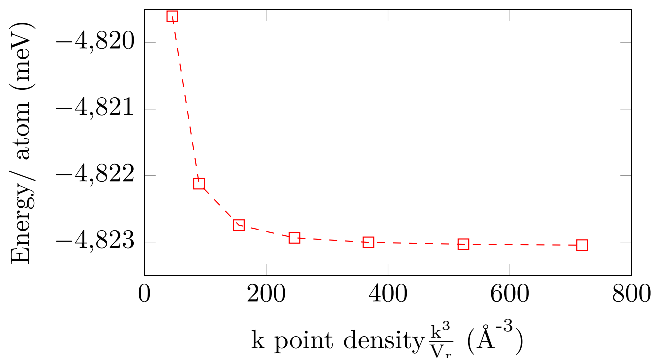

Figure 4.3: *Total energy of GaAs per atom as function of k-point density, with a cutoff energy of 400 eV. The density is given as the total number of k-points (k), scaled with the reciprocal unit cell volume (V_r). Calculations are performed with PBEsol. The PAW potentials Ga_d(s^2p^1) and As(s^2p^3) are used.*

Biaxial strain calculations were performed with a special version of VASP, an "*ab*-fix" version, where the a and b supercell lattice parameters are kept fixed and the c parameter is allowed to change during cell volume relaxation. This version of VASP is compiled for the specific purpose of being able to relax the total volume in only one dimension. Thus, during strain calculations, the a and b parameters were successively decreased and increased, and for each successive step the c parameter was free to relax. Calculation parameters were the same as described for initial structural relaxations. For further details on calculation parameters, see the INCAR file for these calculations (Appendix B.1.1)

4.1.2 Density of states calculations of bulk GaAs

Density of states (DOS) calculations were performed on fully relaxed, unstrained WZ and ZB structures. For the ZB structure, a cubic supercell was used as seen in Figure 4.2, for which the Brillouin zone was sampled with a $10 \times 10 \times 10$ Γ-centered k-mesh, corresponding to a k-point density with total energy per atom well converged within 1 meV/atom.

DOS calculations were performed in two steps. Firstly, a calculation was performed for which a self-consistent charge density was calculated and written. In this run, an SCF convergence energy of 1.0×10^{-9} eV was used, and the supercell volumes and all atomic positions were kept fixed. In the second calculation step, the charge density was kept fixed. This step is a non-SCF calculation, for which the charge density was fixed to the density obtained from the former SCF-run. During this run, all k-points were treated independently. The k-point densities were increased to $24 \times 24 \times 16$ for WZ and $24 \times 24 \times 24$ for ZB, for increased calculation accuracy. The INCAR files for the two calculation steps are included in Appendix B.1.2.

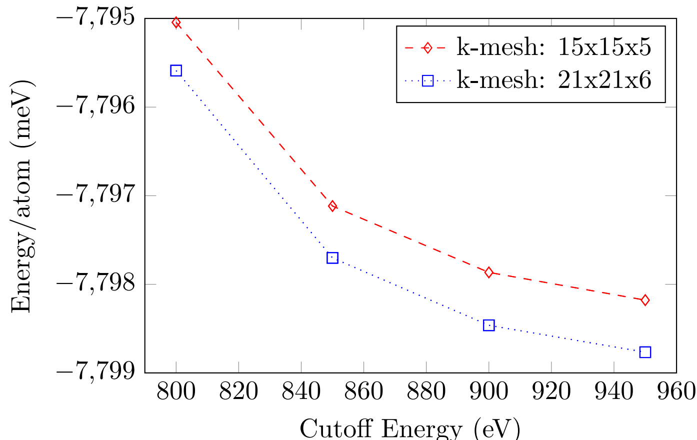

Figure 4.4: *Total energy per atom for graphite $P6_3mc$ as function of cutoff energy. Calculations are performed with the optPBE functional, with PAW potential C_h(s^2p^2). Cutoff testing is performed with two different Γ-centered k-meshes, as indicated in the figure.*

4.1.3 Density of states calculation of graphite

DOS calculations of graphite $P6_3mc$ were performed. These calculations were performed with the optPBE functional [35], using the potential C_h(s^2p^2). The _h implies that this is a hard potential. It is thus more accurate, however it requires a higher cutoff energy than standard potentials. A hard carbon potential was used as calculations with standard carbon potential (C(s^2p^2)) did not sufficiently converge with optPBE. Full cell volume relaxations were initially performed. Electron wave functions were expanded in plane waves up to an energy cutoff of 910 eV, which in accordance with convergence testing yielded energy convergence within 1 meV/atom, as seen in Figure 4.4. The Brillouin zone was sampled with a $15 \times 15 \times 5$ Γ-centered k-mesh. A $21 \times 21 \times 6$ sampling was tested as well, differing in energy from the $15 \times 15 \times 5$ sampling with less than 1 meV/atom. The INCAR file for cell volume relaxation is included in Appendix B.2.1.

DOS calculations for graphite were performed similarly to the above described procedure for GaAs. In the self-consistent calculation step the Brillouin zone was sampled with a $15 \times 15 \times 5$ Γ-centered mesh and this was increased to $18 \times 18 \times 6$ in the the second run, to achieve higher accuracy. The INCAR files for the two calculation steps are included in Appendix B.2.2

4.2 GaAs surface reconstruction

4.2.1 Construction of supercells for modelling surface reconstruction

The supercell that is constructed to model GaAs(111) 2×2 surface reconstruction is to a large extent based on the slab model of GaAs presented by

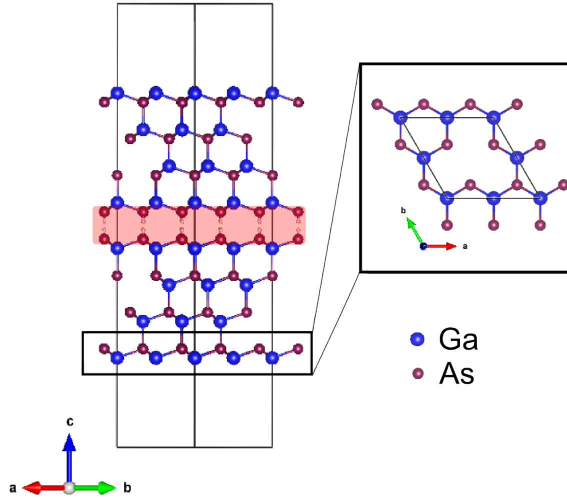

Figure 4.5: Visualization of the constructed supercell with a GaAs symmetric double-slab and an artificial midlayer, where the As-atoms at the midlayer interface are saturated with 0.75e$^-$ pseudo-hydrogen. The midlayer interface is shaded in red. The atoms within the red shaded area are kept fixed throughout all calculations due to large repulsive forces. In the box to the right the interface bilayer is also viewed along the c direction of the cell.

Kaxiras et al. [52].

The construction of a slab model in order to reproduce a 2x2 surface reconstruction of GaAs(111) is not straight forward, and poses a few computational challenges. Firstly, all calculations are performed with periodic boundary conditions. This implies that the supercell structure is being periodically repeated throughout space. In order to model a surface within a supercell, a GaAs slab is constructed with a vacuum region above and below the slab within the supercell. However, simply carving GaAs along its (111) plane will render two different polar surfaces on each side of the slab, one being As-terminated ([$\bar{1}\bar{1}\bar{1}$] direction) and the other being Ga-terminated ([111] direction). Due to periodic boundary conditions, the different polarity of two different surfaces on the slab will create an artificial field that will affect the surface reconstruction [52]. This is due to the different states of the dangling bonds on the As-terminated surface and the Ga-terminated surface, respectively, which with periodic boundary conditions would lead to charge transfer between the different surfaces [52].

In order to avoid such artificial fields, a mirror symmetry is imposed onto the GaAs slab. Thus, instead of having a single slab, a double slab is constructed (Figure 4.5). The mirror symmetry ensures that the same surface is exposed on both sides of the slab. In the present model, Ga is the surface terminating layer on both sides of the slab. When imposing this non-physical

mirror symmetry onto the slab, creating a double slab, there will be two same-atom planes (in our model these are As-planes) at the interface, in the middle of the double slab as seen in Figure 4.5. The As-dangling bonds at the interface are saturated with 0.75e$^-$ pseudo-hydrogen. This is done to avoid charge buildup at the interface which would also lead to a charge transfer from the interface to the slab surface. The reason for this is that each As dangling bond at the interface have a $\frac{5}{4}$e$^-$ charge associated with them, since As has a valence of five and the atoms are all sp^3 hybridized. Bond formation of two such orbitals would lead to an excess charge of $\frac{1}{2}$e$^-$ in an anti-bonding state, that would transfer to the surface region because of the lower laying state of the dangling Ga-bonds, for which a charge of $\frac{3}{4}$e$^-$ is associated with each dangling bond. This charge transfer is avoided by saturating the As-bonds in the interface region with pseudo-hydrogen having a charge of 0.75e$^-$.

The double slab consists of two times eight layers, thus two times four Ga-layers and As-layers respectively, as is seen in Figure 4.5. The supercell consists in total of 30 Ga atoms, 32 As atoms and 8 pseudo-hydrogen atoms. The two excess As atoms as compared to the number of Ga atoms are due to the two vacant Ga sites associated with the two Ga-surfaces on the double slab. The bond-lengths are initially set to the literature value of bulk GaAs, 5.653 Å [53].

For the purpose of comparison in further calculations, also a GaAs slab supercell without Ga vacancies present at the surface is constructed. This supercell therefore has two more Ga atoms present, one for each of the two surfaces on the slab. Apart from this, the supercell construction is identical to the double-slab supercell previously described. The latter supercell will be referred to as the bulk-terminated slab.

4.2.2 Computational scheme for relaxation of supercell

The constructed double slab model with Ga vacancies was relaxed in order to obtain a (111) 2×2 reconstructed surface structure. The calculations were performed with the VASP 5.3.3 version. The calculations were performed with the PBEsol functional, and the PAW potentials Ga_d, As and .75H, supplied with VASP, were used. The Ga_d potential includes the *d* orbital for Ga. The .75H pseudo-hydrogen has a valence of 0.75e$^-$. As for bulk GaAs, electron wave functions were expanded in plane waves up to a kinetic energy cutoff of 400 eV. The electronic convergence criterion was set to a SCF energy of 1.0×10^{-9} eV. The supercell volume was fixed, whereas atomic positions were allowed to relax. However, selective dynamics was used to fix the atomic coordinates of the As atoms and the pseudo-hydrogens in the midlayers of the double slab, due to the here present strong, repulsive forces. Because of the unavoidable, strong forces at the midlayer interface in the double slab, ionic relaxation was done with a convergence criterion which considers the total energy within the supercell, rather than forces acting on each atom individually, in order to get convergence. Convergence testing with different k-point densities and different values for the convergence criterion of the total supercell energy was done, seen in Figure 4.6. The Brillouin zone was

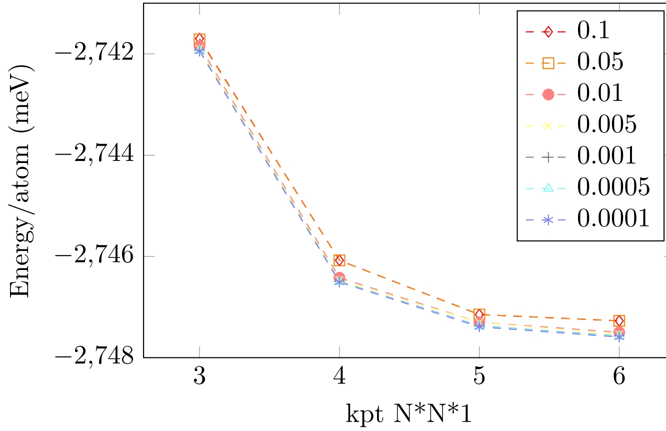

Figure 4.6: *Total energy per atom for different restrictions of the atomic convergence criterion for GaAs double-slab supercells. The numbers given in the legend are the total energies, in eV, that the supercell energy must be converged within. The convergence testing is performed with fixed cell volume. Calculations are peformed with the PBEsol functional with the PAW potentials Ga_d(s^2p^1), As(s^2p^3) and .75H.*

sampled with a $4 \times 4 \times 1$ Γ-centered k-mesh, giving energy convergence within a few meV/Å. Different values for the ionic convergence criterion yielded small energy differences, and visual inspection of the resultant structures after relaxation revealed no visually detectable structural alteration for convergence criteria lower than 0.01 eV/Å. Atomic coordinates varied within an order of magnitude of 10^{-3}Å. The INCAR file for supercell relaxation is included in Appendix B.3.1.

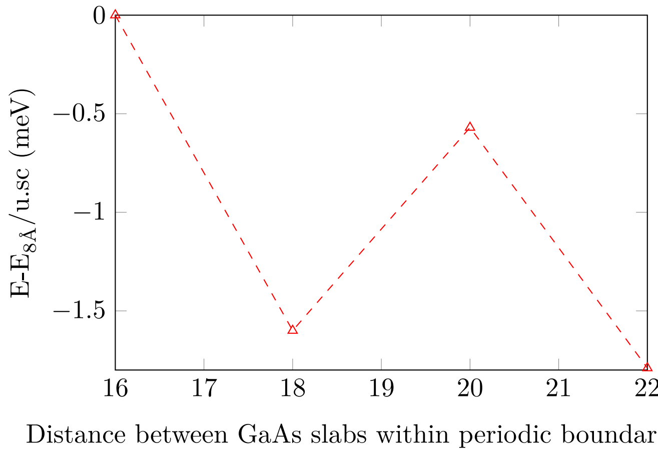

Figure 4.7: *Total GaAs slab supercell energy as function of distance between the periodically repeated GaAs slabs.*

In order to assure that the vacuum is sufficiently large such that the periodically repeated GaAs-slabs do not interact with each other, test calculations were performed where the vacuum regions were successively increased, and no significant change in energy was detected. The *total* supercell energy varied within a few meV for testing of larger vacuum regions than the initial 2×8 Å, seen in Figure 4.7. No further structural change could be observed by visual inspection.

4.2.3 Chemical potential of solid Ga and graphite

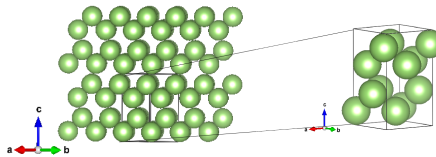

Figure 4.8: *Crystallographic structure of orthorombic Ga metal.*

For the purpose of calculating the surface reconstruction energy of GaAs(111)-2×2 surfaces with Ga vacancies, the chemical potential of Ga was calculated. The chemical potential of solid Ga is simply the energy per atom in the equilibrium Ga(s) structure. At ambient conditions Ga is a metal with orthorombic crystal structure, as seen i Figure 4.8.

The PAW potential Ga_d was used, supplied with VASP, and calculations were performed with the PBEsol functional. The Brillouin zone was sampled with a Γ-centered $12\times12\times8$ grid, giving converged energies within 1 meV/atom. Electron wave functions were expanded up to a kinetic energy cutoff of 400 eV. Relaxations were performed with a SCF energy of 1.0×10^{-9} eV and until Hellmann-Feynman forces on all atoms have reached a value below 0.001 eV/Å. Different settings for the partial occupancies of the wavefunctions were tested. In the INCAR file this corresponds to the ISMEAR tag. Gaussian smearing (ISMEAR = 0) and the method of Methfessel-Paxton [54] for order 1 and 2 (ISMEAR = 1 and ISMEAR = 2, respectively) were tested, for two different σ-values, i.e. smearing widths. This is shown in Figure 4.9. The different smearings yielded values for chemical potential of Ga varying within 0.1 meV. The INCAR file for the Ga metal relaxation is included in Appendix B.3.2.

4.2.4 *ab*-plane straining of GaAs slab

The effect of biaxial straining in the *ab*-plane of the GaAs slab supercell was tested. *ab*-plane straining was performed for GaAs slabs both with surface reconstruction and with bulk-termination. The calculation parameters were equal for both systems and equal to the calculation parameters for relaxation of the GaAs reconstructed slab (see Section 4.2.2). Thus, for each strain calculation, all ions within the supercell were allowed to relax except from the midlayer pseudo-hydrogen-terminated As atoms. Also, the *c* parameter

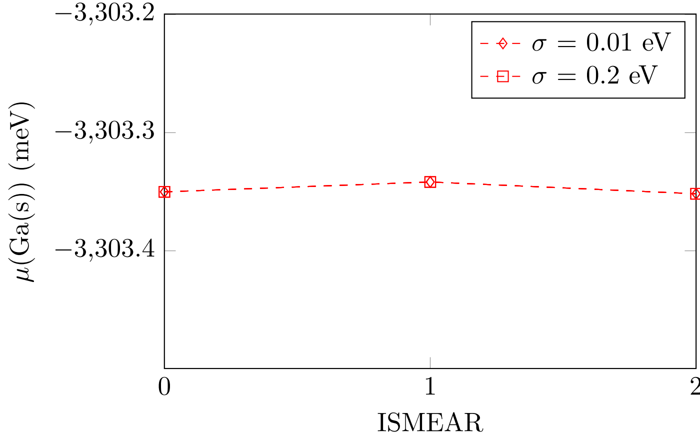

Figure 4.9: *Chemical potential for Ga(s) calculated with different smearing methods and smearing widths. The x axis values 0, 1 and 2 correspond to Gaussian smearing and the method of Methfessel-Paxton of order 1 and 2, respectively.*

was kept constant for all values of strain. The slabs were strained up to 15% both in compressive and tensile mode.

4.2.5 GaAs slab DOS calculations

DOS calculations were performed on GaAs slabs both in relaxed and strained conditions. The calculation procedure was the same as described in Section 4.1.2, thus a two step calculation scheme, with a selfconsistent and a non-selfconsistent run. In the first run the Brillouin zone was sampled with a $4 \times 4 \times 1$ Γ-centered mesh, whereas this was increased to a $5 \times 5 \times 1$ Γ-centered mesh in the second run. Calculation parameters were otherwise the same as for DOS calculations on bulk GaAs.

4.3 Heterostructure calculations

4.3.1 The heterostructure supercells

Five different atomic configurations at the epitaxial interface between graphene and GaAs are proposed. These configurations are described by the epitaxial model presented by Munchi et al [1]. However, in this model a bulk terminated GaAs surface at the interface is assumed. Here, it is proposed that the GaAs (111) surface at the GaAs/graphene interface is 2×2 reconstructed according to the vacancy buckling model described in Section 3.2.1. The five structural configurations that are proposed are shown in Figure 4.10. There are three different suggested relative rotations between graphene and GaAs; a 0°, 16.1° and 30° phase orientation relative to graphene. The different orientations correspond to the relative rotations of the in-plane hexagonal pattern of the interface Ga atoms and graphene respectively. For the 0° orientation, three in-plane translations are considered; one in which all interface Ga atoms are positioned right above a carbon atom, one in which the interface Ga atoms are situated above a C-C bond and one where the Ga atoms are placed above the middle of the hexagonal ring in graphene. Based on the positioning of the interface Ga atoms, these configurations will be referred to as Top (T), Bridge (B) and Hollow (H) configurations, respectively (Figure 4.11). For the 16.1° and the 30° orientations, only one translation is considered. This is due to the fact that these configurations cannot be translated such that all the interface Ga atomic positions are situated on either a Top, Bridge or Hollow site, which are the ones here considered. For these two orientations, all the Ga atoms at the interface are at bridge sites.

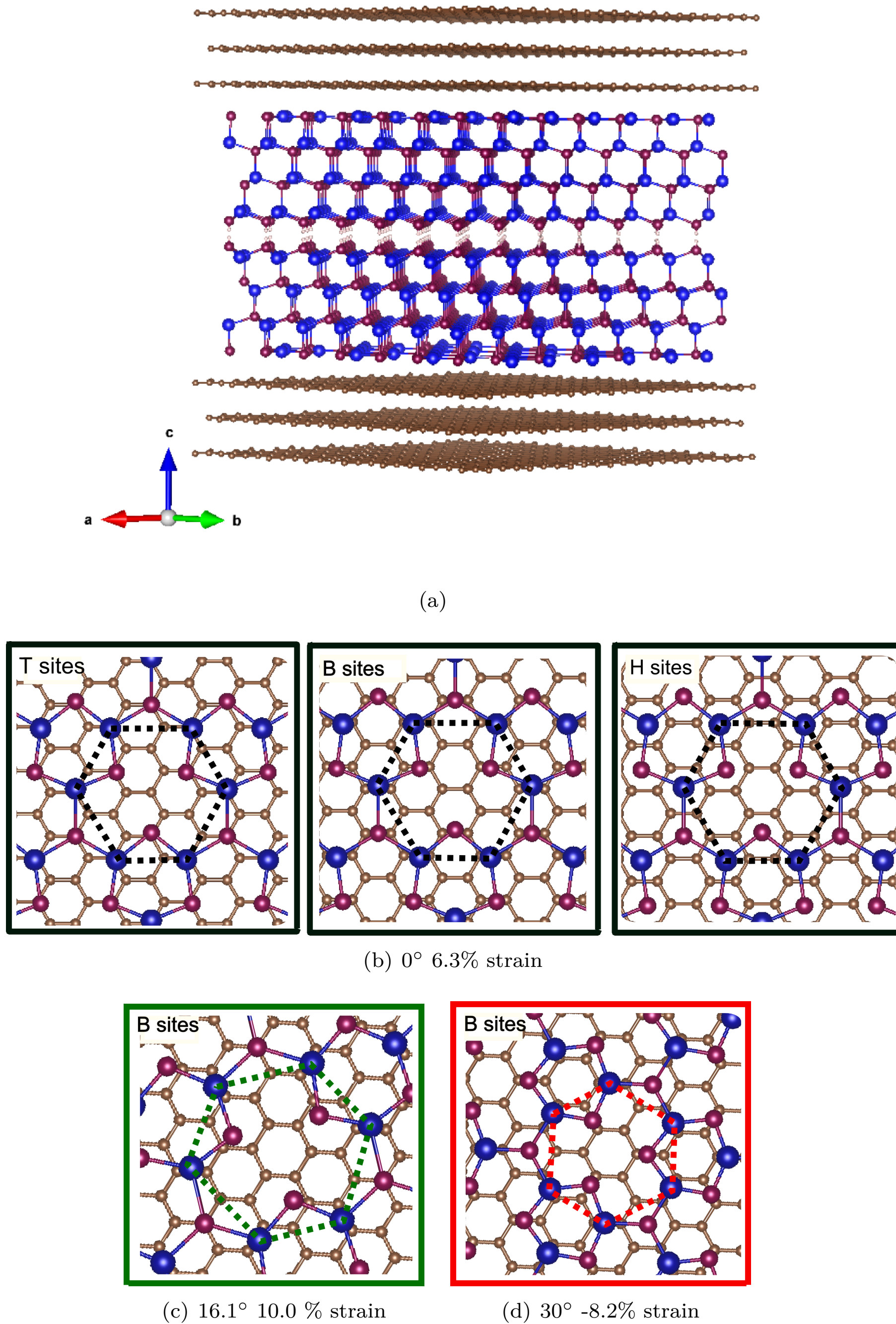

Figure 4.10: ***(a)*** *Heterostructure slab, periodically extended in the ab-plane for visualization. The GaAs slab is the GaAs reconstructed structure obtained after relaxation.* ***(b)***, ***(c)*** *and* ***(d)*** *The five different configurations considered of GaAs on graphene. The dotted lines are meant as a guidance for the eye to visualize the hexagonal pattern of the interface Ga atoms, and the relative rotation of this with respect to graphene.*

The supercell is constructed by placing three graphene layers above and below the relaxed GaAs double slabs, and thereafter strained to accommodate different lattice mismatches (described in Section 4.2). Initially, in employing conventional semi-local functionals during calculations, the supercells contain an 8 Å vacuum region above and below the graphene layers, to reassure no interaction between the periodically repeated GaAs slabs. However, in calculations performed with vdW functionals these two vacuum regions are removed. Due to the fact that such functionals are non-localized, they are computationally more demanding, and the computational work-load depends on the filling of the cell, thus scaling with the amount of vacuum in the cell. Therefore, in order to reduce computational load, the vacuum regions are removed from the supercells.

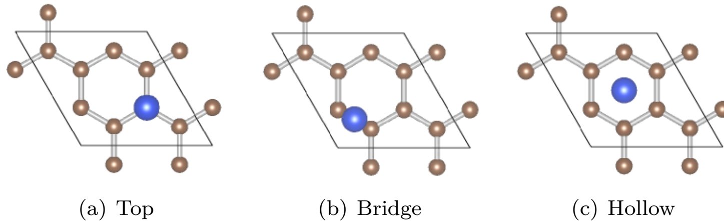

(a) Top (b) Bridge (c) Hollow

Figure 4.11: *Different sites on graphene, top, hollow and bridge sites respectively.*

4.3.2 Computational scheme for heterostructure calculations

During all calculations performed on heterostructure supercells the VASP 5.3.5 version was used. This simply is an upgraded version of VASP that was released during the course of the present study, and has no influence on the results of this present work. The standard PAW potentials Ga(s^2p^1) and As(s^2p^3) were used along with .75H pseudo-hydrogen, for the atoms within the GaAs slab. Changing the Ga potential from Ga_d(s^2p^1) to standard Ga(s^2p^1) was only done to save computational work load, as the the size of the supercell itself along with the number of atoms within the cells make calculations computationally demanding.

Coarse geometry optimization - energy mapping as function of GaAs/graphene distance

Evaluation of functionals was performed on the heterostructure supercells by evaluating the total energy of the supercells as function of distance between graphene and GaAs. The conventional, semi-local PBEsol functional and the vdW functional optPBE were both evaluated. For optPBE, both standard carbon potential (C(s^2p^2)) and hard carbon potential (C_h(s^2p^2)) were tested. For calculations on pure graphite using optPBE, the hard carbon potential was necessary to use in order to get sufficient energy convergence. However, as the hard potentials are computationally much more demanding than standard

potentials, and because of the computationally demanding system under study, the effect of applying standard carbon potential as compared to hard ones was of interest to investigate.

In calculations with standard C potential, electron wave functions were expanded to a kinetic energy cutoff of 550 eV. This cutoff was set based on the default energy cutoff provided with the PAW potential supplied with VASP (which is 400 eV), and then increased by 30%. For calculations with hard carbon potential, the cutoff energy was set to 910 eV, as for bulk graphite calculations. The Brillouin zone was sampled with a Γ-centered k-point grid of $2 \times 2 \times 1$. Static calculations were performed for which no ionic relaxation was allowed to occur. The SCF energy convergence criterion was set to 1.0×10^{-6} eV. For calculations with the PBEsol functional, during which the supercells have vacuum regions both below and above the heterostructure slabs, the graphene layers for each calculation with varying distance were subsequently shifted a distance further away from the GaAs slab without altering the cell volume. Internal bond lengths within the GaAs slab were kept constant. However, for calculations performed with the vdW functional optPBE, the vacuum regions were removed, as explained earlier. Thus in order to increase the GaAs slab/graphene distance, the cell volume was forced to successively expand in the c-direction of the supercells. The internal relative coordinates were rescaled for each calculation such that internal bond lengths were kept constant. The GaAs/graphene distance was varied from 1 Å to 5 Å, with a step length of 0.2 Å.

Based on the functional testing, all further calculations performed on heterostructure supercells were done with optPBE and standard carbon potential.

The energy mapping as function of distance between GaAs and graphene yielded an equilibrium distance for which the total supercell energy was the lowest. This equilibrium distance changed for the two different functionals, but both calculation runs performed with optPBE (with standard and hard carbon potential, respectively) yielded the same equilibrium position. In an effort to fine tune this equilibrium distance, a second calculation run was performed for which a smaller step length was used. Calculation parameters were the same as described above for optPBE calculations with standard carbon potential. The interval of distance for which energy was mapped was 0.4 Å around the equilibrium distance established through the former calculations. The steplength was 0.04 Å. The INCAR file for static calculations is included in Appendix B.4.1.

Fine geometry optimization

Following the static energy mappings, dynamic relaxations at the interface were performed. The starting points for the structural relaxations were the most energetically favourable structures with respect to GaAs/graphene distance for the different configurations. The optPBE functional was applied with standard carbon potential. During relaxation, selective dynamics was used to fix all atoms except from the interface GaAs bilayer along with all

graphene layers, which were allowed to move in x, y and z directions. A Γ-centered k-point grid of $2 \times 2 \times 1$ was used to sample the Brilloiun zone along with a cutoff energy of 550 eV. The convergence cristerion for the SCF energy was set to 1.0×10^{-6} eV and ions were let to relax until the total energy had reached a value below 0.01 eV. As for relaxation of the single GaAs slabs, an ionic convergence criterion based on the *total* energy chosen due to the strong forces within the GaAs slab, and also because we here consider an *interface* between two materials. Forces at the interface are considerably stronger than forces on atoms in bulk materials. The INCAR file for dynamic calculations is included in Appendix B.4.2.

4.3.3 Density of states calculations

DOS calculations were performed for dynamically relaxed structures (described in Section 4.3.2). In order to calculate accurate DOS, two calculation steps were performed, as described in Section 4.1.2. In the first SC run a k-point grid of $2 \times 2 \times 1$ was used to map the Brillouin zone, which was increased to $4 \times 4 \times 1$ in the second non-self-consistent run. The cutoff energy was 550 eV, and the SCF energy convergence criterion was set to 1.0×10^{-6} eV. INCAR files for the two DOS calculations are found in Appendix B.4.3.

Chapter 5

Results

In this chapter the results of the present work are presented. The chapter is divided into three main sections. In the first section bulk GaAs and graphite are studied, respectively. Following the bulk calculations is the modelling of and calculations performed on GaAs reconstructed supercells. Last in this chapter, the results of the investigation of heterostructure interfaces are presented.

5.1 Bulk GaAs and graphite

5.1.1 Straining of bulk GaAs

The energy penalty of biaxial straining of bulk GaAs, both zincblende (ZB) and wurtzite (WZ), is studied. Since there is a lattice mismatch between graphene and GaAs in the preferred growth directions of GaAs on graphene ([111] and [0001] for the ZB and WZ structure, respectively), epitaxial growth would require GaAs to strain to some degree in these planes to adopt to graphene. During the project work [5], it was established that the energy penalty of in-plane straining of graphene is much higher than that associated with isotropic straining of GaAs. Therefore, it is assumed that graphene at the interface will not be significantly strained. This can be seen in Figure 5.1, taken from the project work [5], which shows the increase in energy as GaAs is isotropically compressed and expanded and the increase in energy for an in-plane compression and expansion of graphene. The curvatures of the graphs indicate the relative stiffness of the two materials. Thus, graphene is considerably harder to strain.

In the present work, the energy penalty of an *ab*-plane strain of the ZB(111) and WZ(0001) planes is studied. That is a more realistic modelling of the GaAs strain penalty at the interface than isotropic straining, because of the ability of the nanowires to relax the structure in the direction perpendicular to the interface as a response to *ab*-plane strain. Figure 5.2 shows the energy as function of *ab*-plane straining for bulk GaAs ZB and WZ structures

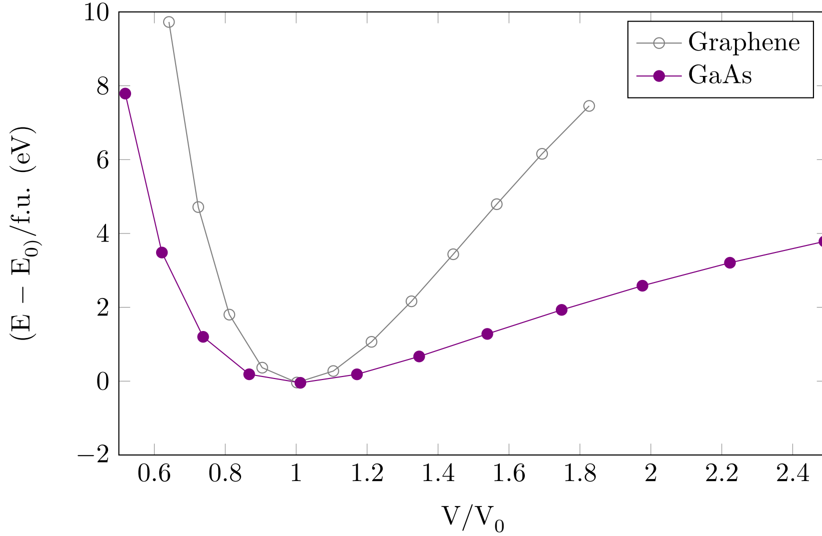

Figure 5.1: *Ref. [5] Results from project work. Energy per formula unit calculated as a function of normalized volume, where V_0 is the volume given by the equilibrium lattice constant for the respective materials. The energy is given relative to the energy at zero strain. Calculations are performed with the LDA functional.*

along with the energy difference between the two respective crystallographic structures. GaAs ZB, which is the energetically favourable structure in unstrained condition, becomes even more favourable with respect to WZ as the material is being strained. However, for compression of the material, WZ is slightly more energetically favourable. The relaxed *c* parameter for WZ, and the corresponding *c'* parameter for the [111] oriented ZB cell are plotted in the lower panel in Figure 5.3. Figure 5.4 shows the supercells for WZ and [111] oriented ZB. Because the ZB structure in the [111] crystallographic direction is ABC stacked, the *c* parameter in the constructed [111] oriented ZB cell includes three bilayers of GaAs. The WZ structure, on the other hand, is AB stacked in the [0001] direction, thus the supercell includes two bilayers. For comparison of the lattice parameters, the *c'* parameter is therefore rescaled to $\frac{2}{3}$. There is a prominent perpendicular response to the *ab*-plane straining, as seen in Figure 5.3. The response of ZB and WZ is very similar, but for increasing strain, the bond lengths perpendicular to the strained plane in ZB decrease slightly more than for WZ.

5.1.2 Orbital resolved DOS for GaAs and graphite

For the purpose of having a reference of bulk electronic structure for GaAs and graphite as compared to the slab systems and heterostructures which will be addressed later on, density of states (DOS) calculations are performed for both GaAs and graphite.

Orbital resolved DOS is calculated for both the ZB and the WZ structure

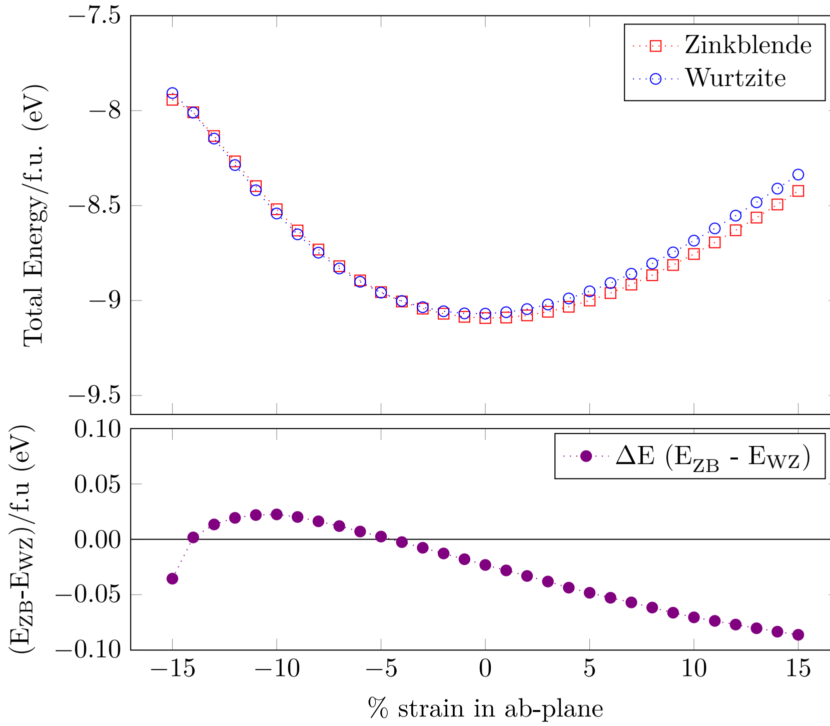

Figure 5.2: *Straining in the ab-plane of GaAs ZB(111) and GaAs WZ(0001). The c parameter in the supercell is free to relax, whereas the a and b parameters are kept fixed for each strain value.* ***Upper panel:*** *Energy per formula unit as function of percentage strain.* ***Lower panel****: Energy difference between ZB and WZ as function of strain.*

of GaAs, in non-strained conditions, as seen in Figure 5.5. Both structures exhibit a bandgap, as expected since GaAs indeed is a semiconductor. The top of the valence band is dominated by As (p) states, whereas the bottom of the valence band is slightly dominated by Ga (s) states for both ZB and WZ. This is in accordance with expectations for a material with polar covalent bonding: In the sp^3 hybridized bonds, the less electronegative Ga atoms donate electrons to the more electronegative As. The calculated bandgaps are summarized in Table 5.1 along with the literature values for bulk GaAs ZB. Close to the Fermi level of the calculated DOS for WZ, it can be seen in Figure 5.5 that the As (p) states exceed the total DOS. Thus, the orbital contributions obviously don't add up to the calculated total DOS. This can, however, be explained by numerical errors in the projection method used to obtain orbital resolved DOS.

Figure 5.6 shows the orbital resolved DOS for graphite $P6_3mc$. The p orbitals have been split up in p_x, p_y and p_z orbitals, as these are highly inequivalent. The s, p_x and p_y orbitals are sp^2 hybridized to form the strong intra-planar σ-bonds within each layer, and all the state contributions from these orbitals are heavily buried at energies much lower than the Fermi level.

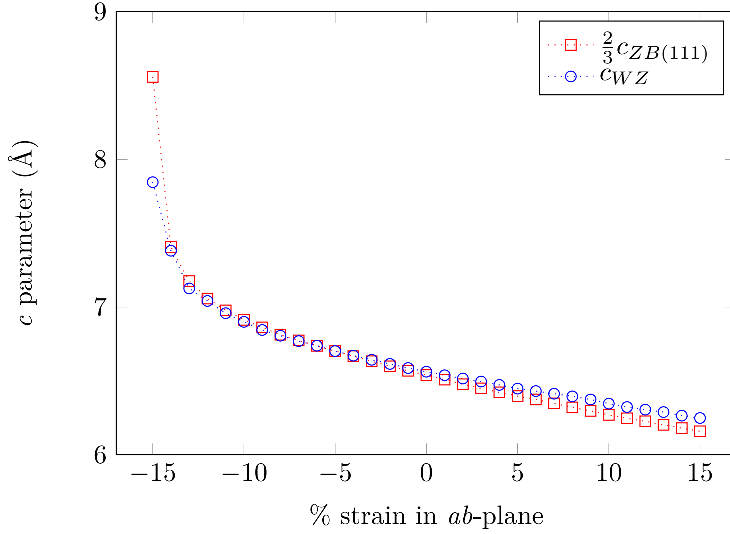

Figure 5.3: *Relaxed c parameter for GaAs WZ and corresponding c' parameter for ZB as function of ab-plane strain. The c' parameter is rescaled with $\frac{2}{3}$ for direct comparison with the WZ c parameter.*

However, the p_z orbital, which is oriented perpendicularly to the graphene sheets dominates the top of the valence band and the conduction band, as expected, as this is in full accordance with theory.

5.1.3 Bandgap evolution of GaAs(ZB) as function of *ab*-strain

How the bandgap of ZB GaAs is affected by the *ab*-plane strain studied in Section 5.1.1 has been investigated. Figure 5.7 shows the evolution of the bandgap of ZB GaAs as function of *ab*-strain in the (111)-plane. The bandgap peaks at two percent compressive strain, but decreases fast as the compressive strain increases. For tensile strain, the bandgap is also significantly reduced as

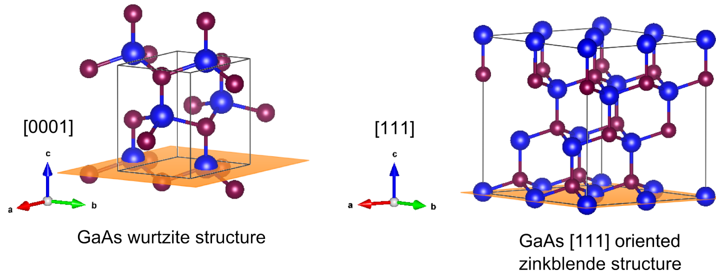

Figure 5.4: *Supercell structures for bulk WZ GaAs and [111] oriented ZB GaAs. The GaAs structure is rotated for the purpose of making the ZB(111) plane equivalent to the ab-plane for the purpose of ab-strain calculations.*

the tensile strain increases. Some deviation from the tendency of decreasing bandgap for increasing tensile and compressive strain is observed for some strain values, where the bandgap slightly increases. However, these deviations are attributed to not fully converged calculations, and is not a physically significant result, owing to the clear overall tendency of bandgap evolution seen in the graph.

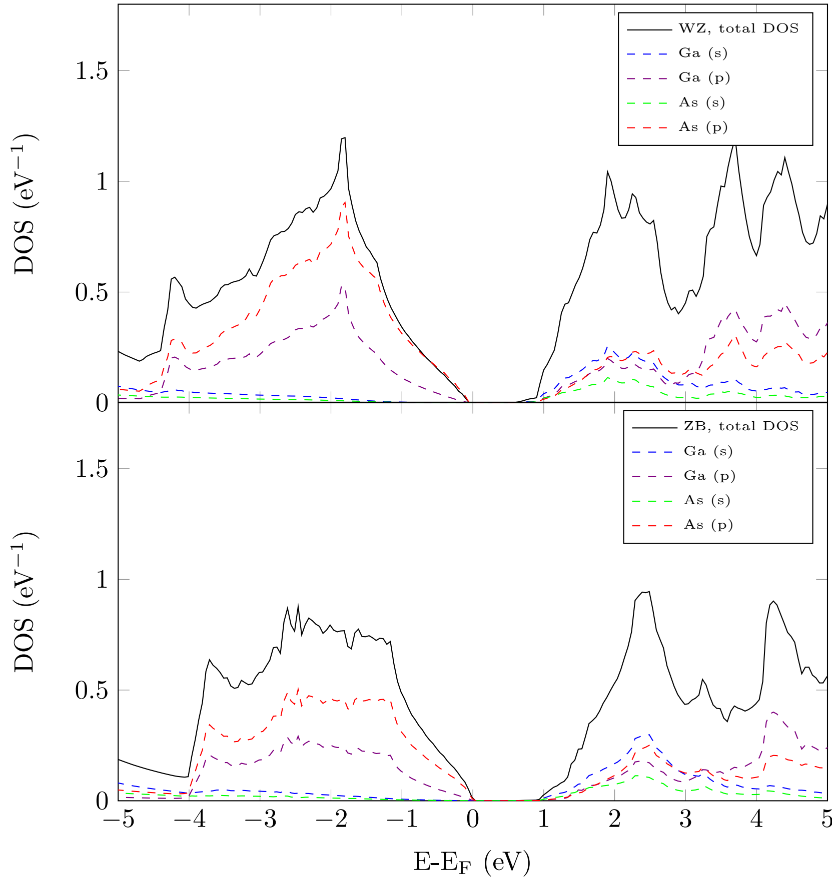

Figure 5.5: *Calculated density of states (DOS) for bulk GaAs, per formula unit (f.u.). Upper figure shows the orbital resolved DOS for the wurtzite (WZ) structure and the lower figure shows the orbital resolved DOS for the zincblende (ZB) structure.*

Table 5.1: *Calculated bandgaps for GaAs zincblende (ZB) and wurtzite (WZ) at zero strain.*

Crystal structure	Bandgap (eV)
ZB	0.424
WZ	0.449
ZB (literature value)	1.52 (0 K) [34]

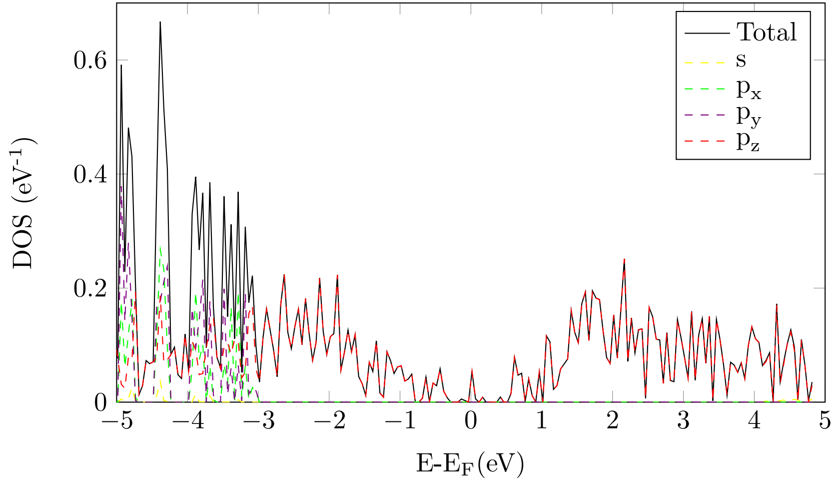

Figure 5.6: *Orbital resolved density of states for grapite $P6_3mc$. The DOS is plotted per formula unit (f.u.).*

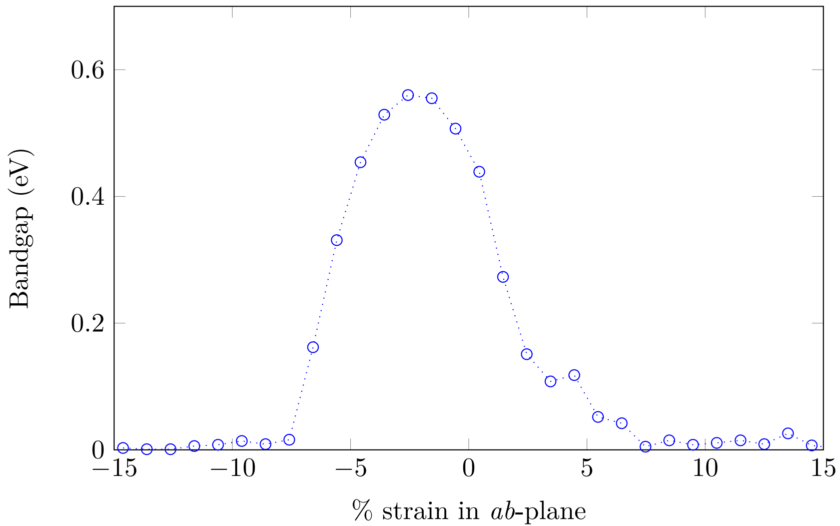

Figure 5.7: *Bandgap as function of percentage strain of GaAs zincblende structure in the (111) plane. In the supercell, the (111) plane spans the ab-plane, which is kept fixed during relaxation. The c parameter is free to relax.*

5.2 GaAs surface reconstruction

A reconstruction of the GaAs(111) surface at the GaAs/graphene interface is assumed. This assumption is based on the observed and reported very strong driving force for ZB GaAs(111) surfaces to reconstruct [17]. Only a 2×2 reconstruction has been considered here, described by the vacancy buckling model [4].

Relaxation of the GaAs double slab described in Section 4.2 yields a slab structure that is seen in Figure 5.8. Figure 5.8(a) shows the full double slab, both with and without surface reconstruction, for comparison. The slabs are periodically extended in the *ab*-plane for better visualization. Figure 5.8(b) visualizes the outermost bilayer in two different orientations for the surface reconstructed slab, which has flattened extensively compared to the bulk bilayer atomic structure. This is in accordance with the vacancy buckling model described in the literature [4], as this is a visual indicator of the predicted rehybridization of the atoms within the interface bilayer. In bulk, the Ga and As atoms are sp^3 hybridized. However, as predicted by the model of Tong et al. [4], the orbitals of the surface group III atoms, thus the Ga atoms, rehybridize to form sp^2 bonds, which are planar. This rehybridization removes electrons from the initial dangling bonds at the surface and puts them onto neighbouring As atoms. The present vacancies render the surface As atoms with some partially filled orbitals which again enable the transfer of electrons between the surface Ga atoms and the surface As atoms.

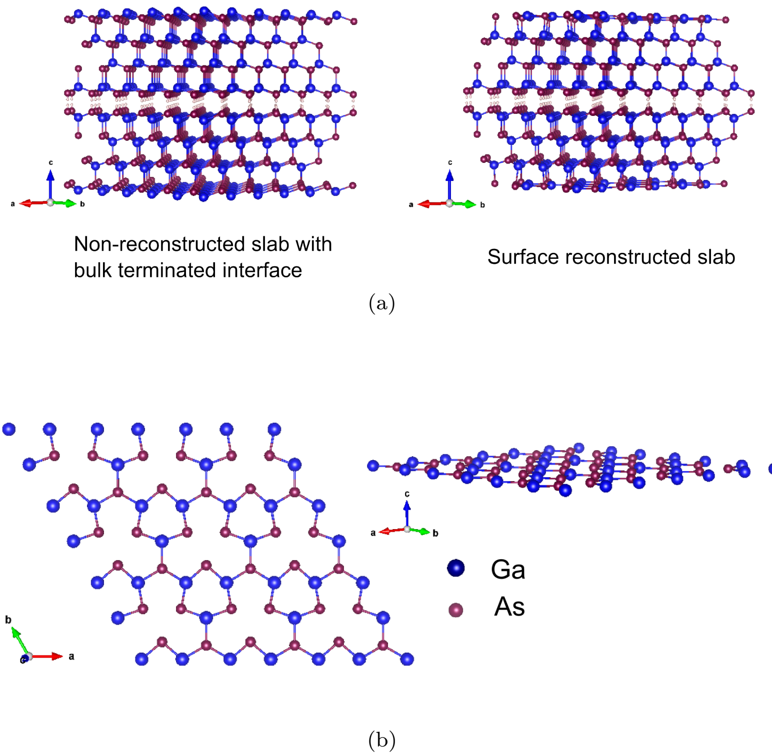

(a)

(b)

Figure 5.8: *Relaxed GaAs reconstructed slab, with Ga surface vacancies. (**a**) The whole GaAs slab is visualized, periodically extendend in the ab-plane. (**b**) In the figure to the left, the surface GaAs bilayer of the relaxed reconstruced surface is viewed along the c-axis of the supercell. In the figure to the right a sideview of the surface GaAs bilayer is shown, visualizing the flattening of this layer.*

5.2.1 Local density of states

Local density of states (LDOS) is calculated for three different bilayers of the GaAs double-slab reconstructed supercell. The different regions for which LDOS is calculated is depicted in Figure 5.9; the three outermost GaAs bilayers, respectively. The innermost GaAs bilayer, for which As is terminated with 0.75e$^-$ pseudohydrogen, is not studied as this layer is considered not to provide any physically significant information because of the artificial slab construction. Figure 5.10 shows the total LDOS for the three respective bilayers.

In Figure 5.11 the orbital resolved DOS of the three different regions is visualized. All three layers exhibit a bandgap. However, DOS of the three bilayers are not the same. Bilayer 1 and 2 exhibit a bandgap of 0.30 eV, whereas bilayer 3 exhibits a bandgap of 0.25 eV. Thus, the size of the bandgaps are smaller in the GaAs double slab than for bulk ZB (see Table 5.1). In the interface bilayer (bilayer 1), the As (p) orbitals dominate the valence band, whereas right above the Fermi level, thus in the conduction band, Ga (p) states dominate. For the uppermost bilayers (bilayer 2 and 3), the As (p) orbitals are also dominating the valence band, however, not as prominently as seen for bilayer 1.

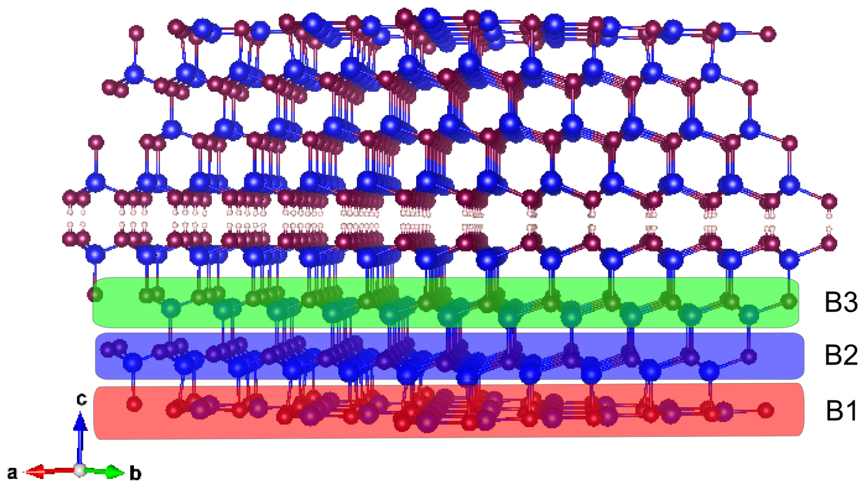

Figure 5.9: *Local DOS (LDOS) regions. B1, B2 and B3 are bilayer 1 (the surface bilayer) bilayer 2 and bilayer 3, respectively.*

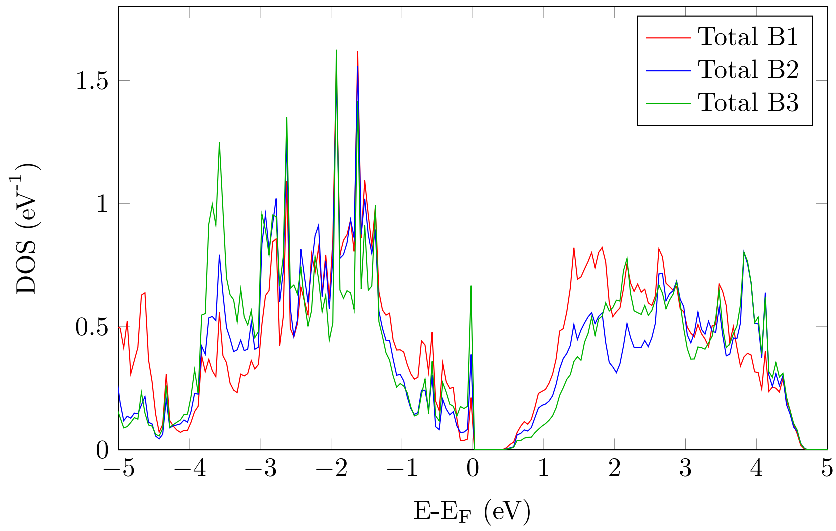

Figure 5.10: *Local DOS per formula unit (f.u.) calculated for reconstructed slab model. The regions corresponding to B1, B2 and B3, respectively are visualized in Figure 5.9.*

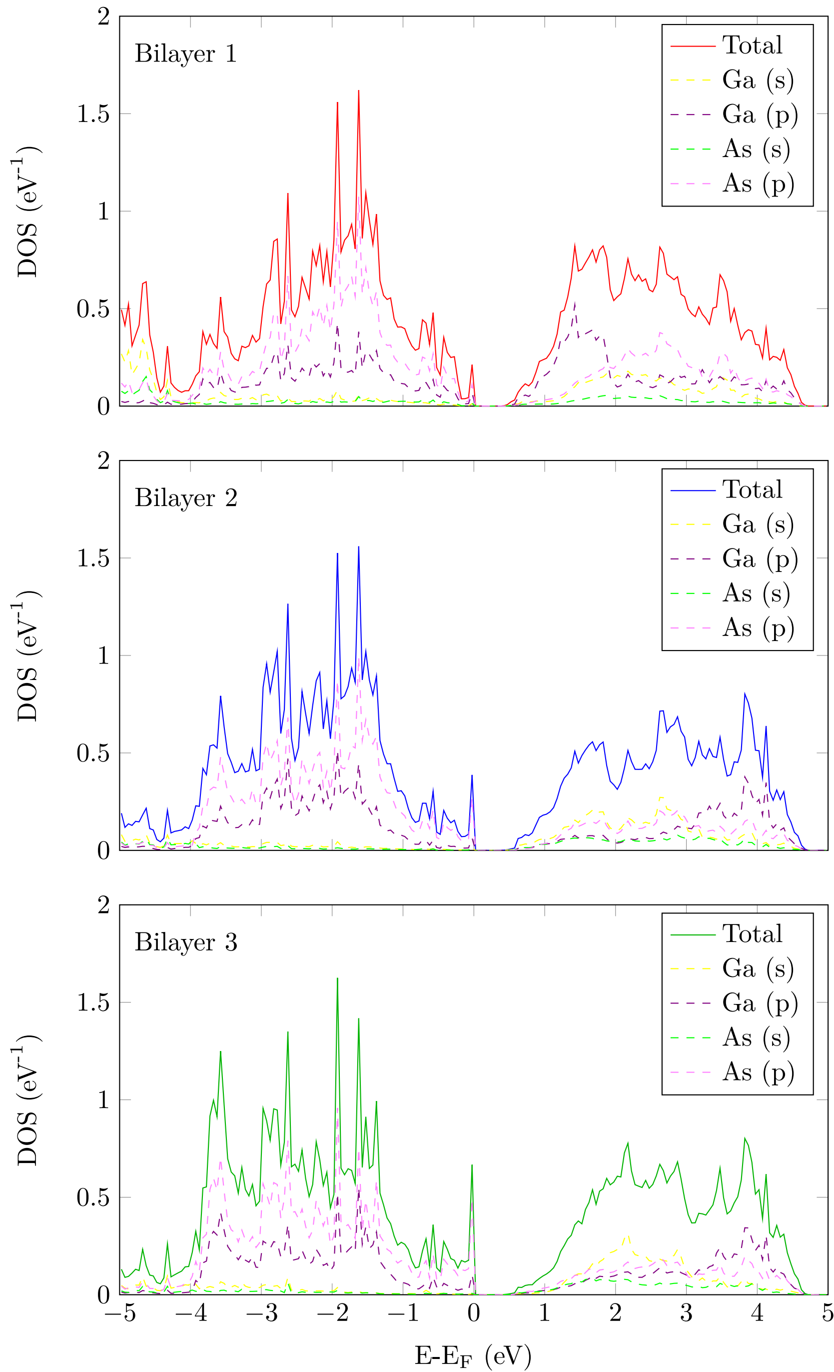

Figure 5.11: *Orbital resolved local DOS per formula unit (f.u.) for the regions indicated in Figure 5.9.*

5.2.2 GaAs reconstruction energy

The reconstruction energy of the GaAs(111)-2×2 surface with Ga vacancy is given by the following equation:

$$E_{rec} = \frac{1}{2}\left[E_{rel,vac} - E_{ref} + 2\mu_{Ga}\right] \tag{5.1}$$

Here E_{rec} is the reconstruction energy and $E_{rel,vac}$ is the relaxed slab structure with Ga vacancies, thus for which reconstruction has taken place at the surface. E_{ref} is the initial slab structure with no Ga vacancies present, for which the surface configuration of the double slab is the bulk GaAs configuration and all bond-lengths correspond to literature bulk values. μ_{Ga} is the chemical potential of Ga in its reservoir. At ambient conditions Ga is a metal in solid phase. The chemical potential of Ga is added to the equation in order to attain mass balance. The factor 2 associated with the chemical potential is due to the double slab structure containing two surface Ga vacancies. This is also the reasoning for the factor $\frac{1}{2}$, as the energy difference inside the brackets is associated with the formation of two reconstructed surfaces.

The calculations yield a value for the reconstruction energy of 2.33 eV per 2×2 unit cell.

5.2.3 Reconstruction energy for strained GaAs(111) surfaces

Energy as a function of in-plane straining of the *ab*-plane for reconstructed and non-reconstructed slabs is calculated. Figure 5.12(a) shows the total free energy of strained supercells; reconstructed supercell and non-reconstructed supercell with a bulk-terminated surface, respectively. Two times the chemical potential of Ga metal is added to the supercell with a reconstructed GaAs slab, for comparison of energies. The reconstruction energy is plotted as function of strain in Figure 5.12(b). Between a compressive strain of 12% and a tensile strain of 11%, the reconstruction energy is negative, thus, a reconstruction is favourable. For some critical strain value the slope of the energy difference between reconstructed and non-reconstructed supercell changes. At a compressive strain of 8%, the energy gain of having a reconstructed surface significantly decreases. The reconstruction energy is largest at a compressive strain of 7%. At a tensile strain of 7%, there is a jump in the reconstruction energy. The abrupt changes in reconstruction energy coincides with sudden curvature changes for the bulk-terminated structure, as seen in Figure 5.12(a). This is thus an indication of abrupt structural changes in the structure of the bulk-terminated slabs.

The structures of bulk-terminated slabs are investigated for the strain-regions -6% to -10% (compressive strains) and 5% to 9% (tensile strains). Figure 5.13 shows the bulk-terminated structures within the mentioned strain regions. In the upper frame, structures which are strained in tensile mode are shown. The slab structure contracts in the direction perpendicular to the strain. The outermost bilayer, highlighted in Figure 5.13, where there are unsaturated dangling bonds, flattens, as for structures which are surface reconstructed. Thus the outermost Ga atoms pull further in towards the

adjacent As layer. Between a strain level of 7% and 8% the outermost Ga atoms are shifted further in towards the bulk than the outermost As atoms in the interface bilayer. Structures within the compressive strain region are seen in the lower frame. The opposite structural change is observed. The double slab expands in the direction perpendicular to the strained plane. However, from a compressive strain of -8% to -9%, the interface bilayers abruptly expand, as the interface Ga atoms are heavily pulled outwards, away from the bulk.

Three different orientations of the GaAs phase on graphene are considered for the heterostructure calculations. These orientations have each a different lattice mismatch with respect to graphene, and thus the different epitaxial configurations require different degrees of strain in the GaAs phase. It is assumed that graphene is in a non-strained state at the interface. In the three different relative phase orientations of GaAs and graphene that are studied, 0°, 16.1° and 30°, respectively, the *ab*-plane strain is summarized in Table 5.2. As calculated for bulk GaAs, the size of the bandgap is highly sensitive to strain. In fact the DOS for slabs at the level of strain corresponding to the three different phase orientations (seen in Figure 5.14) show that for all three strain levels and for all bilayers 1, 2 and 3 (see Figure 5.9) the bandgap is lost.

Table 5.2: *Relative GaAs/graphene phase orientations and their associated strain level.*

Orientation	0°	16.1°	30°
Strain	+6.3%	+10.0%	-8.2%

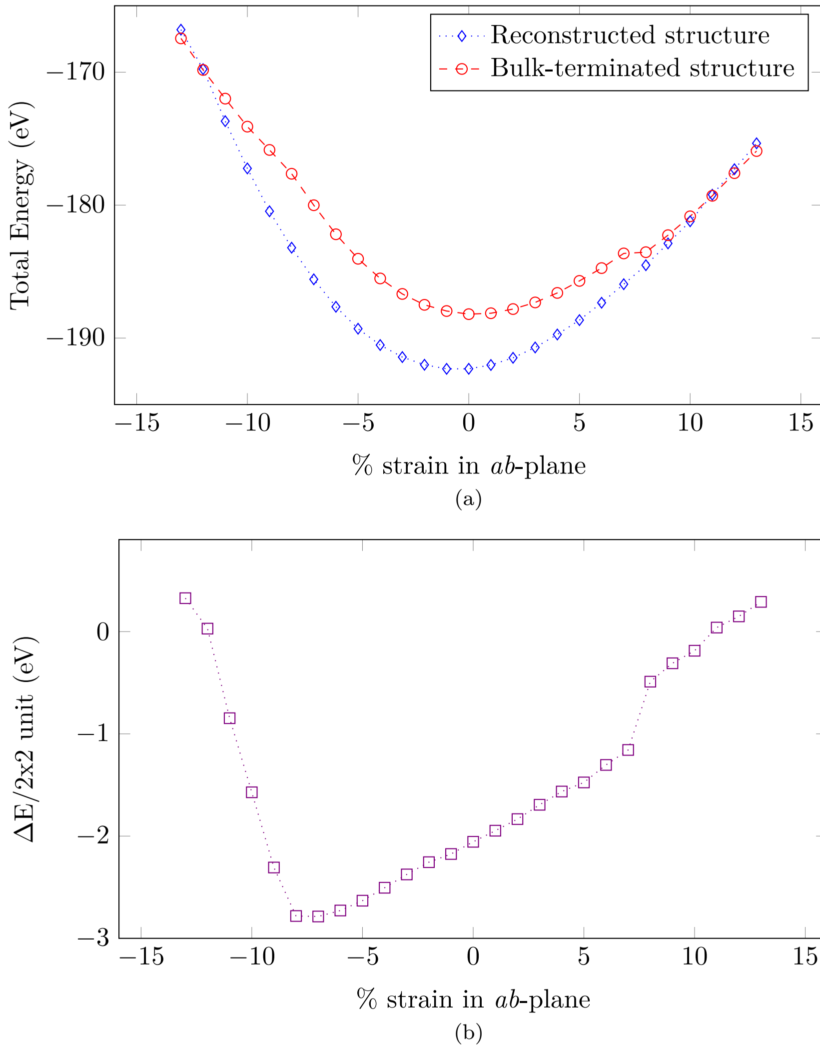

Figure 5.12: *(**a**) Total energy per unit supercell (u.sc) as function of ab-straining for reconstructed and bulk-terminated supercells. For relative energy comparison,* $2 \times \mu(Ga(s))$ *is added to the total energy of the reconstructed supercell. During straining of the supercells, the a and b vectors are altered whereas the c parameter is kept fixed. Selective dynamics is used, where the midlayer As and pseudo-hydrogen atoms are kept fixed, and all other atoms are free to relax. (**b**) Reconstruction energy as function of strain.*

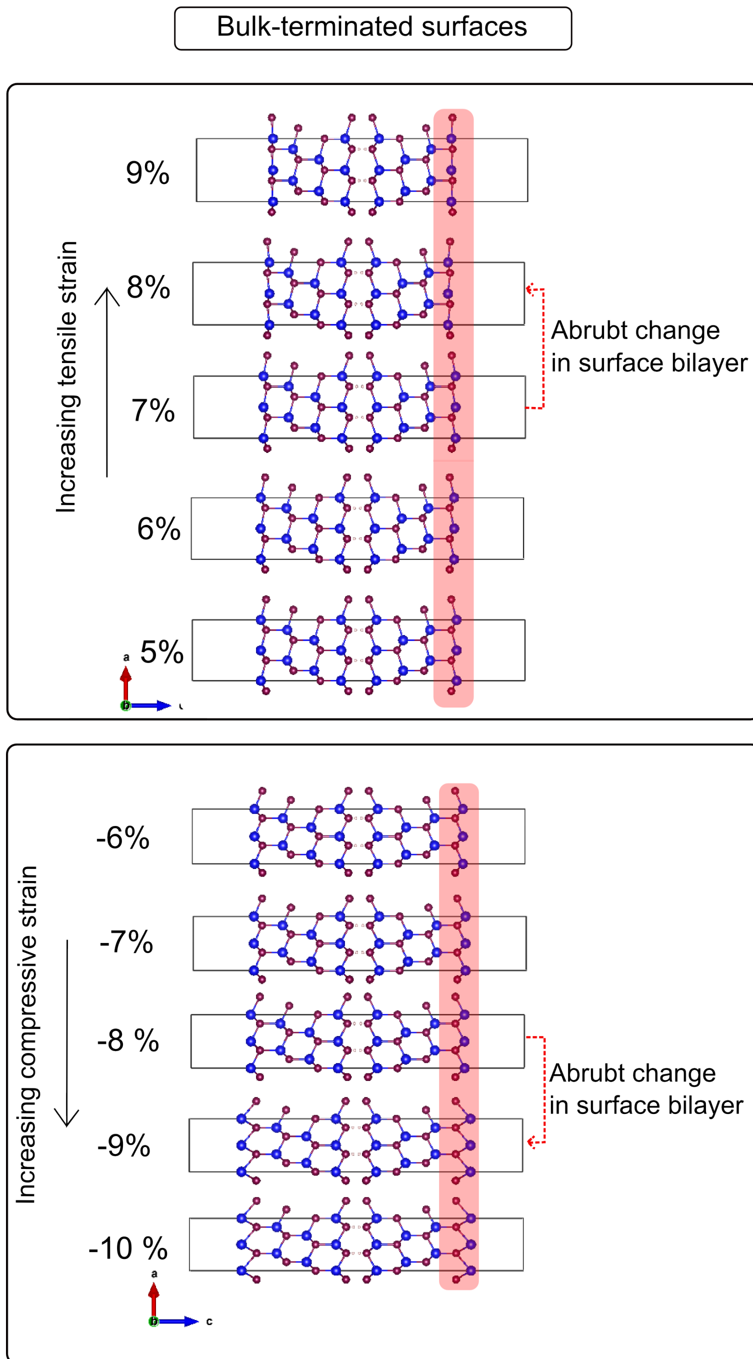

Figure 5.13: *Visualization of the structures for strained and relaxed bulk-terminated structures in the strain-regimes , 5% to 9% (tensile strain), seen in the upper panel, and -6% to -10% (compressive strain), seen in the lower panel. The evolution of strains within the given regimes show abrupt structural alterations, which are indicated in figures.*

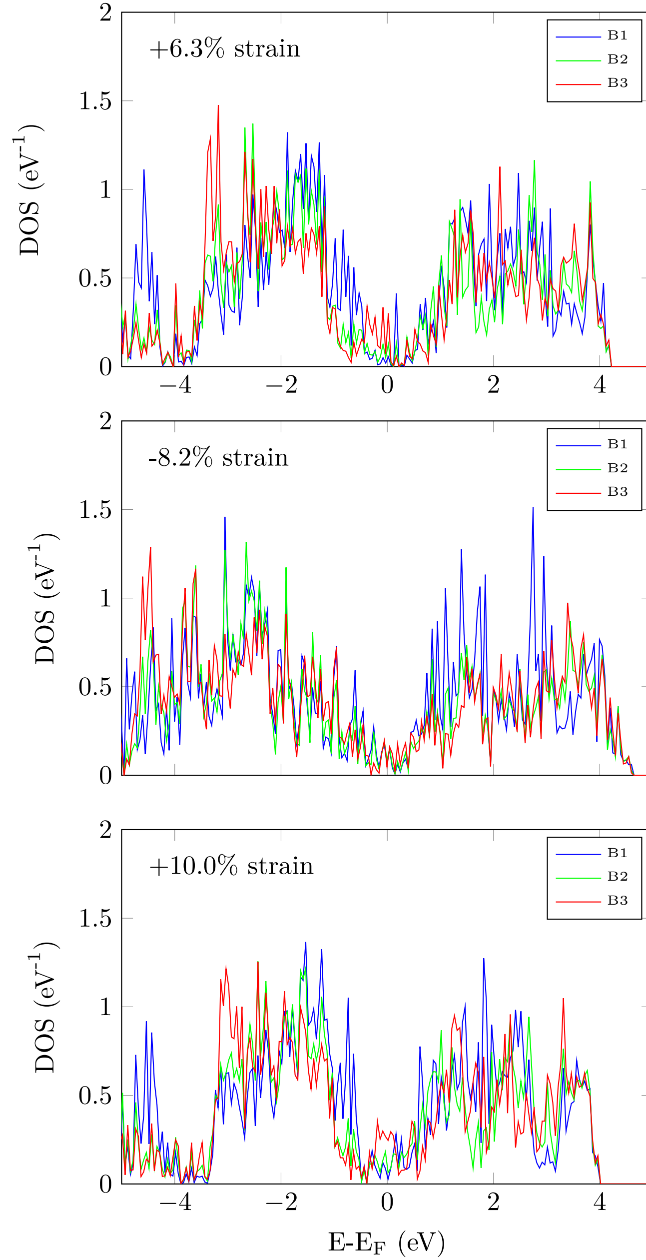

Figure 5.14: *LDOS for three different strain values of the reconstructed GaAs slab. The regions B1, B2 and B3 are specified in Figure 5.9. The three strain values correspond to the three different relative phase orientations considered in the GaAs/graphene heterostructure calculations. +6.3% strain correspond to 0° orientation, -8.2% strain correspond to 30° orientation and +10.0% strain correspond to a 16.1% orientation.*

5.3 GaAs graphene heterostructures

In the following section, the results for all heterostructure calculations are presented. In the first part structural calculations are presented and secondly electronic structure calculations are shown.

5.3.1 Structural calculations

Testing of functionals

Different functionals and potentials are evaluated in order to investigate the effect of and the differences of the respective functional and potential combinations.

Three different relative epitaxial orientations are considered, where the relative phase orientation between graphene and GaAs is 0°, 16.1° and 30° with respect to the in-plane hexagonal symmetry. For the 0° orientation, three translations are considered, for which interface Ga are positioned above Top sites, Hollow sites and Bridge sites on graphene, respectively. In the 16.1° orientation and the 30° orientation the interface Ga atoms are positioned above Bridge sites on graphene. Figure 4.10 visualizes the considered configurations.

Figure 5.15 shows how the supercell energy changes with distance between the GaAs slab and the graphene layers. The energy on the y-axis is the total supercell energy given relative to the minimum energy of each functional/potential calculation, for comparison. These calculations are performed with the PBEsol functional with standard carbon potential as well as with the vdW functional optPBE, with both standard carbon and hard carbon potentials, respectively.

There are significant differences between PBEsol and optPBE for all the epitaxial configurations. For the three configurations within the 0° and for the 30° orientation, a positive interaction for both optPBE and PBEsol is observed. However the calculations on the 16.1° system within the PBEsol functional reveal marginal positive interaction. Still, for the two former orientations, the optPBE functional shows a clear improvement with respect to the observed interaction energy, as these curves have a considerably larger curvature. The difference between using standard and hard potential for carbon within the optPBE functional is marginal for all configurations. Thus, applying hard carbon potential for calculations with optPBE only contributes to a quantitatively slightly higher precision of the calculation, however no significant qualitative changes are observed. The equilibrium distance between GaAs shifts to longer distances for the optPBE functional as compared to the PBEsol for all configurations.

Energy as function of GaAs graphene distance

Energy as function of distance between GaAs and graphene is calculated with a smaller step length (0.04 Å) around the equilibrium distance found from the functional testing, which is seen in Figure 5.15. Because of the different strain for the different orientations, the number of carbon atoms

within each graphene sheet in the supercell varies for the different supercells. For comparison of total supercell energies for the different configurations, n times the chemical potential of carbon in graphite is therefore added to and subtracted from the total supercell energies for the 30° and 16.1°, respectively. n is the difference in the number of carbon atoms between the 0° and the 30° supercells and the 16.1° and the 0° supercells, respectively. Comparing total energies imply that the 30° orientation, where all atoms are positioned on Bridge sites is the most stable one, as this configuration has the lowest energy minimum. The Top configuration for 0° is the second most stable configuration, closely followed by the Bridge configuration for 0°. The Hollow configuration is the least stable translation of the 0° configurations, whereas the 16.1° configuration is the overall least stable configuration. This is also the most heavily strained structure of the ones that have been investigated.

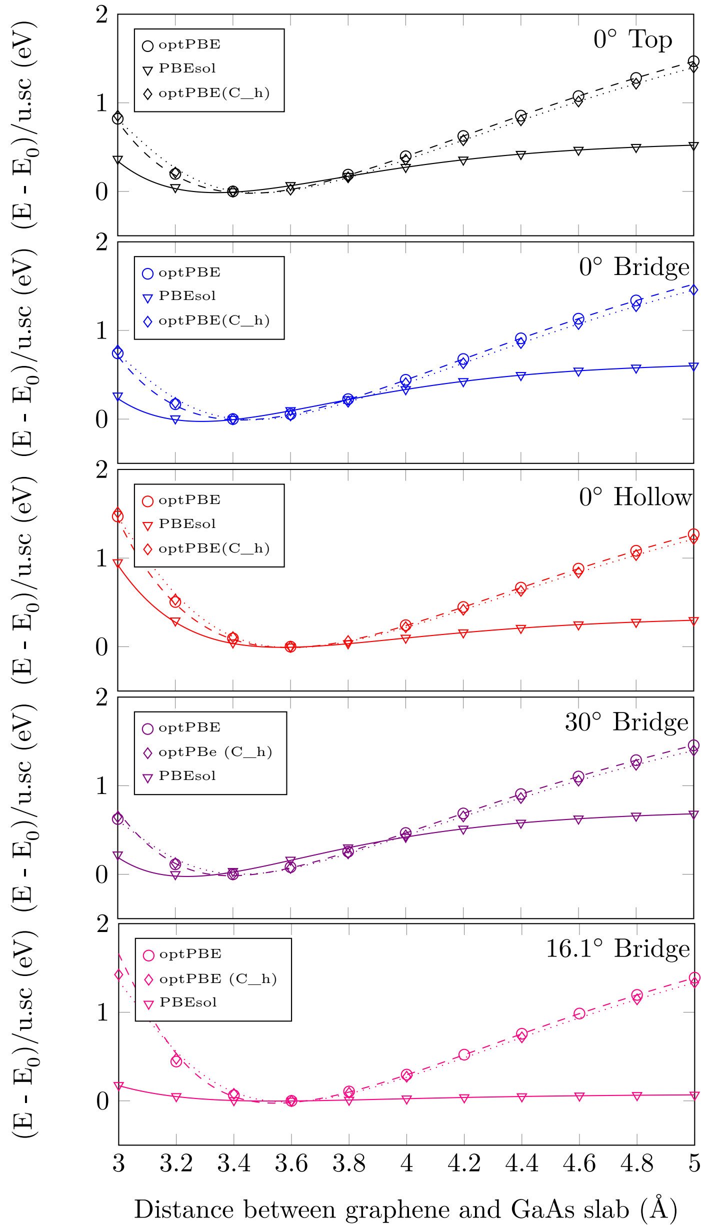

Figure 5.15: *Comparison of energy as function of distance between graphene and GaAs slab in heterostructure supercell for calculations performed the vdW functional optPBE and standard and hard carbon potentials, respectively. The total energy is scaled with the minimum energy value calculated within its potential, in order to compare the relative slopes of standard and hard carbon potential. The lines connecting the data points are fitted spline curves, as a guidance to the eye.*

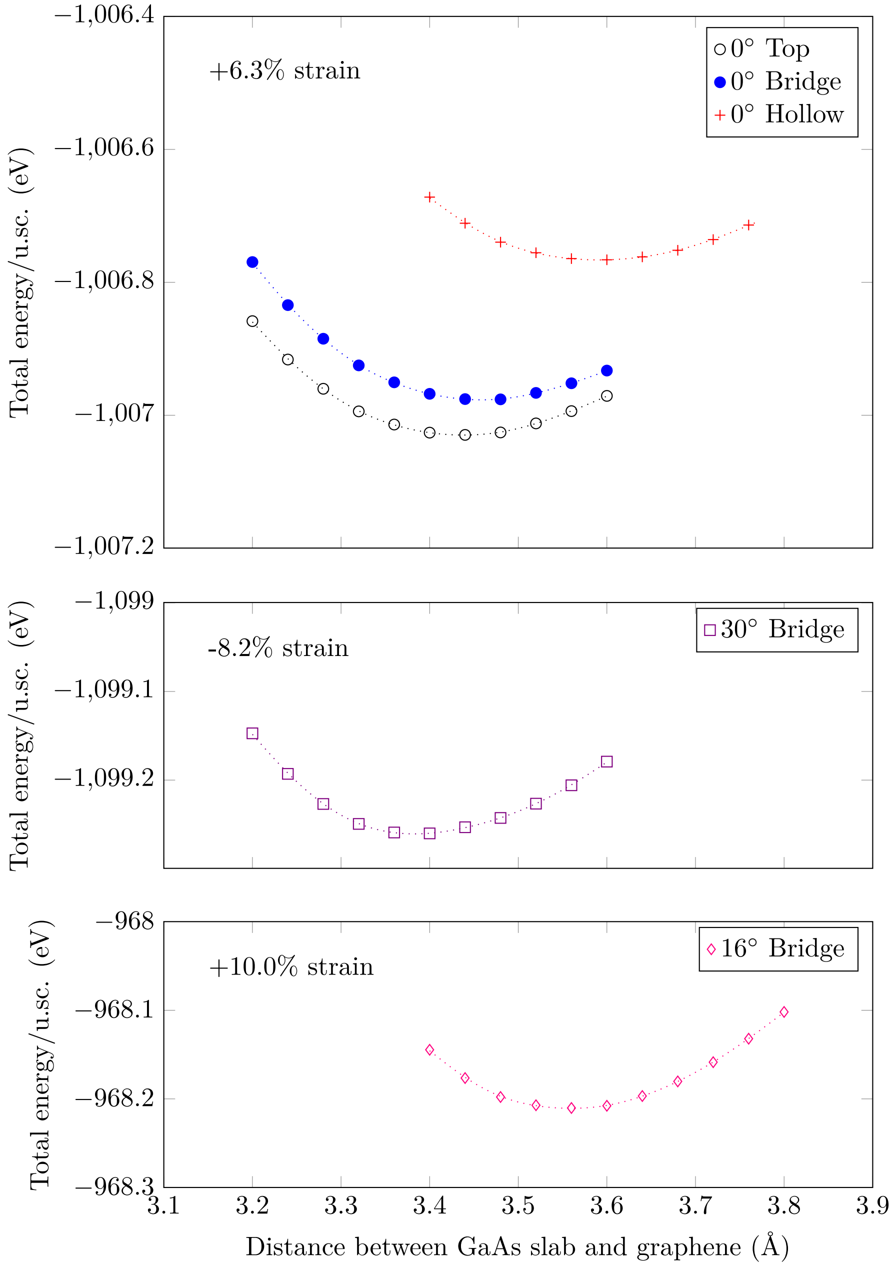

Figure 5.16: *Total energy as function of distance between GaAs and graphene, calculated within optPBE using standard carbon potential. The total energies are given per unit super cell (u.sc). There is an inequivalent number of carbon atoms within each supercell with different orientation, which is a consequence of the different degrees of strain. Therefore, the chemical potential of carbon $P6_3mc$ is added to the total energy of the 30° (-8.2% strain) and subtracted from energy of the 16.1° (10%) orientation the number of times corresponding to the difference in carbon atoms between the 0° and the 30° orientations and the 0° and the 16.1° orientations, respectively. This is done in order to compare total energies of the supercells. The lines connecting the data points are fitted spline curves, as a guidance to the eye.*

Relaxation of interface layers

Following static calculations to determine the equilibrium position between graphene and GaAs, the interface GaAs layer, which during former static calculations has been equal to a GaAs reconstructed surface towards vacuum, is free to relax. All carbon atoms within the graphene layers are also free to relax.

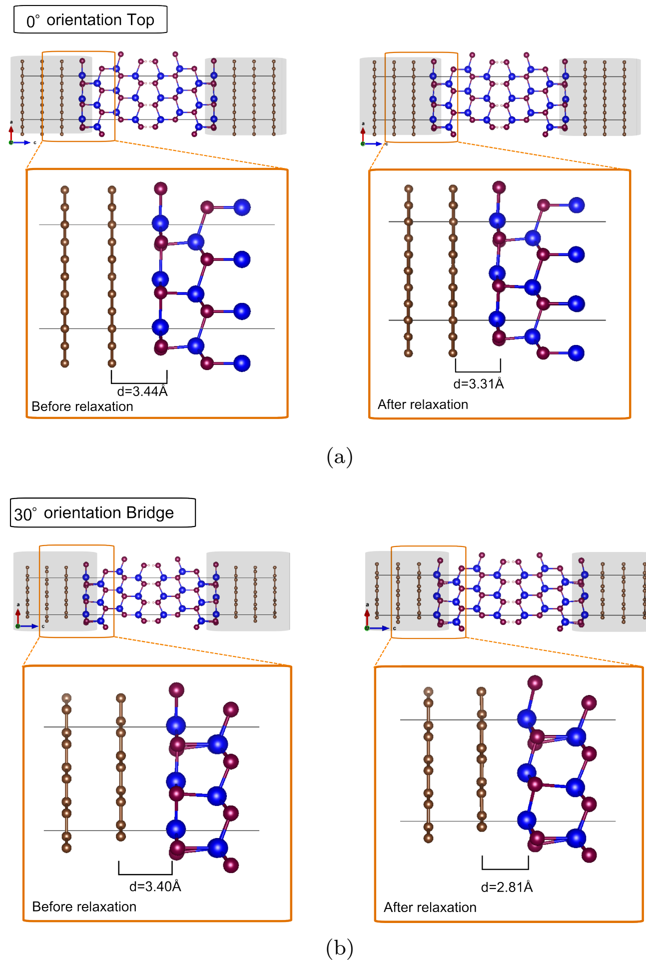

Figure 5.17: *Ionic relaxation at the interface of* (**a**) *the 0° Top and* (**b**) *30° Bridge configuration, respectively. Relaxation is done with selective dynamics. The layers within the shaded areas (the interface GaAs bilayer and the all graphene layers) are free to relax in x, y and z directions, whereas all other atoms are kept fixed.*

The two configurations found to be most stable from the former static calculations are studied, namely the 0° Top configuration and the 30° Bridge configuration. Figure 5.17 shows the interface of 0° Top configuration and 30° Bridge configuration before and after dynamic relaxation. The initial distance

is the equilibrium distance found from static calculations. For both configurations considered, the distance between GaAs and graphene is considerably shortened as compared to what was found in the static calculations. Further, the GaAs surface is more heavily altered in the proximity of graphene for the 30° Bridge configuration than the 0° Top configuration; Ga atoms are pulled outward toward the interface graphene layer.

5.3.2 Electronic structure of 30° interface configuration

Local density of states

The structural calculations point towards that the 30° configuration is the most stable of the different epitaxial configurations that have been investigated within the constructed model. Therefore, a further electronic structure investigation of the 30° configuration is conducted, by studying local density of states (LDOS).

Figure 5.18 shows the different regions considered where local DOS have been studied. The three outermost bilayers of GaAs have been studied, along with the three graphene layers, as depicted in the figure. Figure 5.19 shows the total LDOS for the GaAs layers (upper panel) and the graphene layers (lower panel). Orbital resolved LDOS for different GaAs bilayers are shown in Figure 5.20, and orbital resolved LDOS for the graphene layers are shown in Figure 5.21. There is a charge accumulation at the Fermi level in bilayer 1 which is prominent compared to bilayers 2 and 3. A charge depletion at the Fermi level is seen for the interface graphene layer compared to the two other considered graphene layers. This might imply some charge transfer from the graphene layer to interface GaAs layer, thus an indication of a certain degree of covalence between GaAs and graphene.

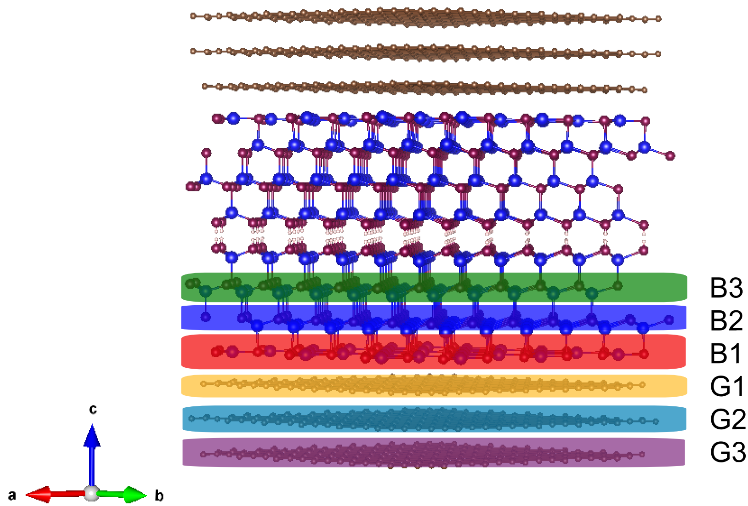

Figure 5.18: *Local DOS (LDOS) regions. B1, B2 and B3 are bilayer 1 (the surface bilayer) bilayer 2 and bilayer 3. G1, G2 and G3 referres to graphene layer 1 (the layer at the interface) and the two layers beneath this, respectively, as illustrated in the figure.*

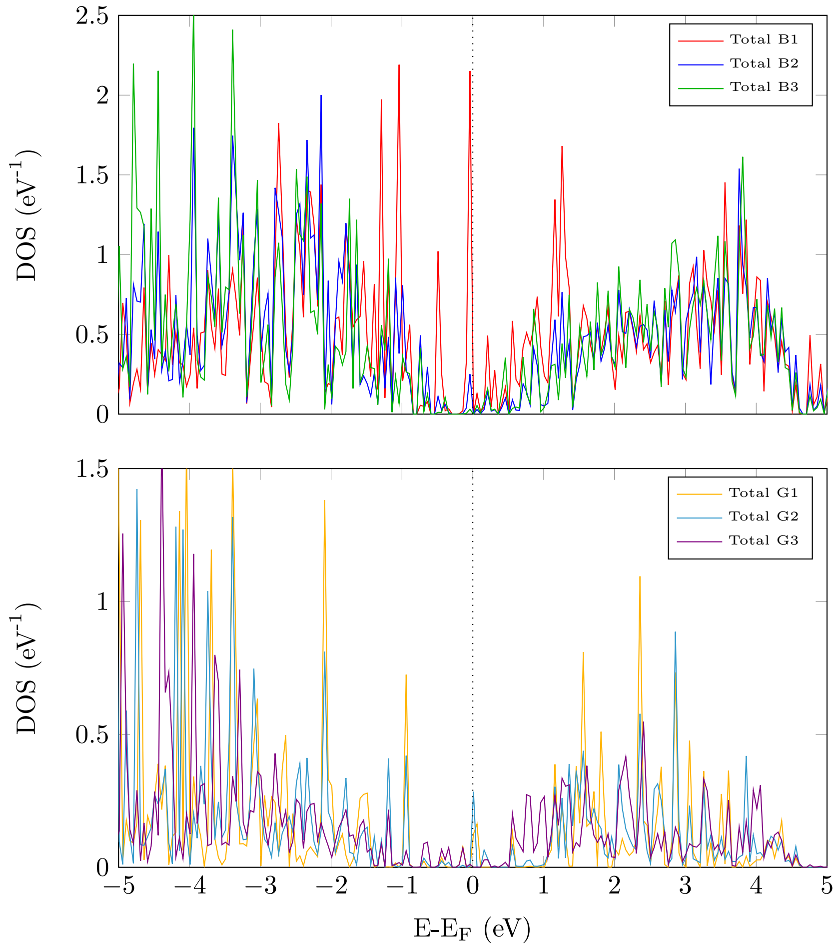

Figure 5.19: *LDOS for the dynamically relaxed heterostructure for the 30° orientation. Upper panel shows the LDOS for the GaAs regions depicted in Figure 5.18. Lower panel shows the LDOS for the three graphene layers depicted in Figure 5.18.*

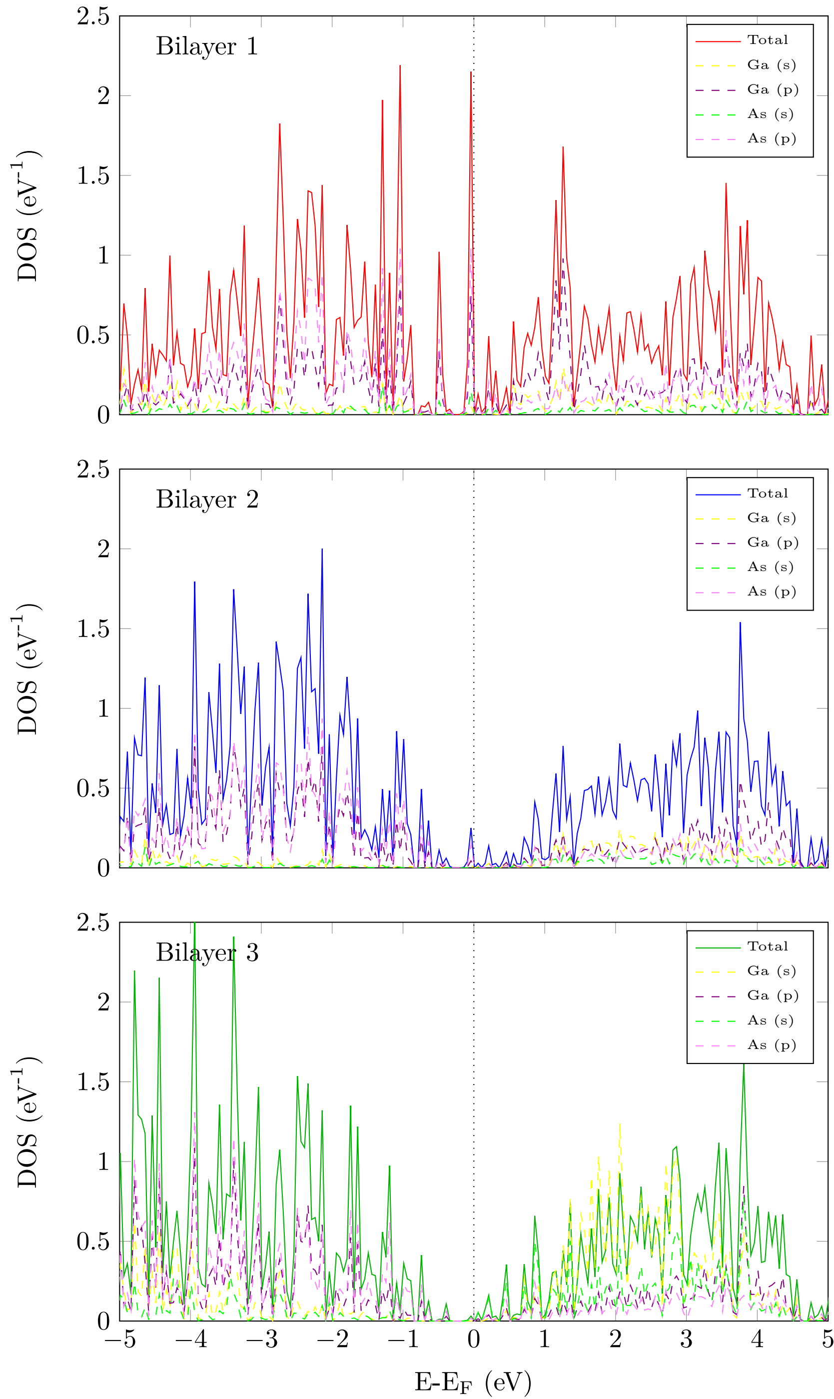

Figure 5.20: *Orbital resolved LDOS for GaAs regions described in Figure 5.18. Upper panel shows the LDOS for the interface layer of GaAs, the mid panel shows the LDOS for the second GaAs bilayer and the lower panel shows the LDOS for the third GaAs bilayer.*

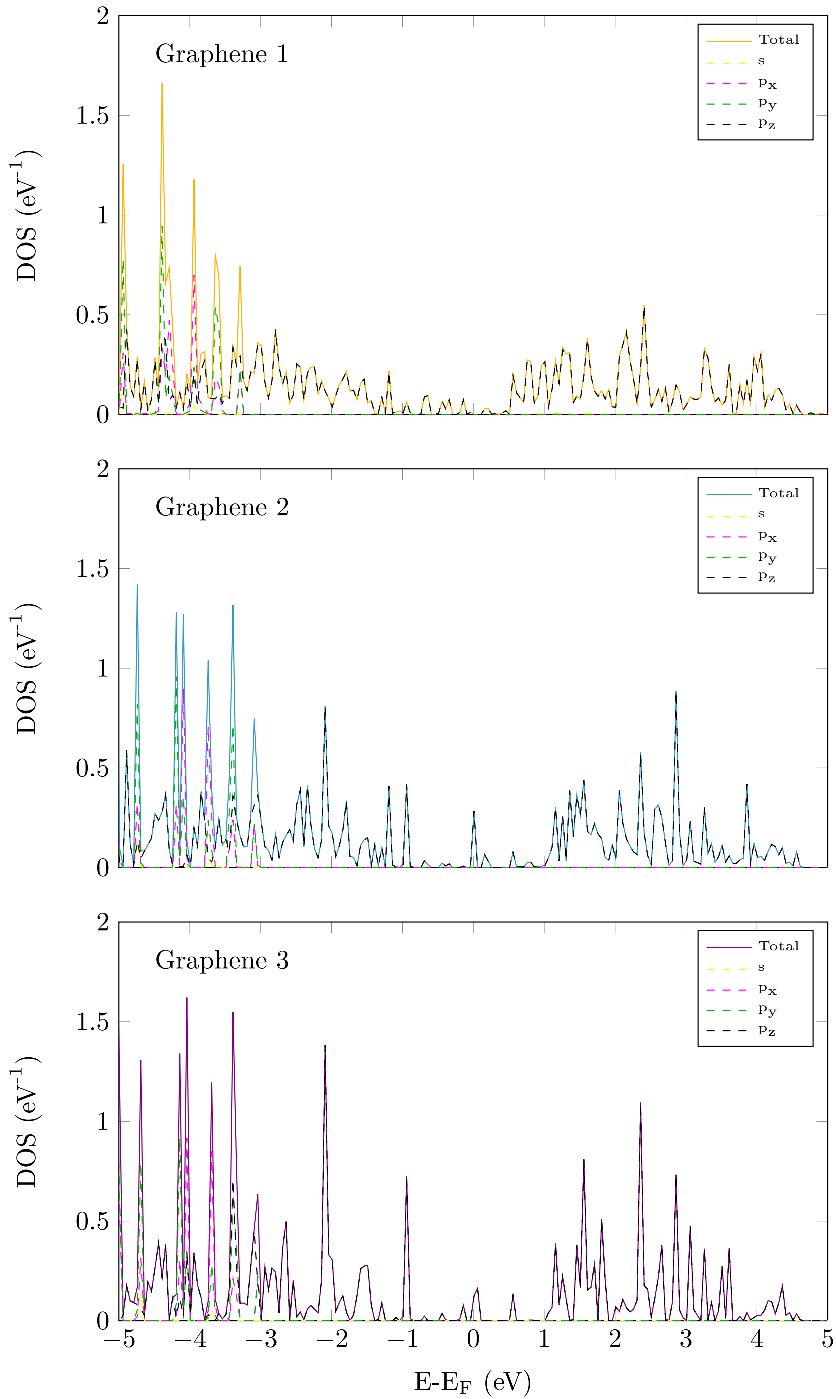

Figure 5.21: *Orbital resolved LDOS for graphene regions described in Figure 5.18. Upper panel shows the LDOS for the interface layer of graphene, the mid panel shows the LDOS for the second graphene layer and the lower panel shows the LDOS for the third graphene layer.*

Chapter 6

Discussion

A computational model has been constructed to study the atomic and electron structure at the interface between GaAs and graphene. The aim has not been to construct a model which is able to capture and reproduce all aspects of the interface, as this is simply not possible within the limits of DFT. The main focus has been to study different epitaxial structures and relative interaction energies. In these regards, methodology has been important in terms of investigating which computational choices must be made to capture the relative interactions at the interface. Electronic structure at the interface has also been studied. However within the present model, investigation of the electronic structure has rather been to gain qualitative insight, more than obtaining precise quantitative information.

6.1 Epitaxial configurations

Five different epitaxial configurations have been studied; three different relative in-plane phase orientations between ZB GaAs(111) and graphene: the 0°, 16.1° and the 30° orientations, where three different translations of the 0° orientation have been considered. These configurations have been chosen inspired by those within the epitaxial model presented by Munshi et al. [1]. However, due to the assumption of having a GaAs(111)-2 $\times$ 2 surface reconstruction with Ga vacancies, the in-plane structure of the interface Ga-atoms do not exhibit perfect hexagonal symmetry since the surface atomic coordinates are slightly shifted as compared to a bulk-terminated surface. The different configurations have different degrees of in-plane (111) strain, in order to accommodate lattice mismatch between GaAs and graphene at the interface. The strain values associated with the different orientations are quite significant: 6.3% tensile strain, 10.0% tensile strain and -8.2% compressive strain for the 0°, 16.1° and the 30°, orientations respectively. In the epitaxial model by Munshi et al. [1] a fourth orientation is proposed, a 10.9° orientation. However, the in-plane GaAs strain associated with this orientation is -22.7%, which is an extreme compression, and physically not very plausible. The in-plane strain

calculations of GaAs reconstructed slab structures, did not render a stable reconstructed surface of the slab at this value of compressive strain and was therefore not considered further in the heterostructure calculations.

6.1.1 The GaAs crystal structure

In the study of the epitaxial interface, only the GaAs ZB structure has been considered. This is the energetically most stable structure in bulk. The study of *ab*-strained GaAs, in the ZB(111) and the WZ(0001) planes, respectively, show, however, that the relative stabilities of these two crystal structures are sensitive to strain (Figure 5.4).

However, in consideration of GaAs *nanowires*, there is the complicating element of size- and dimension-induced new properties. It has been reported that nanowires are successfully grown in both the ZB structure [55], the WZ structure [56] and mixed phases [1]. Johansson et al. [46] have reported that the crystallographic structure in fact can be tuned, by controlling the diameter of III-V semiconductor nanowires. Thus, even though only one crystal structure has been considered within the constructed model in this work, also the WZ structure can be realized.

6.1.2 The effect of strain

The bandgap evolution of *ab*-strained bulk ZB GaAs(111) (5.7) has been studied. According to the present study, the bandgap is highly sensitive to *ab*-plane straining. For sufficiently high strains, the bandgap becomes insignificant and GaAs becomes metallic. Generally, if a semiconductor is put under high compression, this will, for high enough compressions, lead the semiconductor to become metallic. The reason for this is that the orbitals are forced to overlap more and more, which leads the energy bands to broaden until the valence band eventually overlaps with the conduction band. For isotropic expansion of the material, an opposite effect is observed: as atoms are pulled further apart from each other, the orbital overlap decreases, leading to a larger bandgap. However, in this study, bulk GaAs has only been strained in two dimensions. Atomic positions in the direction perpendicular to the strain-plane are able to relax. Thus, in the strain-plane, the overlapping of the orbitals increases and decreases, for compressive and tensile strain, respectively, whereas in the perpendicular direction, a counteracting effect is observed. This counteracting effect might explain the observed bandgap evolution. However, further investigations into electronic effects of strain have not here been conducted, as this was not the main focus of the present work.

The effect of straining GaAs slab structure supercells has been studied, both with reconstructed surfaces and with bulk-terminated surfaces, for comparison. In Figure 6.1 the energy of straining a GaAs slab structure with surface reconstruction is replotted, but with energies scaled with the minimum energy (at zero strain) to better see the energy penalty of straining. The three considered orientations are also marked at their respective strain values. The strain penalty is smallest for the 0° orientation, which has a strain of 6.3% associated with it, and largest for the 16.1° orientation, which has a

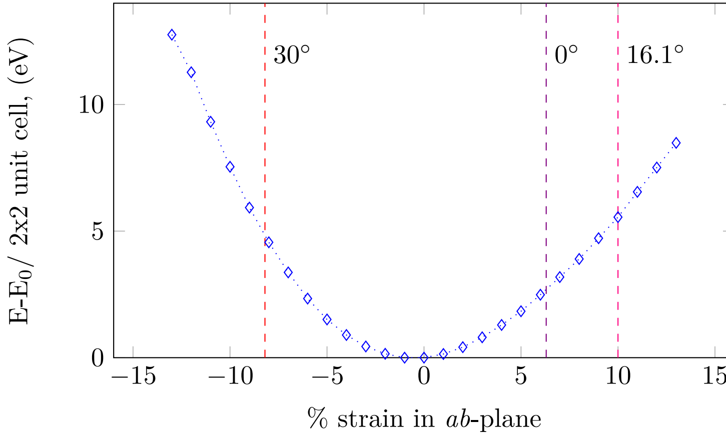

Figure 6.1: *Energy penalty of ab-plane straining per* 2×2 *reconstructed surface. The different strains for the three different orientations considered, are marked with dotted lines.* E_0 *is the energy at zero strain.*

strain of 10% associated with it. The strain penalty per 2×2 unit cell is in the order of many eV, which is a massive energy penalty. However, this is essentially modelling of the strain in thin films because of the periodic boundary conditions in the calculations. Because of the nature of the nanowires, they are in fact able to accommodate much larger lattice mismatches than thin films, thus the quantitative values of the strain penalties found for the different configurations, are artificially high.

As a GaAs(111)-2×2 reconstruction is assumed to take place at the GaAs/graphene interface, the energetic driving force for surface reconstruction as function of strain has been studied, seen in Figure 5.12 in Chapter 5. Of particular interest are the strain values associated with the three different considered orientations, 0°, 16.1° and 30° , respectively. Thus, Figure 5.12 is replotted in Figure 6.2, where these orientations are marked with the respective strains associated with them. The 30° orientation is at a strain value where the reconstruction energy is found to be almost at its maximum value with respect to strain. The 16.1° orientation, however, requires a strain value for which the driving force for reconstruction is significantly reduced with respect to unstrained conditions.

6.2 Energy landscape at the interface

A main focus of the present work has been to establish an insight into the methodology that is necessary for studying the energy landscape at the interface. By this is meant how different configurations (relative phase orientations and translations) vary in energy, and the nature and strength of the GaAs/graphene interaction for the different configurations considered.

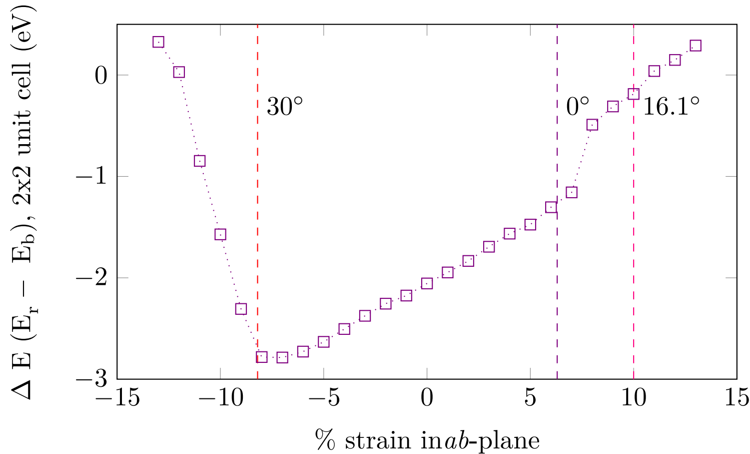

Figure 6.2: *The reconstruction energy per* 2 × 2 *surface unit cell as function of strain in the ab-plane.*

6.2.1 Functional evaluation

In evaluating the interaction energy between GaAs and graphene at the interface, two different functionals have been evaluated, the semi-local PBEsol functional and the vdW functional optPBE. The evaluation of these two functionals revealed that vdW functionals are necessary in order to capture the actual strength of interaction between GaAs and graphene. In fact the semi-local PBEsol functional is not able to capture any significant interaction compared to the optPBE functional. This is an indication that vdW interactions account for most of the interaction between GaAs and graphene. Further, with the optPBE functional, both standard and hard carbon potentials have been evaluated. Hard potentials are more accurate, but require a higher cutoff-energy, and are therefore more computationally costly. Evaluation of the GaAs/graphene interaction energy, however, showed that there is no significant qualitative difference between using standard and hard carbon potentials. Therefore, for computational savings, standard carbon potential was used throughout further heterostructure calculations within the present model.

6.2.2 Estimate of interaction energy

Estimates of the vdW interactions for the different orientations at the interface are made. These estimates are made based on the energy mapping plotted in Figure 5.15.

This is done by plotting the total energies of the respective supercells as function of d^{-6}, where d is the distance between the GaAs slab and graphene. In Figure 6.3 the total energies are scaled with the minimum energy for each configuration. Further, the curves are linearly extrapolated to d^{-6} equal to zero. This is done in order to estimate the total energy as $d \longrightarrow \infty$, since

Table 6.1: *Estimated interaction energies for different configurations along with a calculated reference for interlayer binding energy in graphite $P6_3mc$ and references from experimental data reported in literature.*

Configurations	Interaction energy [J/m^2]
0° Top	0.24
0° Bridge	0.26
0° Hollow	0.23
30° Bridge	0.31
16.1° Bridge	0.24
Graphite	**Interlayer binding energy [J/m^2]**
Calculated	0.21
Experimental	0.19 - 0.32 [57, 58]

this is the limit of no GaAs/graphene interaction. Energy is plotted against d^{-6}, because it scales with the attractive term in the Lennard Jones (LJ) potential. This term in the LJ potential exactly represents van der Waals interactions (see Section 3.3). The interaction energy is estimated by the following equation:

$$E_i = \frac{1}{2}(E - E_0)/A \tag{6.1}$$

where E_i is the estimated vdW interaction energy, E is the total energy of the respective double-slab supercell, E_0 is the minimum energy with respect to GaAs/graphene distance and A is the supercell ab-plane area. The factor $\frac{1}{2}$ accounts for the fact that there are two interfaces in the supercell.

Table 6.1 sums up the interaction energies calculated for the different configurations along with the graphene interlayer binding energy.

The interaction energies are estimated based on the static calculations for which the relative atomic positions at the interface have not been allowed to move. In other words, the atomic coordinates in the GaAs slab are those in the slab with the GaAs(111)-2 × 2 reconstruction terminated towards vacuum. Thus, up to this point atomic coordinates have not been allowed to move in response to interface interactions. As demonstrated through dynamic relaxations considered for two of the configurations, an alteration of the interface structure is indeed observed along with a shortening of the GaAs/grahene distance (Figure 5.17). Thus, the real interaction energies are possibly somewhat higher than the estimated values here. However, the estimates still provide an idea about order of magnitude of the strength of interactions, as well as relative differences between the different configurations.

The different configurations do not differ significantly in energy, however the overall strongest interaction is found for the 30° Bridge configuration. This is also the configuration that during static calculations was found to have the shortest equilibrium distance between GaAs and graphene. Overall, the Bridge configurations interact somewhat more strongly than the respective other configurations. In the project work work [5], adatom adsorption of Ga

and As single atoms onto graphene was studied. It was found the Ga is most stable at a Hollow position and As is most stable in Bridge positions, a result that is supported by Nakada et al. [49]. The present results, however, do not support that Ga at the surface of GaAs is the most stable in a Hollow position.

However, the fact that there are so small changes in the interaction energy between the different configurations reflect that the strength of interaction between GaAs and graphene is weak.

For a reference, the interlayer binding energy for graphite $P6_3mc$ is calculated and plotted in Figure 6.4. The interlayer binding energy is found to be 0.21 J/m^2. Experimental data that has been reported for the interlayer energy span the energy interval of the estimated the GaAs/graphene interaction energies found here, which can be seen in Table 6.1.

The interaction energies are in the same order of magnitude as the graphene interlayer binding energy, and this is in good agreement with what has been established here, that the nature of interaction between GaAs and graphene is dominated by weak van der Waals forces.

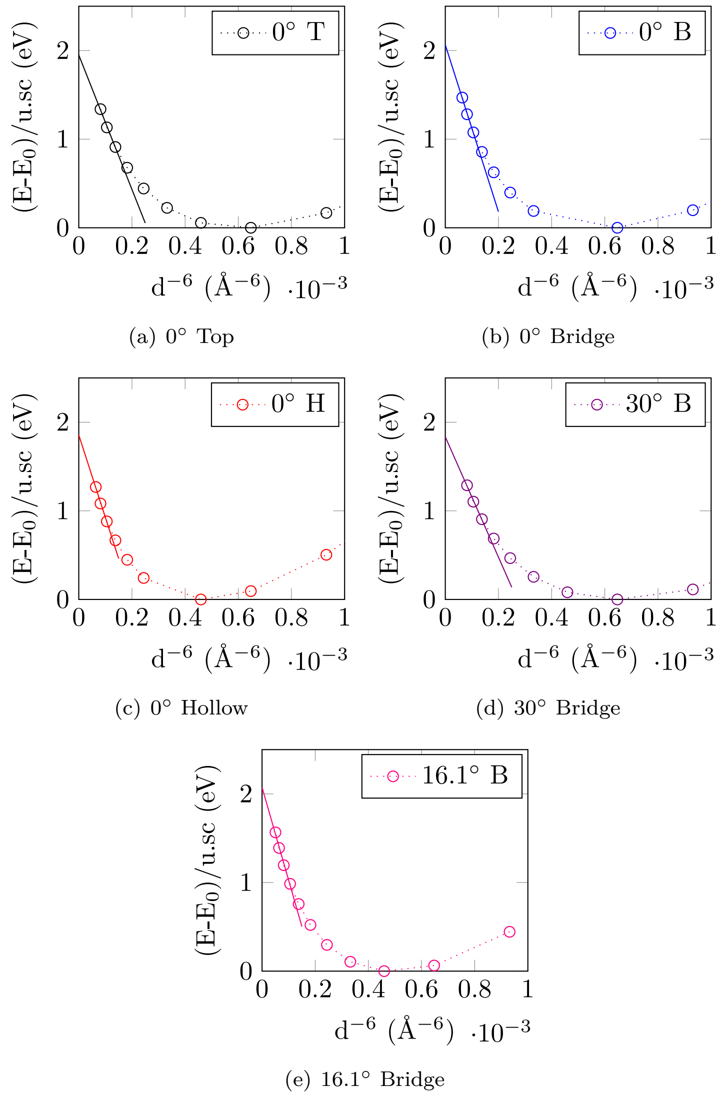

(a) 0° Top

(b) 0° Bridge

(c) 0° Hollow

(d) 30° Bridge

(e) 16.1° Bridge

Figure 6.3: *Estimation of interaction energy between GaAs and graphene for the five different configurations considered. Total energy per unit supercell (u.sc.) is plotted as function of d^{-6}, where d is the distance between graphene and the GaAs slab. The total energy is scaled with the equilibrium distance energy. Estimates are made by linear extrapolation to zero. The linear extrapolations are based on the three data points closest to $d^{-6} = 0$. T, B and H indicate Top, Bridge and Hollow sites, respectively.*

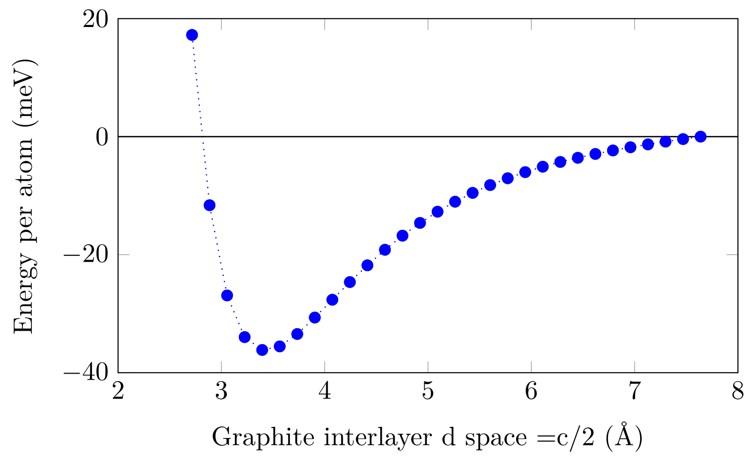

Figure 6.4: *Interlayer binding energy for graphite $P6_3mc$.*

6.3 Structural and electronic considerations

6.3.1 Structural relaxation of the 0° Top and the 30° Bridge configurations

Structural relaxation of the 0° Top configuration and the 30° Bridge configuration has been studied. These were the two most stable ones with respect to total energy, seen in Figure 5.17. These studies showed that the presence of the interface has an effect on the structure of GaAs at the interface. However, the structural effect is significantly stronger for the 30° Bridge configuration than the 0° Top configuration. Again, compared to studies of adatom interactions with graphene, somewhat conflicting results are found here. According to the project work [5] and the results of Nakada et al. [49] in the study of single adatom interaction with graphene, As has an equilibrium distance closer to graphene than Ga, thus indicating stronger interaction. However, as is seen in the dynamic relaxation of the 30° orientation, where atomic coordinates in the GaAs interface is structurally relaxed in all three directions, the Ga atoms seem to interact more strongly as these are the ones that pull out towards graphene (Figure 5.17). However, study of the interaction of single atoms with graphene is a very simplified scenario, and thus it is perhaps not surprising that one might find conflicting observations in studies of more structurally complicated materials.

6.3.2 Electronic structure of the 30° Bridge configuration

Based on the calculated Local DOS for the 30° orientation (Figure 5.20), GaAs is seen to be metallic, exhibiting no bandgap around the Fermi level. Also, the LDOSes for GaAs differ considerably from the LDOSes found for the GaAs reconstructed slab with no graphene present. Yelgel et al. have done an *ab initio* study of the InAs(111)/graphene interface using DFT [15]. InAs and GaAs are highly similar materials. They report that the InAs at the InAs/graphene interface also exhibits metallic character at the interface, and they strongly and exclusively attribute this shift from semiconducting to metallic character to the interaction of InAs with graphene. The lattice mismatch for the configurations considered in the study of Yelgel et al. was 0.16%.

In the present work, however, it is found that the GaAs bandgap is also heavily altered by biaxial strain, and for the interfaces considered, the strain itself has reduced the bandgap of GaAs considerably.

Electron localization function

As a continued effort to investigate electronic structure, the electron localization function for the 30° structure has been studied. The higher value of the isosurface level, the more localized are the electrons included in the visualization.

Figure 6.5 shows the electron localization function for three different graphene layers in the supercell, and for each layer three different isosurface

levels (ISL) are visualized. For the highest isosurface level the strong in-plane σ-bonds are observed. For the lower isosurface levels, delocalized π bonds around each hexagon are seen. There is no significant difference in the electron localization functions for the three layers, except for the uppermost layer for the lowest ISL, where interaction sites with GaAs are seen. The hexagonal pattern of blue dots can be recognized, which indicates the sites of Ga at the interface. Also, the interaction sites are not strictly on bridge sites, however, they are positioned partly on bridge sites and partly on Top sites.

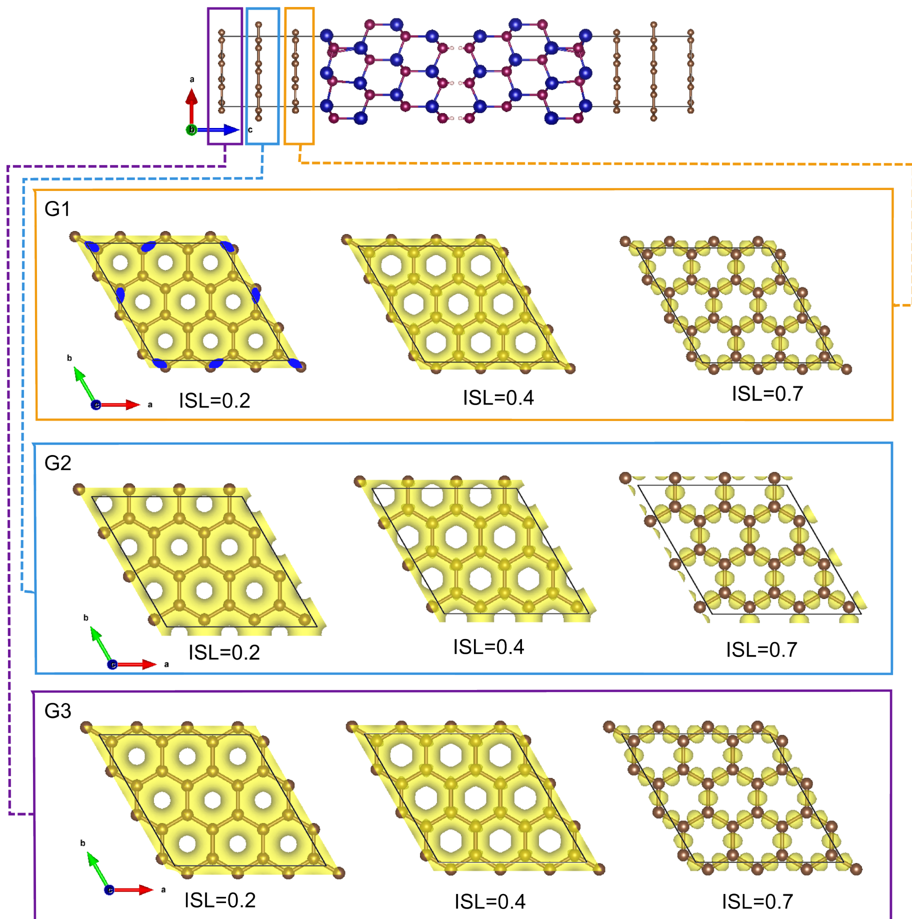

Figure 6.5: *Electron localization function for three different graphene sheets in the 30 ° heterostructrue supercell. For each layer, three different isosurface levels are visualized.*

In Figure 6.6 the electron localization function around the interface along the supercell b-direction is shown. At the highest visualized ISL the chemical bonds (the sp^2 orbitals) in graphene are seen along with the chemical bonds in GaAs around the interface. At this level, no interaction can be observed between GaAs and graphene. However, at an ISL of 0.2, interaction is indeed

observed, although fairly weak.

Figure 6.7 shows the electron localization function for three different isosurface levels for the three outermost GaAs layers in the relaxed 30° structure. For the interface layer the charge is highly concentrated on the As atoms around the Ga vacancy. Although, atomic coordinates of the reconstructed GaAs surface have changed in response to the presence of the interface, the projected *ab*-plane symmetry is barely seen altered from the GaAs(111)-2 $\times$ 2 reconstructed surface terminated towards vacuum.

The two upper bilayers (B2 and B3) differ significantly from the interface layer, which is what one should expect. For the highest ISL for the uppermost bilayers, the tetrahedral coordination characteristic for sp^3-bonds are clearly seen.

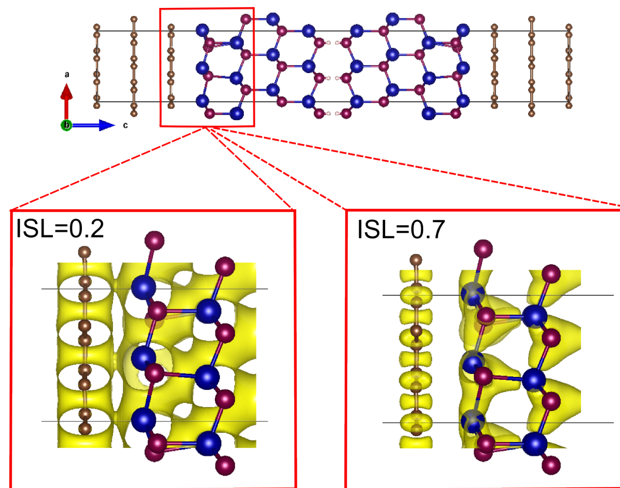

Figure 6.6: *Electron localization function shown at the interface between graphene and GaAs in the dynamically relaxed 30° supercell, for different isosurface levels (ISL).*

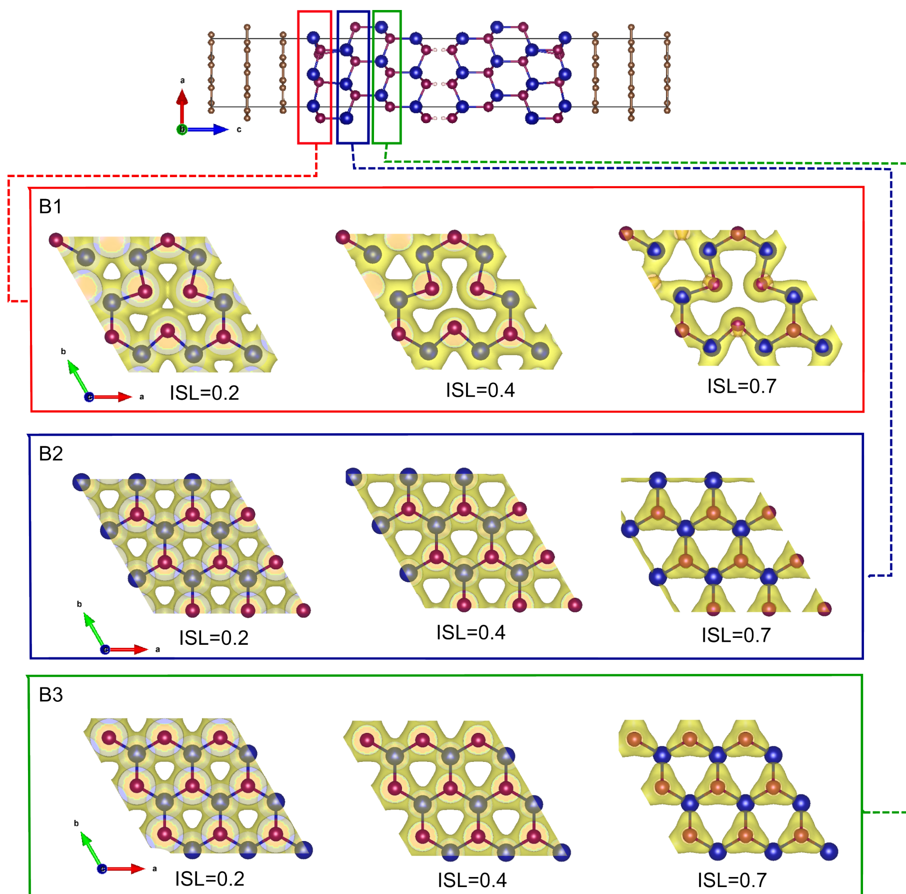

Figure 6.7: *Electron localization function visualized for different regions of the dynamically relaxed 30° Bridge cell for different isosurface levels (ISL).*

6.4 The Computational Model

The development of a computational model to study different epitaxial interfaces between GaAs and graphene is not straight forward. In the present work, a model has been constructed on the assumption that the GaAs(111) surface at the interface under study is 2×2 reconstructed with the presence of Ga vacancies. A reconstruction of the GaAs surface is assumed based on the both computationally and experimentally very strong driving force for reconstruction at the GaAs(111) surface due to the energetically highly unstable dangling bonds at the interface. There have been reported several reconstructions of the GaAs(111) surface. However, as a 2×2 reconstruction is the most simple one, this is a natural starting point, and has been the only considered reconstruction in this work. In the present work, the reconstruction energy for the unstrained GaAs(111)-2×2 surface was found to be 2.33 eV/ 2×2 unit cell. This is in good accordance with the calculated value reported by Chadi et al. [59], of 2.3 eV/2×2 unit cell.

The aim of this model is to provide knowledge about structural and electronic properties at the interface between GaAs and graphene. In fact, the main aim is to predict the properties at the interface between GaAs nanowires and graphene, on which the nanowires are grown. However, providing such a model within the framework of DFT is challenging, and one should be aware of the limitations. The advantage of growing GaAs nanowires as compared to thin films is not reflected very well within this model, with respect to the energy penalty of straining GaAs. This has to do with the fact that nanowires are able to accommodate a much larger lattice mismatch than thin films at the interface because they have the ability to relax in the *ab*-plane in the nanowires as one moves further away from the interface. Thus, there will be an *ab*-plane strain gradient in the growth direction of the nanowire. This feature is not captured by the simple slab model and the strain calculations performed in the present work. Thus, calculations evaluating the effect of strain are likely to overestimate the energy penalty for the nanowires at the interface.

The estimated vdW interaction energy is a rough estimate, and merely meant for relative comparison of the interaction energy for the different configurations, rather than a precise interaction quantification. Ideally, in estimating the interaction energy, the GaAs/graphene gap within the supercells should be successively increased until the two phases are no longer interacting. However, due to the fact that vdW functionals converge increasingly slowly with more vacuum in the cell, such an approach would be extremely computationally demanding and ineffective.

6.4.1 Choice of functionals

The choices made with respect to functionals throughout the present project have been made with the focus on studying atomic structures and relative energies at the interface of GaAs. In the consideration of electronic structure, and in particular calculations of the bandgap, it is a known limitation within

DFT that the conventional functionals underestimates this property. vdW functionals are neither optimized to improve this fact. In order to calculate more accurate bandap values, hybrid functionals should be used. However, in the present work, accurate quantification of electronic structure has not been the aim, but rather gaining a qualitative understanding of what affects the properties at the interface and trends in the evolution of properties with respect to change of different parameters.

6.5 Further work

Throughout the present work it has become evident that investigations of the structural and electronic properties at the GaAs/graphene interface, and thus also similar interfaces, is a demanding task. The model constructed in this work has its limitations with respect to providing quantitatively reliable information about electron structure. Also, many assumptions that are implemented in the model, need to be further validated. For example, only the GaAs ZB structure has been considered at the interface. For further structural considerations, the WZ structure should also be considered. As the GaAs(111) surface has been reported to have more than one reconstruction, this is also an aspect that could be further investigated.

In order to gain a more realistic image on how nanowires respond to in-plane straining, classical molecular dynamics (MD) could be used. With an MD approach, nanowires could be studied as a whole, because this method is computationally much less demanding than DFT. However, it would not provide any information about electronic structure. In order to capture all aspects of the interface under study, a multiscale modelling approach is indeed necessary.

Chapter 7

Conclusion

Epitaxial interfaces between GaAs(111) and graphene have been studied with a first-principles approach, using density functional theory. Three in-plane relative phase orientations 0°, 16.1° and 30°, and three different translations of the 0° orientation have been studied. In the three translations, all interface Ga atoms are positioned either right above a carbon atom (Top sites), above a C-C bond (Bridge sites) or right above the center of a carbon hexagon (Hollow sites). In the 16.1° orientation and the 30° orientation, all interface Ga atoms are positioned on Bridge sites.

Within the epitaxial configurations considered, graphene is assumed to be unstrained, whereas the GaAs phase is biaxially strained in the (111) plane to accommodate lattice mismatch. The three phase orientations correspond to a lattice mismatch of +6.3%, +10% and -8.2%, for the 0°, 16.1° and 30°, respectively. The GaAs(111) surface is assumed to be 2×2 reconstructed with Ga vacancies.

Biaxial straining of bulk GaAs, both in the ZB phase (in the (111) plane) and the meta-stable WZ phase (in the 0001 plane) has been studied, to better understand the impact of strain at the GaAs/graphene interface. Straining influences the relative stabilities of the two phases. A study of the bandgap evolution of GaAs ZB as function of biaxial strain, indicates that this property also is highly sensitive to strain.

The GaAs(111)-2×2 reconstructed surface without the presence of graphene has been studied. A mirror-symmetric GaAs double slab has been constructed in order to model surface reconstruction. Biaxial straining of the surface plane has a significant impact on the reconstruction energy. Straining also influences the electronic structure of the surface; the GaAs surface and the adjacent layers become metallic, rendering no bandgap.

The heterostructure interface has been studied by a stepwise structural investigation followed by an investigation of the electronic properties. The interactions between GaAs and graphene at the interface have been studied by two different exchange-correlation functionals: The semi-local GGA functional PBEsol, and the van der Waals (vdW) functional optPBE. This is done by a static energy mapping where the distance between the two phases is

varied. The optPBE functional yields a significantly stronger interaction energy than the PBEsol functional. signifying a substantial vdW contribution to the interactions at the GaAs/graphene interface. The optPBE functional is necessary in order to study dispersion interactions.

The vdW interaction was estimated for each of the five configurations. The interaction energy is found to span from 0.24-0.31 J/m^2, where the 30° configuration is found most strongly interacting. However there are very small differences between the configurations considered. All the estimated interaction energies are in the same order of magnitude as the interlayer binding energy of graphene, which is found to be 0.21 J/m^2.

The present findings show that interactions at the interface between GaAs and graphene are weak, and in terms of growth of GaAs nanowires on graphene, the estimates of the interaction energies indicate that neither of the epitaxial configurations considered are strongly favoured.

Bibliography

[1] A. M. Munshi, D. L. Dheeraj, V. T. Fauske, D.C. Kim, A. T. J. van Helvoort, B.-O. Fimland, and H Weman. Vertically Aligned GaAs Nanowires on Graphite and Few-Layer Graphene: Generic Model and Epitaxial Growth. *Nano Let.*, 12(9):4570–4576, 2012.

[2] C. Neto, F. Guinea, N. M. R. Peres, K. S. Novoselov, and A. K. Geim. The electronic properties of graphene. *Rev. Mod. Phys.*, 81:109–162, 2009.

[3] A. K. Geim. The rise of graphene. *Nat. Mater.*, 6:1476–1122, 2007.

[4] S. Y. Tong, G. Xu, W. Y. Hu, and M. W. Puga. Vacancy buckling model for the (111) surface of III-V compound semiconductors. *J. Vac. Sci. Technol. B.*, 3(4):1076–1078, 1985.

[5] A. Marthinsen. DFT calculations on semiconductor/graphene interfaces. 2013.

[6] W. F. Brinkman, D.E. Haggan, and W.W Troutman. A History of the Invention of the Transistor and Where It Will Lead Us. *J. Solid-State Circuits*, 32:1858–1865, 1997.

[7] J. A. del Alamo. Nanometre-scale electronics with III-V compound semiconductors. *Nature*, 479:317323, 2011.

[8] S.A Dayeh, D. Aplin, X. Zhou, P. Yu, E. T Yu, and D. Wang. High Electron Mobility InAs Nanowire Field-Effect Transistors. *Small*, 3: 326–332, 2007.

[9] X. Duan, Y. Huang, Y. Cui, J. Wang, and C. M. Lieber. Indium phosphide nanowires as building blocks for nanoscale electronic and optoelectronic devices. *Nature*, 409:66–69, 2001.

[10] P. Yang. Semiconductor nanowire building blocks: From flux line pinning to artificial photosynthesis. *MRS Bull.*, 37:806–813, 2012.

[11] T. J. Kempa, R. W. Day, D.C. Kim, H.G. Park, and C.M. Lieber. Semiconductor nanowires: a platform for exploring limits and concepts for nano-enabled solar cells. *Energy Environ. Sci.*, 6:719–733, 2013.

[12] W. Lu and C Lieber. Semiconductor nanowires. *J. Phys. D: Appl. Phys.*, 39(21):R387, 2006.

[13] C. Wilhelm, A. Larrue, X. Dai, D. Migas, and C. Soci. Anisotropic photonic properties of III–V nanowires in the zinc-blende and wurtzite phase. *Nanoscale*, 4:1446–1454, 2012.

[14] K. S. Novoselov, A. K. Geim, S. V. Morozov, D. Jiang, Y. Zhang, S. V. Dubonos, I. V. Grigorieva, and A. A. Firsov. Electric Field Effect in Atomically Thin Carbon Films. *Science*, 306:666–669, 2004.

[15] C. Yelgel, G. P. Srivastava, and R. H. Miwa. Ab initio investigation of the electronic properties of graphene on InAs(111)A. *J. Phys. : Cond. Mater*, 24(48):485004, 2012.

[16] Y. J. Hong, J. W. Yang, W. H. Lee, R. S. Ruoff, K. S. Kim, and T. Fukui. Van der Waals Epitaxial Double Heterostructure: InAs/Single-Layer Graphene/InAs. *Adv. Mater.*, pages 6847–6853, 2013.

[17] D. K. Biegelsen, R. D. Bringans, J. E. Northrup, and L.E. Swartz. Reconstructions of GaAs(111) surfaces observed by scanning tunneling microscopy. *Phys. Rev. Lett.*, 65:452–455, 1990.

[18] D. S. Sholl and J. A. Steckel. *Density functional theory - A practical introduction.* Wiley, 2009.

[19] Zoe H. Barber, editor. *Introduction to Materials Modeling.* Maney, 2005.

[20] G. Kresse and J. Hafner. Ab initio molecular dynamics for liquid metals. *Phys. Rev. B*, 47:558, 1993.

[21] G. Kresse and J. Hafner. Ab initio molecular-dynamics simulation of the liquid-metal-amorphous-semiconductor transition in germanium. *Phys. Rev. B*, 49:14251, 1994.

[22] G. Kresse and J. Furthmuller. Efficiency of ab-initio total energy calculations for metals and semiconductors using a plane-wave basis set. *Comput. Mat. Sci.*, 6:15, 1996.

[23] G. Kresse and J. Furthmuller. Efficient iterative schemes for ab initio total-energy calculations using a plane-wave basis set. *Phys. Rev. B*, 54: 11169, 1996.

[24] M. Born and R. Oppenheimer. Zur Quantentheorie der Molekeln. *Annalen der Physik*, 389(20):457–484, 1927.

[25] P. Hohenberg and W. Kohn. Inhomogeneous Electron Gas. *Phys. Rev.*, 136:B864–B871, 1964.

[26] W. Kohn and L. J. Sham. Self-Consistent Equations Including Exchange and Correlation Effects. *Phys. Rev.*, 140:A1133–A1138, 1965.

[27] L. Hedin and B. I. Lundqvist. Explicit local exchange-correlation potentials. *J. Phys. C.*, 4(14):2064, 1971.

[28] J.P. Perdew, J.A. Chevary, S.H. Vosko, K.A. Jackson, M.R. Pederson, D.J. Singh, and C. Fiolhais. Atoms, Molecules, Solids, and Surfaces: Applications of the Generalized Gradient Approximation for Exchange and Correlation. *Phys. Rev. B*, 46:6671, 1992.

[29] J.P. Perdew, J.A. Chevary, S.H. Vosko, K.A. Jackson, M.R. Pederson, D.J. Singh, and C. Fiolhais. Erratum: Atoms, Molecules, Solids, and Surfaces: Applications of the Generalized Gradient Approximation for Exchange and Correlation. *Phys. Rev. B*, 48:4978, 1993.

[30] J. P. Perdew, K. Burke, and M. Ernzerhof. Generalized Gradient Approximation Made Simple. *Phys. Rev. Lett.*, 77:3865, 1996.

[31] J. P. Perdew, K. Burke, and M. Ernzerhof. Erratum: Generalized Gradient Approximation Made Simple. *Phys. Rev. Lett.*, 78:1396, 1997.

[32] H. Hellmann. Einfuhrung in die Quantumchemie. *Deuticke*, 1937.

[33] R. P. Feynman. Forces in molecules. *Phys. Rev.*, 56:340–343, 1939.

[34] C. Kittel. *Introduction to solid state physics.* Wiley, 2005.

[35] J. Klimes, D.R. Bowler, and A. Michaelides. Van der Waals density functionals applied to solids. *Phys. Rev. B*, 83:195131, 2011.

[36] M. Dion, H. Rydberg, E. Schröder, D. C. Langreth, and B. I. Lundqvist. Van der Waals Density Functional for General Geometries. *Phys. Rev. Lett.*, 92:246401, 2004.

[37] Y. Zhang and W. Yang. Comment on "Generalized Gradient Approximation Made Simple". *Phys. Rev. Lett.*, 80:890–890, 1998.

[38] J. Klimes, D. Bowler, and A. Michaelides. Chemical accuracy for the van der Waals density functional. *J. Phys.: Condens. Matter*, 22(2):022201, 2010.

[39] M. S. Fuhrer, C. N. Lau, and A. H. MacDonald. Graphene: materially better carbon. *MRS bull.*, 35:289–295, 2010.

[40] P. Avouris. Graphene: Electronic and Photonic Properties and Devices. *Nano Let.*, 10(11):4285–4294, 2010.

[41] E.A. Kim and C. Neto. Graphene as an electronic membrane. *EPL (Europhysics Letters)*, 84(5):57007, 2008.

[42] M. Grundmann. *The Physics of Semiconductors - An introduction Including Devices and Nanophysics.* Springer, 2006.

[43] V. Schmidt, J. V. Wittemann, S. Senz, and U. Gösele. Silicon Nanowires: A Review on Aspects of their Growth and their Electrical Properties. *Adv. Mater.*, 21(25-26):2681–2702, 2009.

[44] J. Bao, D. C. Bell, F. Capasso, N. Erdman, D. Wei, L. Fröberg, T. Mårtensson, and L. Samuelson. Nanowire-Induced Wurtzite InAs Thin Film on Zinc-Blende InAs Substrate. *Adv. Mater.*, 21(36):3654–3658, 2009. ISSN 1521-4095.

[45] J. Johansson, L. S. Karlsson, C. P. T. Svensson, T. Mårtensson, B. A. Wacaser, K. Deppert, L. Samuelson, and W. Seifert. Structural properties of [111]B -oriented III-V nanowires. *Nat. Mater.*, 5:574–580, 2006.

[46] J. Johansson, K. A. Dick, P. Caroff, M. E. Messing, J. Bolinsson, K. Deppert, and L. Samuelson. Diameter Dependence of the Wurtzite-Zinc Blende Transition in InAs Nanowires. *J. Phys. Chem. C*, 114(9):3837–3842, 2010.

[47] C. Dupas, P. Houdy, and M. Lahmani, editors. *Nanoscience - Nanotechnologies and Nanophysics.* Springer Berlin Heidelberg, 2007.

[48] E. Kaxiras, Y. Bar-Yam, J. D. Joannopoulos, and K. C. Pandey. Variable stoichiometry surface reconstructions: New models for GaAs($\bar{1}\bar{1}\bar{1}$)(2x2) and ($\sqrt{19}x\sqrt{19}$). *Phys. Rev. Lett.*, 57:106–109, 1986.

[49] K. Nakada and A. Ishii. DFT Calculation for Adatom Adsorption on graphene. *Solid State Commun.*, 151:13–16, 2011.

[50] G. Kresse and D. Joubert. From ultrasoft pseudopotentials to the projector augmented-wave method. *Phys. Rev. B*, 59:1758, 1999.

[51] J Perdew, A. Ruzsinszky, G. I Csonka, O.A. Vydrov, G. E. Scuseria, L. A. Constantin, X. Zhou, and K. Burke. Restoring the density-gradient expansion for exchange in solids and surfaces. *Phys. Rev. Lett.*, 100: 136406, 2008.

[52] E. Kaxiras, Y. Bar-Yam, J. D. Joannopoulos, and K. C. Pandey. Ab initio theory of polar semiconductor surfaces. I. Methodology and the (2x2) reconstructions of GaAs(111). *Phys. Rev. B*, 35:9625–9635, 1987.

[53] O. Madelung, editor. *Semiconductors - Basic Data 2nd ed.* Springer, Berlin, 1996.

[54] M. Methfessel and A. T. Paxton. High-precision sampling for Brillouin-zone integration in metals. *Phys. Rev. B*, 40:3616–3621, 1989.

[55] H. Shtrikman, R. Popovitz-Biro, A. Kretinin, and M. Heiblum. Stacking-Faults-Free Zinc Blende GaAs Nanowires. *Nano Lett.*, 9(1):215–219, 2009.

[56] H. Shtrikman, R. Popovitz-Biro, A. Kretinin, L. Houben, and M. Heiblum. Method for Suppression of Stacking Faults in Wurtzite III-V Nanowires. *Nano Lett.*, 9(4):1506–1510, 2009.

[57] Z. Liu, Jefferson Z. Liu, Y. Cheng, Z. Li, L. Wang, and Q. Zheng. Interlayer binding energy of graphite: A mesoscopic determination from deformation. *Phys. Rev. B*, 85:205418, 2012.

[58] R. Zacharia, H. Ulbricht, and T. Hertel. Interlayer cohesive energy of graphite from thermal desorption of polyaromatic hydrocarbons. *Phys. Rev. B*, 69:155406, 2004.

[59] D. J. Chadi. Vacancy-Induced 2x2 Reconstruction of the Ga(111) Surface of GaAs. *Phys. Rev. Lett.*, 52:1911–1914, 1984.

Chapter A

VASP

In this appendix the general technical aspects of running calculations with VASP are described. Details regarding the VASP files hereunder described are found in the online VASP manual [1].

A.1 The Four Main Input Files

For every simulation to be run VASP requires four main input files:

- INCAR
- POSCAR
- POTCAR
- KPOINTS

INCAR

The INCAR file contains a series of input parameters that decides how a calculation should be performed and which output files that are written. There are a series of tags that can be set in the INCAR file; the example file below shows some of the most important and general ones.

[1] http://cms.mpi.univie.ac.at/vasp/vasp/Contents.html

Listing A.1: INCAR file

```
# general
SYSTEM = GaAs supercell
ISTART = 0
ICHARG = 2
INIWAV = 1
ISMEAR = 0
SIGMA = 0.01
EDIFF = 1.0e-08
EDIFFG = -0.001
PREC = N
LREAL = AUTO

ENCUT = 400

NELM = 60
NELMIN = 2

ISIF = 3
IBRION = 2
NSW = 0
NPAR = 4
```

- ISTART Determines whether the initial wave functions should be set by a WAVECAR file or specified by the tag INIWAV. The WAVECAR is a VASP file can be calculated and contains information about the wavefunctions for the system.
- ISCHARG Determines how the initial charge density is constructed.
- INIWAV Determines how initial wave functions are set up. This tag is only set for start jobs, and not if the ISTART tag is set to read WAVECAR.
- ISMEAR Determines the setting for the partial ocupancies of the wavefunctions.
- SIGMA Determines the smearing width in eV.
- EDIFF The self-consistent field (SCF) energy, which is the electronic convergence criterion.
- EDIFFG Determines the ionic convergence criterion. A positive EDIFFG implies that calculations stop when the supercell energy has reached a value below this criterion, whereas a negative EDIFFG implies that the Hellmann-Feynman forces acting on each atom individually must reach a value below this criterion.
- PREC Specifies the precision mode of the calculations.

- ENCUT Sets the cutoff energy.
- NELM Sets the maximum number of electronic steps if the EDIFF value is not reached.
- NELMIN Sets the minimum value of electronic self-consistency steps.
- ISIF Determines whether the stress tensor i calculated, along with the degrees of freedom which are allowed to change.
- IBRION Determines by which algorithm the atoms are updated and moved.
- NSW Determines the number maximum number of ionic steps.
- NPAR Determines the parallelization of the calculations.

A.1.1 Specifying functionals

Specifying functionals are done by setting some extra tags in the INCAR. The settings for PBEsol and optPBE are given in Listing A.2

Listing A.2: *INCAR functional settings*

```
#PBEsol
GGA = PS


#optPBE
GGA = OR
LUSE_VDW = .TRUE.
AGGAC = 0.0000
```

POSCAR

The POSCAR file (Listing A.3) contains all information about the geometry of the supercell. In this file, the vectors spanning the supercell are specified along with the coordinates of all atoms within the cell. The first line is a comment line for naming the system. The second line contains a scaling value for the vectors spanning the cell volume and all atomic coordinates. The following three lines are cartesian vector coordinates spanning the volume of the supercell. The sixth and seventh line provide the atomic species and number of atoms within the cell per atomic species. It is crucial that the order of the atomic species in the POSCAR file is in accordance with the order of the potentials of the respective elements within the POTCAR file. On the eight line, the mode *Direct* specifies that the following atomic coordinates are given in direct, or fractional coordinates rather than in cartesian. The remaining lines provide the fractional coordinates of the atomic positions within the supercell.

Listing A.3: *POSCAR file*

```
GaAs
    1.00000000000000
    5.66184470611923    0.00000000000000    0.00000000000000
    0.00000000000000    5.66184470611923    0.00000000000000
    0.00000000000000    0.00000000000000    5.66184470611923
  Ga     As
  4      4
Direct
  0.000000000000000   0.00000000000000    0.00000000000000
  0.000000000000000   0.50000000000000    0.50000000000000
  0.500000000000000   0.00000000000000    0.50000000000000
  0.500000000000000   0.50000000000000    0.00000000000000
  0.249999985000002   0.24999998500000    0.24999998500000
  0.750000000000000   0.75000000000000    0.24999998500000
  0.750000000000000   0.24999998500000    0.75000000000000
  0.249999985000002   0.75000000000000    0.75000000000000
```

POTCAR

The POTCAR file contains the physical information about the atoms specified in the POSCAR file, thus all the pseudo-potentials for the different elements are included in this file. The atomic order in the POTCAR file needs to be the same as specified in the POSCAR file.

KPOINTS

The KPOINTS file contains the k-points in reciprocal space. Listing A.4 shows an example of a typical KPOINTS file. The first line in the KPOINTS file (Listing A.4) specifies the generation of an automatic k-mesh in which one only has to specify how the Brilloiun zone (BZ) is subdivided in each direction along the reciprocal lattice vectors. The second line activates the generation of the automatic mesh. The third line generates a Γ-centered k-mesh, whereas the fourth line specifies the subdivision of the BZ. The last line is an optional shift of the mesh. For all calculations in the present work, a Γ-centered, automatically generated mesh has been generated. The shift of the last line has also been set to zero throughout all calculations.

Listing A.4: *KPOINTS file*

```
Automatic mesh
0
Gamma
12   12   8
0   0   0
```

A.2 Accurate DOS calculations

Accurate DOS calculations are performed in two steps. The first is a self-consistent run, during which a CHGCAR is written, which is a file containing the system charge density. This file is simply written by setting the tag CHGCAR = .TRUE. in the INCAR file. The precision mode must be set to "High" during this run.

A second non-self-consistent run is performed for which the charge density is fixed throughout the calculation to the density found in the first, self-consistent run. In this step the k-points are treated independently and the k-point density should be increased. In Listing A.5 are given the specific tags that need to be set for this run.

Listing A.5: *Spesific tags in non-self-consistent calculations for accurate DOS*

```
ICHARG = 11

PREC = High

# DOS
LORBIT = 11
EMIN = -10
EMAX = 10
NEDOS = 401
```

- ICHARG = 11 reads the charge density from the file CHGCAR.
- Prec = High Is set to achieve high precision of calculations.
- LORBIT = 11 provides orbital resolved wave functions.
- EMIN, EMAX determines the energy range in eV with a minimum and maximum value, respectively, between which DOS should be calculated.
- NEDOS sets the resolution for the DOS.

Chapter B

VASP files

B.1 Bulk GaAs

B.1.1 GaAs relaxation and *ab*-strain

The INCAR file applied for bulk relaxation and *ab*-strain calculations is shown in Listing B.1.

Listing B.1: *INCAR bulk relaxation and ab-strain*

```
# general                              ENCUT = 400
SYSTEM = GaAs bulk
ISTART = 0                             NELM = 60
ICHARG = 2                             NELMIN = 2
INIWAV = 1
ISMEAR = 0                             ISIF = 3
SIGMA = 0.01                           IBRION = 2
EDIFF = 1.0e-09                        NSW = 50
EDIFFG = -0.001                        NPAR = 4
PREC = N
LREAL = AUTO                           #PBEsol
                                       GGA = PS
```

B.1.2 Bulk GaAs DOS

Listing B.2 shows the INCAR file for the selfconsistent run in bulk GaAs DOS calculations. Listing B.3 shows the INCAR file for the non-selfconsistent run in bulk GaAs DOS calculations.

Listing B.2: *INCAR DOS selfconsistent run*

```
SYSTEM = GaAs                          ENCUT = 400
ISTART = 0
ICHARG = 2                             NELM = 60
```

```
INIWAV = 1                          NELMIN = 2
SIGMA = 0.01
EDIFF = 1.0e-09                     ISIF = 3
EDIFFG = -0.001                     IBRION = 2
PREC = High                         NSW = 0
LREAL = .FALSE.
LCHARG = .TRUE.                     GGA = PS
LWAVE = .FALSE.
```

Listing B.3: *INCAR DOS non-selfconsistent run*

```
SYSTEM = GaAs                       NELM = 60
ISTART = 0                          NELMIN = 2
ICHARG = 11                         ISIF = 3
INIWAV = 1                          IBRION = 2
ISMEAR = -5                         NSW = 0
SIGMA = 0.01
EDIFF = 1.0e-08                     #PBEsol
EDIFFG = -0.001                     GGA = PS
PREC = High
LREAL = .FALSE.                     # DOS
LCHARG = .FALSE.                    LORBIT = 11
LWAVE = .FALSE.                     EMIN = -10
                                    EMAX = 10
ENCUT = 400                         NEDOS = 401
```

B.2 Graphite $P6_3mc$

B.2.1 Volume relaxation

In Listing B.4, the INCAR file for full relaxation of graphite $P6_3mc$ is shown.

Listing B.4: *INCAR volume relaxation*

```
# general                           ENCUT = 910
SYSTEM = graphite
ISTART = 0                          NELM = 60
ICHARG = 2                          NELMIN = 2
INIWAV = 1
ISMEAR = 0                          ISIF = 3
SIGMA = 0.01                        IBRION = 2
EDIFF = 1.0e-09                     NSW = 50
EDIFFG = -0.001                     NPAR = 4
PREC = N
LREAL = .FALSE.                     #optPBE
LCHARG = .FALSE.                    GGA = OR
LWAVE = .FALSE.                     LUSE_VDW = .TRUE.
```

```
                                      AGGAC = 0.0000
```

B.2.2 DOS calculations

Listing B.5 shows the INCAR file for the selfconsistent run in bulk graphite DOS calculations. Listing B.6 shows the INCAR file for the non-selfconsistent run in bulk graphite DOS calculations.

Listing B.5: *INCAR DOS selfconsistent run*

```
# general                             ENCUT = 910
SYSTEM = graphite
ISTART = 0                            NELM = 60
ICHARG = 2                            NELMIN = 2
INIWAV = 1
ISMEAR = 0                             ISIF = 3
SIGMA = 0.01                          IBRION = 2
EDIFF = 1.0e-09                       NSW = 0
EDIFFG = -0.001
PREC = High                           #optPBE
LREAL = .FALSE.                       GGA = OR
LCHARG = .TRUE.                       LUSE_VDW = .TRUE.
LWAVE = .FALSE.                       AGGAC = 0.0000
```

Listing B.6: *INCAR DOS non-selfconsistent run*

```
# general                              ISIF = 3
SYSTEM = graphite                     IBRION = 2
ISTART = 0                            NSW = 0
ICHARG = 11
INIWAV = 1                            #optPBE
ISMEAR = 0                            GGA = OR
SIGMA = 0.01                          LUSE_VDW = .TRUE.
EDIFF = 1.0e-08                       AGGAC = 0.0000
EDIFFG = -0.001
PREC = High
LREAL = .FALSE.                       # DOS
LCHARG = .FALSE.                      LORBIT = 11
LWAVE = .FALSE.                       EMIN = -10
                                      EMAX = 10
ENCUT = 910                           NEDOS = 401

NELM = 60
NELMIN = 2
```

B.3 GaAs surface reconstruction

B.3.1 Slab relaxation and *ab-plane strain*

In Listing B.7 the INCAR file for relaxation of GaAs slab supercells is included. The same INCAR file is used for GaAs slab *ab*-strain calculations.

Listing B.7: *INCAR slab relaxation*

```
SYSTEM = GaAs                      ENCUT = 400
ISTART = 0
ICHARG = 2                         NELM = 60
INIWAV = 1                         NELMIN = 2
ISMEAR = 0
SIGMA = 0.01                       ISIF = 2
EDIFF = 1.0e-09                    IBRION = 2
EDIFFG = 0.01                      NSW = 50
PREC = High                        NPAR = 4
LREAL = .FALSE.
LCHARG = .FALSE.
LWAVE = .FALSE.                    GGA = PS
LVTOT = .TRUE.
```

B.3.2 Chemical potential of Ga metal

Listing B.8 shows the INCAR for calculation of the chemical potential of Ga(s). Different values for the ISMEAR and SIGMA tag were tested.

Listing B.8: *INCAR* $\mu(Ga(s))$

```
SYSTEM = Ga metal                  NELM = 60
ISTART = 0                         NELMIN = 2
ICHARG = 2                         ISIF = 3
INIWAV = 1                         IBRION = 2
ISMEAR = ismear                    NSW = 50
SIGMA = sigma                      NPAR = 4
EDIFF = 1.0e-09
EDIFFG = -0.001
PREC = High                        GGA = PS
LREAL = .FALSE.

ENCUT = 400
```

B.4 Heterostructure calculations

B.4.1 Coarse energy mapping

Listing B.9 provides the INCAR file for static calculations with heterostructure supercells. For calculations performed with PBEsol, the PBEsol functional is specified rather than the optPBE functional.

Listing B.9: *INCAR coarse energy mapping*

```
# general                               NELM = 60
SYSTEM = heterostructure                NELMIN = 2
ISTART = 0
ICHARG = 2                               ISIF = 3
INIWAV = 1                              IBRION = 2
ISMEAR = 0                              NSW = 0
SIGMA = 0.1                             NPAR = 4
EDIFF = 1.0e-06
EDIFFG = 0.01                           #optPBE
PREC = Accurate                         GGA = OR
AMIN = 0.01                             LUSE_VDW = .TRUE.
LREAL = Auto                            AGGAC = 0.0000

ENCUT = 550
```

B.4.2 Fine energy mapping

Listing B.10 shows the INCAR file for dynamic calculations with heterostructure supercells.

Listing B.10: *INCAR fine energy mapping*

```
# general                               NELM = 60
SYSTEM = heterostructure                NELMIN = 2
ISTART = 0
ICHARG = 2                               ISIF = 2
INIWAV = 1                              IBRION = 2
ISMEAR = 0                              NSW = 50
SIGMA = 0.1                             NPAR = 4
EDIFF = 1.0e-06
EDIFFG = 0.01                           #optPBE
PREC = Accurate                         GGA = OR
AMIN = 0.01                             LUSE_VDW = .TRUE.
LREAL = Auto                            AGGAC = 0.0000

ENCUT = 550
```

B.4.3 DOS calculations

In Listing B.11 the INCAR file for the selfconsistent of heterostructure DOS calculations is shown, and in Listing B.12, the INCAR file for the non-selfconsistent run is included.

Listing B.11: *INCAR DOS selfconsistent run*

```
# general
SYSTEM = heterostructure
ISTART = 0
ICHARG = 2
INIWAV = 1
ISMEAR = 0
SIGMA = 0.1
EDIFF = 1.0e-06
EDIFFG = 0.01
PREC = High
AMIN = 0.01
LREAL = Auto
LCHARG = .TRUE.
LWAVE = .FALSE.
LELF = .TRUE.

ENCUT = 550
NELM = 60
NELMIN = 2

ISIF = 2
IBRION = 2
NSW = 0


#optPBE
GGA = OR
LUSE_VDW = .TRUE.
AGGAC = 0.0000
```

Listing B.12: *INCAR DOS non-selfconsistent run*

```
# general
SYSTEM = heterostructure
ISTART = 0
ICHARG = 11
INIWAV = 1
ISMEAR = 0
SIGMA = 0.01
EDIFF = 1.0e-06
EDIFFG = 0.01
PREC = High
AMIN = 0.01
LREAL = Auto


ENCUT = 550

NELM = 60
NELMIN = 2
ISIF = 2
IBRION = 2
NSW = 0
NPAR = 4

#optPBE
GGA = OR
LUSE_VDW = .TRUE.
AGGAC = 0.0000

# DOS
LORBIT = 11
EMIN = -10
EMAX = 10
NEDOS = 401
```